



seit 1558

Vibrational Spectroscopy on Stem Cells in Wound Healing

Dissertation zur Erlangung des akademischen Grades des Doktors der

Naturwissenschaften (Dr. rer. nat.)

eingereicht in der Fakultät für Physicalische Chemie der Friedrich-Schiller-Universität

Jena

vorgelegt von

Katherine Lau, MSc Biomedical and Forensics Studies in Egyptology

(29th May, 1982, Hong Kong)

Gutachter:

Professor Jürgen Popp

PD Dr Volker Deckert

PD Dr Michael Gottschadt

Datum der Verteidigung::

21 December 2011

Declaration of Honour / Selbständigkeitserklärung

Ich erkläre, dass ich die vorliegende Arbeit selbständig und unter Verwendung der angegebenen Hilfsmittel, persönlichen Mitteilungen und Quellen angefertigt habe.

Ort, Datum

Unterschrift der Verfasserin

Katherine Lau MSc. BSc. (Hons)

Education

- July 07-
Oct 10 **Institute of Photonic Technology – Jena, Germany**
Institute of Analytical Sciences – Dortmund, Germany
PhD Student in Bio-Spectroscopy
Thesis title: Vibrational Spectroscopy on Stem Cells in Wound Healing
- Sept 04 –
Sept 05 **The University of Manchester, England, UK**
MSc Biomedical and Forensic Studies in Egyptology (Distinction, awarded Dec 05)
Thesis: Analysis of Fatty Acid Profiles of Mummified Humans and Animals by GC-MS
Involved phthalate identification
- Sept 01 –
Sept 04 **The University of Edinburgh, Scotland, UK**
BSc (Honours) Biological Sciences - Developmental Biology (Class 2)
Thesis: Cell-cell interaction during amoeba-to-flagellate transformation (Awarded 2.1)
- Sept 99 –
June 01 **Malvern Girls' College, Worcestershire, UK**
A-levels: Biology (A); Chemistry (B); Mathematics (A)

Scientific Employment History

- Nov 10 –
Present **Application Scientist – Raman spectroscopy in Life Sciences**, Renishaw plc., Glos., UK
- Develop application areas for Raman spectroscopy in biological sciences.
 - Develop new life sciences market specific products
- Nov 06-
June 07 **Scientific Researcher**, Family Genetics, Stockport, UK; Centre for Integrated Genomic Research (CIGMR), The University of Manchester, UK
- Developed Y-chromosome microsatellites panels.
 - Designed primers and multiplexes, PCR and capillary electrophoresis conditions.
- Jan 06 –
May 06 **Laboratory Manager**, Family Genetics, Stockport, UK
- Performed genomic tests
 - Wrote genetic ancestry report
 - Developed haplotyping software for automation
 - Stock control
- Aug 03 **Research assistant**, Dr. Evelyn Telfer, The University of Edinburgh, UK
- Assisted in research on the early bovine follicular development.
- July 00
- Aug 00 **Laboratory assistant**, Cord Blood Bank, Hong Kong Red Cross, Hong Kong
- Processed data of umbilical cord stem cells donors and filed documents.

Scientific Achievements and Participation

- Awarded grant** Boehringer Ingelheim Fonds Travel Grant (July 09)
Funded my research work at the Australian Synchrotron Centre, Victoria, Australia.
- Affiliation** Member of Society of Applied Spectroscopy (2011-present)
Member of Infrared Raman Discussion Group(2009-present)
Member of GdCH (2009-2011)
- Publications** 1. K. Lau, M.A.B. Hedegaard, J.E. Kloepper, R. Paus, B.R.Wood, and V. Deckert (2011).

Visualization and characterisation of defined hair follicle compartments by Fourier transform infrared (FTIR) imaging without labelling (*J. Dermatol. Sci.* 63(3): 191-198)

2. Lau, K., Paus, R., Tiede, S. *et al* (2009) **Exploring the role of stem cells in cutaneous wound healing** (invited review, cover of issue, *Exp Dermatol* 18(11):921-933)
3. Lau, K., Wood, B.R., Kloepper, J.E. *et al* (2010) **Locating mesenchymal stem cells in the human hair follicle dermal papilla by focal plane array-Fourier transform infrared spectroscopy** (*Exp Dermatol*, 19(2):221)
4. Lau, K., Kloepper, J.E., Paus, R., *et al* (2010) **Distinguishing and characterizing hair follicle tissue layers using Fourier transform infrared spectroscopy** (*Exp Dermatol*, 19(2):223)
5. K. Lau, W. Schumacher, J.E. Kloepper, C. Krafft, J. Popp, R. Paus and V. Deckert (2011). **A classifier built on single hair follicle FTIR spectra for demarcating hair follicular compartments based on spectral variations.** (*Analyst*; submitted)
6. K. Lau, A.J. Hobro, T. Smith, T. Thurston, B. Lendl (2011). **Label-free non-destructive in situ biochemical analysis of nematode *Steinernema kraussei* using FPA-FTIR and Raman spectroscopic imaging.** (*Vib. Spectrosc.*; submitted)
7. L. Ashton, K. Lau, C.L. Winder, R. Goodacre (2011). **Raman Spectroscopy: Lighting up the future of microbial identification.** (*Fut. Microbiol.*; invited review, submitted)

Oral Presentations SPEC 2010, Manchester, UK (June/July 10)
'Towards the Identification of Hair Follicle Mesenchymal Stem Cells with FPA-FTIR'

Photonics4Life, Barcelona, Spain (Nov 09)
'Hair Follicle FTIR Imaging and Finding Mesenchymal Stem Cells'

- Conference Posters**
1. **Presence of lipid polarisation in human hair follicle epithelial progenitor cells revealed by Raman mapping.** (Jun 2011) ICAVS-6, Sonoma County, CA, USA.
 2. **Raman imaging of a *Steinernema kraussei*.** (Jun 2011) ICAVS6, Sonoma County, CA, USA
 3. **Towards label-free non-destructive identification of stem cells in the hair follicle with confocal Raman spectroscopy.** (Aug 2010) ICORS, Boston, USA.
 4. **Classifier built from hair follicle single FTIR spectra – a reproducible modality for demarcating cell types within an organ.** (Jun 2010) SPEC 2010, Manchester, UK.
 5. **Towards the Identification of Hair Follicle Mesenchymal Stem Cells by FPA-FTIR.** (Oct 2009) FTIR-Diagnostics Workshop, RKI-Berlin, Germany.
 6. **Seeking mesenchymal stem cells in the human hair follicle with FTIR microspectroscopy.** (Jul 2009) ICAVS-5, Melbourne, Australia.
 7. **Differentiation of tissue layers within the hair follicle using FT-IR spectroscopy.** (Mar 2009) ANAKON, Berlin, Germany.
 8. **FT-IR microspectroscopy towards the identification of mesenchymal stem cells in the hair follicle - Application on wound healing.** (Nov 2008) SPEC 2008, Sao Paolo, Brazil.(poster)

Relevant Training Intensive Entrepreneurship In Photonics Training, Vrije Universiteit Brussel, Belgium (Jan 10)
Home Office Animal Handling License Training, University of Manchester (May 07)

Table of Contents

Dedication.....	x
List of Abbreviations.....	xi
Glossary.....	xiv
Zusammenfassung.....	xv
Chapter 1 Introduction.....	1
1.1 Hair follicle stem cells and their involvement in cutaneous wound healing.....	2
1.1.1 Introduction to stem cells.....	2
1.1.2 The importance of cutaneous wound healing.....	3
1.2 The role of hair follicle stem cells in wound healing <i>in vivo</i>	4
1.2.1 Hair follicle epithelial stem cells.....	5
1.2.2 Hair follicle mesenchymal stem cells.....	6
1.2.3 Success of applying tissue-specific stem cells to wound treatments and the need for isolating hair follicle stem cells using vibrational spectroscopy.....	8
1.3 Scope of research.....	11
Chapter 2 Methods and Instrumentation.....	15
2.1 Introduction – Applying vibrational spectroscopy to biological samples.....	16
2.1.1 Why is vibrational spectroscopy suitable for hair follicle stem cell identification?.....	16
2.2 Infrared spectroscopy – background and theory.....	17
2.2.1 IR spectroscopy.....	17
2.2.2 Selection rules.....	18
2.2.3 Vibrational modes.....	18
2.2.4 Energy prediction for molecular vibrations.....	19
2.2.5 IR transmission vs absorption.....	20
2.2.6 Fourier transform infrared spectroscopy (FTIR).....	21
2.2.7 FTIR mapping and imaging and spatial resolution.....	23
2.3 Raman spectroscopy – background and theory.....	25
2.3.1 Raman microspectroscopy and mapping.....	25
2.3.2 Raman theory.....	25
2.3.3 Raman intensity.....	28
2.3.4 Conventions.....	28
2.3.5 Coupling Raman spectroscopy to microscopy and Raman spectroscopic imaging.....	28
2.4 Examples of application of vibrational spectroscopy to skin and hair.....	30
2.5 Examples of application of vibrational spectroscopy to stem cells.....	31
Chapter 3 Proof of Principle: Application of FTIR mapping and N-FINDR algorithm to demarcating tissue compartments within the human hair follicle bulb.....	35
3.1 Abstract.....	36
3.2 Introduction.....	36

3.3	Materials and methods.....	38
3.3.1	Sample origin.....	38
3.3.2	Skin section preparation.....	38
3.3.3	Sample selection.....	38
3.3.4	FTIR measurement.....	39
3.3.5	Data analysis.....	39
3.4	Results.....	41
3.4.1	Data set 1.....	41
3.4.1.1	Overall morphology and protein distribution according to IR spectra.....	41
3.4.1.2	Specific FTIR spectra correspond to distinct hair follicle compartments as shown in data set 1.....	43
3.4.1.3	N-FINDR abundance maps in relation to hair follicle anatomy.....	46
3.4.2	Data set 2.....	47
3.4.3	Data set 3.....	50
3.5	Discussion.....	51
3.5.1	Biological relevance of the N-FINDR results.....	52
3.5.2	Suitability of using N-FINDR on hair follicle spectra.....	54
3.5.3	Perspectives for use of FTIR microspectroscopy in the hair biology field.....	55
3.6	Conclusions.....	55
Chapter 4 Classifier built from hair follicle single FTIR spectra – a reproducible method for demarcating cell types in an organ.....		59
4.1	Abstract.....	60
4.2	Introduction.....	60
4.3	Materials and methods.....	61
4.3.1	Sample source.....	61
4.3.2	Preparation and measurement.....	61
4.3.3	Chemometrics.....	62
4.4	Results and Discussion.....	62
4.5	Conclusion.....	67
Chapter 5 Elucidation of lipid spectral features in the hair follicle mesenchyme in relation to mesenchymal stem cells.....		69
5.1	Abstract.....	70
5.2	Introduction.....	70
5.3	Materials and methods.....	71
5.3.1	Human skin sections.....	71
5.3.2	FTIR mapping.....	72
5.3.3	Data processing.....	72
5.4	Results and discussion.....	72
5.5	Outlook.....	76
Chapter 6 Identifying human hair follicle bulge epithelial progenitor cells using FTIR spectroscopy.....		78
6.1	Abstract.....	79
6.2	Introduction.....	79
6.3	Materials and methods.....	80
6.3.1	Human skin sample origin.....	80

6.3.2	K15 positive epiPCs and ORS cells on CaF ₂ and quartz substrates.....	81
6.3.3	Skin section preparation.....	81
6.3.4	FTIR imaging.....	81
6.3.5	Statistical evaluation.....	81
6.3.5.1	Resonant Mie scattering correction (RMieS).....	81
6.3.5.2	PCA.....	82
6.3.5.3	Unsupervised hierarchical clustering analysis (UHCA).....	82
6.4	Results and discussion.....	82
6.4.1	Viability of hair follicle K15+ epiPCs and ORS cells on the CaF ₂ substrates affirmed.....	82
6.4.2	Multivariate analysis applied to single FTIR spectra revealed homogeneity within the K15+ epiPCs population.....	83
6.4.3	Increase in total lipids and decrease in total proteins, established as a FTIR signature of K15+ epiPCs.....	86
6.4.4	FTIR spectroscopy revealed different trends in nucleic acids levels between hair follicle epiPCs and ORS cells.....	89
6.4.5	Spectral features suggest higher acyl branching in the more differentiated ORS cells.....	90
6.4.6	Correlation of high lipid contents to lipid storage in stem cells.....	90
6.4.7	Changes in protein expression from progenitor cells to TA cells and their activated status.....	90
6.4.8	FTIR imaging of the hair follicle bulge revealed the location of epiPCs with spectral features of primary K15+ epiPCs.....	91
6.4.9	Establishment of K15+ epiPCs spectral features and demonstration of their label-free identification within the hair follicle bulge paves way for future label-free epiPCs sorting.....	92
6.5	Conclusion.....	93
Chapter 7 Locating mesenchymal stem cells in the human hair follicle using FTIR spectroscopy.....		96
7.1	Abstract.....	97
7.2	Introduction.....	97
7.3	Materials and methods.....	98
7.3.1	Human skin sample origin.....	98
7.3.2	Skin sections preparation.....	98
7.3.3	Immunohistochemistry – nestin staining (for correlation to FTIR imaging).....	98
7.3.4	Immunohistochemistry – nestin staining (followed by Raman spectra collection).....	99
7.3.5	FTIR spectroscopy.....	99
7.3.6	Raman spectral collection.....	99
7.3.6.1	Raman map on CTS.....	99
7.3.6.2	Single point Raman spectra collection on stained skin section.....	100
7.3.7	Statistical evaluation.....	100
7.3.7.1	UHCA.....	100
7.3.7.2	Raman map processing.....	100
7.4	Results.....	100
7.4.1	Visualisation of single cells within their natural habitat using FTIR and UHCA.....	100
7.4.2	Verification with a second data set and scalp skin hair follicle immunohistochemistry.....	102
7.4.3	Confocal Raman mapping of the MSC-rich human hair follicle CTS successfully differentiated cell spectra.....	106

7.5	Discussion.....	109
7.5.1	K15+ epiPCs spectral features as a guideline for locating MSCs with FTIR.....	109
7.5.2	The feasibility of FTIR spectroscopy in identifying hair follicle MSCs.....	110
7.5.3	Potentials for MSC identification within the hair follicle demonstrated by Raman mapping of CTS, which distinguished CTS cells from their ECM.....	111
7.5.4	Perspectives in the direction of cell sorting using vibrational spectroscopy.....	112
7.6	Conclusion.....	112
Chapter 8 Perspective work.....		115
8.1	Abstract.....	116
8.2	Introduction.....	116
8.3	Materials and methods.....	118
8.3.1	Hair follicle K15+ epiPCs and ORS cells isolation.....	118
8.3.2	Raman maps collection.....	118
8.3.3	Raman map processing.....	118
8.4	Results.....	118
8.5	Discussion.....	119
8.6	Conclusion.....	120
Chapter 9 Summary, conclusion and outlook.....		122
9.1	Importance of developing a reliable stem cell identification modality.....	123
9.2	Need for label free identification of hair follicle stem cells.....	123
9.3	Feasibility of using FTIR spectroscopy to discern hair follicle tissue compartments proven.....	124
9.4	A classifier trained specifically to identify hair follicle tissue types.....	125
9.5	Elucidation of lipid features detectable by FTIR spectroscopy in DP cells.....	126
9.6	Establishment of FTIR spectral markers for human hair follicle K15+ epiPCs.....	126
9.7	Identifying MSCs in the human hair follicle using FTIR spectroscopy.....	127
9.8	Paving way for human hair follicle MSC identification with Raman spectroscopy..	127
9.9	Raman mapping revealed lipid polarisation in single K15+ epiPCs but not in ORS cells.....	129
9.10	Conclusion and outlook.....	129
Acknowledgments.....		132

Dedication:

I would like to dedicate this thesis to my beloved late father, Luke Lau, who has been and continues to be a source of inspiration and motivation.

Abbreviations

ADM – acellular dermal matrix

ADSC – adipose-derived stem cell

APM – arrector pili muscle

ASC – adult stem cell

ATR – attenuated total reflection

B – bulge

BM – bone marrow

BPF – band pass filter

BS – beam splitter

CCD – charge coupled device

CTS – connective tissue sheath

db – diabetic

DNA – deoxyribose nucleic acid

DP – dermal papilla

ECM – extracellular matrix

EF – edge filter

epiPC – epithelial progenitor cell

epiSC – epithelial stem cell

DAPI - diamidino-2-phenylindole

DNA – deoxyribose nucleic acid

ESC – embryonic stem cell

FA – fatty acid

FACS – fluorescence-activated cell sorting

FPA – focal plane array

FTIR – Fourier transform infrared

GFP – green fluorescent protein

GT – granulation tissue

hESC – human embryonic stem cell

HSC – haematopoietic stem cell

HPC – haematopoietic progenitor cell

IR - infrared

IRS – inner root sheath

IV - intravenous

K15 – cytokeratin 15

K15+ - cytokeratin 15 positive

mESC – murine embryonic stem cell

mRNA – messenger ribose nucleic acid

M – hair follicle matrix cells

MACS – magnetic activated cell sorting

mESC- murine embryonic stem cell

MSC – mesenchymal stem cell

Nestin+ – nestin positive

NOD – non-obese diabetic

NSC – neuronal stem cell

OF – optical fibre

ORS – outer root sheath

PBS – phosphate buffered saline

PFA - paraformaldehyde

PC – principal component

PCA – principal component analysis

qRT-PCR – quantitative reverse transcriptase polymerase chain reaction

TA – transient amplifying

RMieS – resonant Mie scattering correction

RNA – ribose nucleic acid

RSC – retinal stem cells

satFA – saturated fatty acid

SC - subcutis

SNR – signal to noise ratio

SR – synchrotron

SVM – support vector machine

UHCA – unsupervised hierarchical clustering analysis

unsatFA – unsaturated fatty acid

VCA – vertex component analysis

WL – white light

Glossary

Adult stem cell – stem cell, which can be found in the adult stage of an organism

Autologous stem cell – stem cell from one's own body

Bipotent – can differentiate into two cell types

Embryonic lineage – endoderm, mesoderm and ectoderm

Embryonic stem cell – stem cell, which is found in the inner cell mass of an embryo in the blastocyst stage

Label-retaining cell – when incubated with a DNA label, such as bromodeoxyuridine, a cell that retains the label after a prolonged period of time, due to its slow cycling (few cell divisions) property, is called a label-retaining cell. DNA label is not retained in fast cycling cells, due to novel DNA strand synthesis during cell division.

Multipotent – can differentiate into multiple, but not all, cell types of the embryonic lineages

Progenitor cell – a relatively undifferentiated cell type that can differentiate into more mature cell types. It can divide many times but not indefinitely, and is usually committed to a certain embryonic lineage. The definition of a progenitor cell and its difference from a stem cell is still being evolved.

Pluripotent – can differentiate into cell types of any embryonic lineages in the organism

Quiescent – describes a relatively dormant cell that goes through its cell cycle slowly (i.e. slow cycling). A quiescent cell stays in the G₀ phase of the cell cycle, hence not rapidly dividing.

Stem cell – a stem cell can multiply (self-renew) indefinitely, divide asymmetrically to preserve a stem cell pool, and to produce a daughter cell that is more differentiated.

Stem cell niche – an anatomical location where stem cells are known to predominately reside, where stem cells are maintained in their stem cell state, supported by the diffusible factors secreted by the cells that make up the niche.

Teratocarcinoma – a tumour consisting of cells of different lineages that continually multiply

Transient amplifying cell – a daughter cell of a stem/progenitor cell, which is more differentiated than a stem/progenitor cell, has a more migratory phenotype and higher proliferation rate, but not end-differentiated. It can be regarded as an intermediate cell type between stem cell and end-differentiated cell.

Unipotent – can differentiate into one cell type

Xeno-transplantation – transplantation from one animal species to another

Zusammenfassung

Menschliche Haarfollikel bieten eine reichhaltige Quelle an Stammzellen, die naturgemäß an der kutanen Wundheilung beteiligt sind. Die in der Haut gelegenen Haarfollikel sind zudem leicht zugänglich. Daher besteht großes Interesse an der Verwendung von Haarfollikel-Stammzellen zur Wundbehandlung. Mesenchymale Stammzellen und Epithelvorläuferzellen im menschlichen Haarfollikel sind an der dermalen und epidermalen Wundheilung beteiligt und sind der Schwerpunkt der in dieser Dissertation beschriebenen Arbeit.

Schwingungsspektroskopie ist eine labelfreie und nicht-invasive Methode. Der spektrale Fingerabdruck einer Zell-Linie bietet die Möglichkeit einer labelfreien Klassifizierung lebender Zellen. Ziel dieser Arbeit ist deshalb die Anwendung von Schwingungsspektroskopie zur Identifizierung und Analyse von Haarfollikel-Stammzellen.

Der erste Teil dieser Arbeit (Kapitel 3 und 4) beschreibt zwei proof-of-principle Studien, die die Realisierbarkeit der Anwendung von FTIR Spektroskopie und chemometrischer Analyse (N-FINDR und SVM) zur Differenzierung verschiedener Gewebearten im Haarfollikel allein auf spektralen Unterschieden basierend zeigen. Mittels N-FINDR wurden erfolgreich unvermischte Spektren (Endmember) aus FTIR Maps von Haarfollikeln extrahiert, die sowohl chemisch als auch strukturell mit individuellen Gewebebereichen korrelierten. Die SVM wurde auf einzelne FTIR Spektren bekannter Gewebebereiche trainiert und ermöglichte eine Zuordnung unbekannter Spektren einer Haarfollikel FTIR Map zu ihren jeweiligen Gewebeschichten. Die SVM bietet eine reproduzierbare Methode Gewebeschichten in Haarfollikeln zu unterscheiden.

Nachfolgend richtete sich die Arbeit auf die Anwendung von FTIR Spektroskopie zur Identifizierung einzelner Zellen im Haarfollikel. Kapitel 5 beschreibt die spektrale Analyse einzelner Zellen in Bezug auf Stammzeleigenschaften durch die Anwendung von FTIR Mapping auf die dermale Papille mit anschließendem Clustering der Spektren mittels UHCA. Die Unterschiede der Banden der C-H-Streckschwingungen, die Fettsäuren und Proteinen zugeordnet werden, waren hierbei von besonderem Interesse.

Kapitel 6 beschreibt die FTIR Charakteristika von Epithelvorläuferzellen der Haarfollikel. Primäre menschliche Haarfollikel- Epithelvorläuferzellen und differenzierte Zellen der äußeren Wurzelscheide wurden extrahiert und einer FTIR-spektroskopischen Analyse unterzogen. Haarfollikel- Epithelvorläuferzellen wiesen die höchste Lipidkonzentration auf, welche in vorübergehend amplifizierten Zellen und Zellen der äußeren Wurzelscheide

abnahm. Im Gegensatz dazu besaßen die Epithelvorläuferzellen die geringste Proteinkonzentration. Die erhöhte Gesamtlipidkonzentration und erniedrigte Proteinkonzentration wurden als wichtige Kriterien zur Identifizierung von menschlichen Haarfollikel- Epithelvorläuferzellen erachtet.

Obwohl mesenchymale Stammzellen menschlicher Haarfollikel Nestin exprimieren, fehlen mesenchymalen Stammzellen eindeutige Marker und eine definierte Nische, was die Isolierung purer mesenchymaler Stammzellen für die Etablierung einer FTIR-Signatur erschwert. Kapitel 7 beschreibt, wie FTIR Charakteristika von Epithelvorläuferzellen als Leitlinie zur Identifizierung mesenchymaler Stammzellen im Haarfollikel genutzt werden können. FPA-FTIR wurde als bildgebendes Verfahren auf Haarzwiebeln angewendet, um mesenchymale Stammzellen zu lokalisieren. Der FPA Detektor hatte eine physische Pixelgröße von $5.5 \times 5.5 \mu\text{m}^2$ und verfügte über die räumliche Auflösung einzelner Zellen. Die Anwendung von UHCA auf die FTIR Maps isolierte erfolgreich Spektren im Haarfollikel-Mesenchym, welche die Spektren mit erhöhter Gesamtlipidkonzentration und erniedrigte Proteinkonzentration darstellten. Außerdem wurden diese putativen mesenchymalen Stammzell-Spektren sowohl in der dermalen Papille als auch im Bindegewebe gefunden. Darüber hinaus wies die Lage der putativen mesenchymalen Stammzellen im Falschfarbenbild ein ähnliches Muster auf wie die Nestin Immunreaktivität in der Immunfärbung. Damit war erwiesen, daß mit FTIR Spektroskopie als bildgebendem Verfahren mesenchymale Stammzellen im menschlichen Haarfollikel lokalisiert werden konnten.

Eine weitere Verifizierung erfordert zukünftige Studien, um mesenchymale Stammzellen lebender Haarfollikel mittels Schwingungsspektroskopie zu identifizieren und um zu zeigen, ob diese Zellen auch *in vitro* Stammzeleigenschaften aufweisen. Da die Ramanspektroskopie geeigneter für die Analyse lebender Zellen ist als FTIR Spektroskopie ist es wahrscheinlich, daß die Verifizierung mittels Ramanspektroskopie durchgeführt wird.

Im letzten Teil dieser Arbeit (Kapitel 7 und 8) werden Daten von Raman Mappings dargestellt um die Realisierbarkeit zu zeigen, Raman Spektren sowohl von Zellen von Haarfollikeln in Hautschnitten als auch von unabhängigen einzelnen Zellen zu erhalten. Während die Ramanspektroskopie eine laterale Auflösung im sub-Mikrometerbereich bietet,

kann mittels FTIR Bildgebung ein schneller Überblick über einen großen Gewebebereich erlangt und die Stammzellen genau lokalisiert werden.

Die Arbeit in dieser Dissertation zeigt neuartige Beispiele auf, Schwingungsspektroskopie zur Charakterisierung von Stammzellen in Haarfollikeln anzuwenden. Die vorliegende Arbeit ebnet den Weg für eine labelfreie und nicht-invasive Technik zur Klassifizierung von Stammzellen in Haarfollikeln und besitzt das Potential, auf lebende Haarfollikelzellen angewendet zu werden.

Chapter 1

Introduction

1.1 Hair follicle stem cells and their involvement in cutaneous wound healing

1.1.1 Introduction to stem cells

Stem cells are cells that have a self-renewal capacity and ability to produce daughter cells which are more differentiated. In embryos, stem cells are involved the embryonic development and organogenesis, whereas in adults, stem cells are important for replenishing lost cells both because of normal homeostasis and injury.

The difference between embryonic stem cells (ESCs) and adult stem cells (ASCs; also known as tissue-specific stem cells) lies in their differentiation potentials. ESCs, which can be isolated from the inner cell mass during the blastula stage (32-cell stage; Fig.1) of the embryonic development, are pluripotent, meaning they can differentiate into cell types of any embryonic lineages (endoderm, mesoderm and ectoderm) in the organism¹. The pluripotency of ESC can be maintained *in vitro* indefinitely. Spontaneous differentiation results from the removal of leukocyte inhibiting factor from the cell culture medium², whereas targeted differentiation can be mediated by administering the appropriate diffusible factors^{3,4}.

ASCs can be found at their respective niches⁵, such as the bone marrow endosteal region for haematopoietic stem cells (HSCs)⁶ and the hair follicle bulge for hair follicle epithelial stem cells (epiSCs)⁷. ASCs may be multipotent, bipotent or unipotent, meaning they can differentiate into multiple cell types, two cell types or one mature cell type. Their differentiation potentials are usually limited to one embryonic lineage, though cases of stem cells capable of differentiating from one lineage to another (termed transdifferentiation) have been described⁸⁻¹⁰.

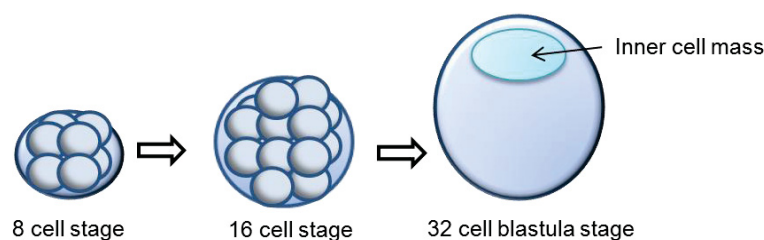


Figure 1 illustrates the development of an embryo from the 8 cell stage to the 32 cell blastula stage. The inner cell mass present in the blastula stage contain embryonic stem cells, which will proceed to forming the embryo, whereas the rest of the blastula goes on to form the placenta.

The current definition of tissue-specific stem cells¹¹ states that the population constitutes undifferentiated cells capable of:

- 1) Homing upon engraftment to adequate growth microenvironment(s)
- 2) Extensive proliferation
- 3) Producing large numbers of differential progeny
- 4) Self-renewal
- 5) Functional tissue repair after injury
- 6) With flexibility/reversibility in the use of the previous options.

Furthermore, stem cells last through the longevity of the host^{12, 13}. They are known to be quiescent (slow-cycling) *in vivo* so as to conserve the stem cell pool. In fact, HSCs are even known to enter hibernation¹⁴, to prevent the exhaustion of the HSC population by entering cell cycles frequently.

ASCs have been identified in almost every tissue type in the human body. Their exploitation for regenerative medicine purposes invokes considerably fewer ethical concerns than the use of ESCs¹⁵. Therapies involving autologous ASCs do not post risks of immuno-rejection. Moreover, ASCs are not known to be at risk of forming teratocarcinoma as ESCs may. Consequently there has been a rapid growth in the field of basic ASC research, and its clinical applications to regenerative medicine. Stem cells in bone marrow¹⁶, adipose tissues, dental pulp¹⁷ and skin¹⁸ are potential sources for harvesting stem cells for stem cell treatments. Skin is not only highly accessible, but also contains numerous types of ASCs¹⁹. A list of ASCs known to participate in cutaneous wound healing is summarised in Supp. Fig. 1.

1.1.2 The importance of cutaneous wound healing

Skin is the largest compartment of the body. As skin has multiple important functions such as acting as the barrier to foreign pathogens, regulating body temperature, supplying sensation, and preventing dehydration of the body²⁰⁻²⁵, normal wound healing is a critical survival factor, both in the individual and the species as a whole. In current medical practice, aberrations of cutaneous wound healing consumes substantial resources and often requires major, long-term medical attention²⁶. Severe scarring disorders not only affect the patients aesthetically but also psychosocially²⁷⁻²⁹. Burn injury presents another type of insult to the skin which not only can be potentially lethal, but whose depleting effects on local tissue stem cells may result in the inability of the wound to repair itself, thus increasing the need to surgically graft borrowed skin from another body site to restore the functions of the skin^{30, 31}.

Chronic wounds severely affect a patient's quality of life³² and generate enormous medical costs^{26,33,34}. Such wounds are frequently linked to old age³², coinciding with a poorer reservoir of fully functional stem cells^{12, 13, 35, 36}. Both chronic wound and keloid scarring may recur, suggesting differences in the intrinsic healing ability of stem cells between patients who heal poorly and those who heal more aggressively. Both hypertrophic and keloid scarring are characterized by hyperproliferation of wound fibroblasts^{37, 38} and overproduction of extra cellular matrix (ECM) proteins³⁹⁻⁴¹. In addition, keloid scarring is characterized by its invasive growth into the surrounding skin and high risk of recurrence following any treatment modality^{29, 42-44}.

ASCs are considered to be the source for replenishing lost cells during wound healing, and therefore are recognized as key players in tissue regeneration. A more complete understanding of the ASCs that contribute to normal and impaired wound healing and their regulatory controls, therefore, appears vital for a better control of wound repair, and is likely to promote novel treatment strategies for improved wound healing.

1.2 The role of hair follicle stem cells in wound healing *in vivo*

There are three main phases in the cutaneous wound healing cascade: the inflammatory, proliferative and tissue remodelling leading to scar formation⁴⁶. The hair follicle is a dynamic regenerative organ⁴⁵ in the skin compartment and is a rich source of ASCs that participate in cutaneous wound healing¹⁹. While the hair follicle contains stem cells that contribute to all three phases of wound healing¹⁹, we shall focus on the hair follicle epithelial stem cells (epiSCs) and the hair follicle mesenchymal stem cells (MSCs). Figure 2 illustrates the anatomical structure of the human hair follicle and depicts where epiSCs and MSCs are located.

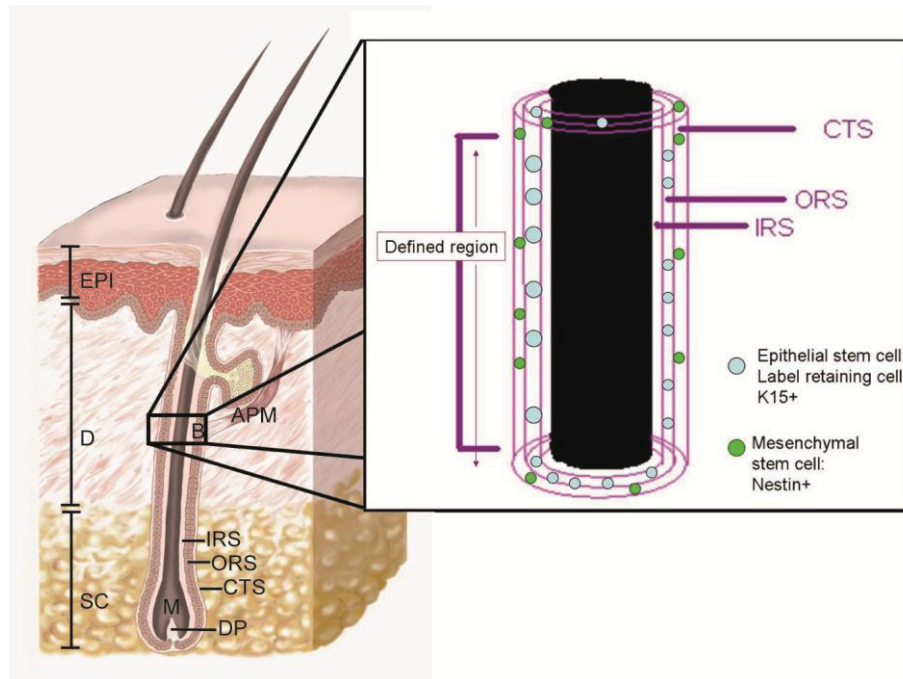


Figure 2. This figure illustrates the anatomical structure of an anagen VI human hair follicle in the human skin. Human skin comprises of epithelium (EPI), dermis (D) and subcutis (SC). An anagen VI hair follicle extends into the SC. The dermal papilla (DP) in the hair bulb is part of the mesenchyme. The DP is surrounded by hair follicle matrix cells (M) of the epithelium. The bulge (B) region of a human hair follicle is identified as the part of the outer root sheath (ORS) where the arrector pili muscle (APM) inserts into. Cytokeratin (K15)⁺ cells, i.e. epithelial stem cells, are predominantly found in the bulge⁵⁸. In the enlargement figure, the three layers inner root sheath (IRS), ORS and connective tissue sheath (CTS) are depicted. epiSCs can be found in the bulge in the ORS. MSCs, which are nestin⁺, are found in the CTS. (Adapted from figure in *Exp Dermatol* 18(11):921-933)⁵⁹

1.2.1 Hair follicle epithelial stem cells

Hair follicle epiSCs were first identified as label-retaining cells (demonstration of quiescent nature)⁴⁷⁻⁴⁹ and are predominantly found in the so called bulge of the hair follicle^{47, 48, 50, 51}. The bulge is located in the outer root sheath (ORS) of the permanent portion of the hair follicle where the arrector pili muscle (APM) inserts (Fig.2). They have been demonstrated to contribute to all hair follicle lineages⁵¹⁻⁵⁴. epiSCs are self-renewing and able to produce rapidly proliferating daughter transient amplifying (TA) cells that undergo several cell divisions before differentiating and leaving the basal compartment⁵⁵⁻⁵⁷.

Lyle *et al*⁴⁷ established that cytokeratin 15 (K15), an intracellular intermediate filament protein, is expressed in human hair bulge cells. Since then, more human bulge epiSC markers have been identified⁶⁰⁻⁶². The most useful positive *in situ* markers for human bulge cells are

considered K15, cytokeratin19 and CD200⁶⁰⁻⁶², though these markers are not exclusively expressed in the bulge. Thanks to the previous thorough characterisation of epiSCs, the isolation of human bulge epiSCs was made possible. The isolation of epiSCs was realised through transfecting the ORS of human hair follicles from scalp skin with non-viral vectors, which induces K15 promoter-driven expression of green fluorescent protein (GFP) and geneticin resistance. Plastic adherence is also selected for⁸.

In response to injury, epiSCs provide keratinocytes that are necessary for reconstructing the epidermal barrier^{53, 63}. While hair follicle bulge epiSCs are not necessarily required for epidermal survival⁶³, nor does its absence prevent reepithelialisation⁶⁴, they enhance the early stages of wound closure⁶⁴⁻⁶⁶. In neonatal mouse models, ablating early hair follicle epiSCs severely impaired epidermal regeneration⁶⁵. In adult mutant mice that lacked hair follicle development, an acute delay in wound closure occurred⁶⁴. In an adult patient micro-grafting hair follicles in a dermal regeneration template applied to a full thickness burn wound successfully accelerated reepithelialisation through the mediation by hair follicle epiSCs².

1.2.2 Hair follicle mesenchymal stem cells

Hair follicle MSCs have been identified from the connective tissue sheath (CTS; Fig.2, Fig.3a) and the dermal papilla (DP; Fig. 2, Fig.3a) of the hair follicle⁶⁷⁻⁶⁹. Their potentials to differentiate into adipocytes, osteocytes, chondrocytes, haematopoietic, neuronal and smooth muscle cells^{18, 67, 70-73} have been demonstrated. Not only are these MSCs multipotent, they are also known to participate in dermal wound healing⁵⁹. A link between the recovery of the number of DP and dermal reconstruction has been suggested, such that a smaller number of DP recovered correlates to increased scarring⁷⁴. Transplantation of hair follicles with vital dye-labelled CTS cells into a murine wound bed resulted in the incorporation of CTS fibroblasts from the lower hair follicle being incorporated into the wounded dermis⁶⁸. In intact mouse skin, hair follicle cycling involves extensive, bidirectional trafficking of fibroblasts between the DP and the CTS⁷⁵, hence it is conceivable that CTS fibroblasts may migrate into the interfollicular dermis under wound healing conditions^{68, 69, 76}.

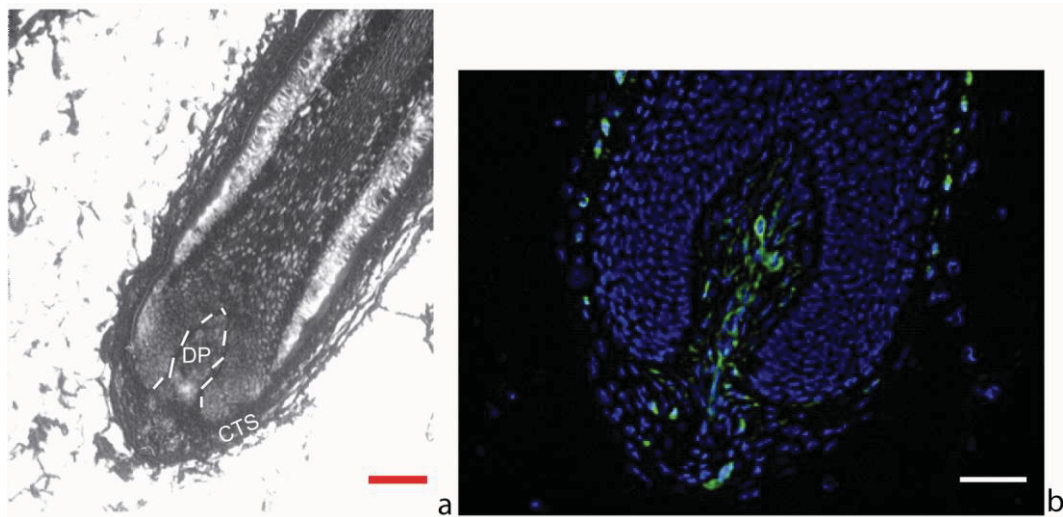


Figure 3. a) A scanning electron microscopy image of a longitudinal section of an anagen VI human hair follicle in a skin section. The dotted line demarcates the basement membrane zone between the DP and the hair follicle matrix cells. The CTS is the layer that separates the hair follicle from its surrounding adipose tissue. Scale bar: 100 μm . **b)** An immunofluorescence image of a hair bulb. Nestin immunoreactivity can be visualised in green and the nuclei of the cells in blue. Nestin expression is found in the DP and the CTS of the human hair follicle. Scale bar: 50 μm .

Unlike human hair follicle epiSCs^{7, 48, 49, 53, 77, 47, 50}, MSC populations lack definitive markers. MSCs can often be recognised by a cocktail of surface markers such as CD44, CD90, CD73 and CD49^{71, 72}. The hair follicle MSCs are also known to express nestin^{61, 73, 78}, an intermediate filament and ASC marker also expressed by neuronal stem cells (NSCs)⁷⁹. However, nestin is not a definitive marker for hair follicle MSCs. Unlike the hair follicle epiSCs which are pre-dominantly found in the bulge, the hair follicle MSCs do not have a characterised specific niche within the mesenchyme. The lack of definitive markers and defined niche presents great challenges for obtaining a pure MSC colony from the human hair follicles for further characterisation. Therefore, Fourier transform infrared (FTIR) spectroscopy is proposed as a modality to identify these MSCs within the hair follicle, based on the intrinsic molecular differences between stem cells and differentiated cells as reflected in the FTIR spectra.

1.2.3 Success of applying tissue-specific stem cells to wound treatments and the need for isolating hair follicle stem cells using vibrational spectroscopy

Numerous strategies have been applied to treat skin wounds using ASCs, where positive effects on all phases of wound healing have been reported with various types of MSCs and hair follicle epiSC⁸⁰⁻⁸⁹. Summarised in Table 1 are examples of stem cell based wound treatments applied to animal models, and in Table 2 examples of treatments applied to human patients. It should be emphasised that, while success with applying ASCs to wound treatments is aplenty, the choice of stem cell type and mode of application has to be based upon the age and the genetics of the patient. Since this area is out of the scope of this thesis, readers are referred to review Ref¹⁹ for further information.

Hair follicle stem cells are not only natural strong mediators for cutaneous wound healing *in vivo*, they are also situated in a highly accessible part of the body facilitating their harvesting. Thus, epiSCs and MSCs are ideal candidates for stem cell based wound treatments. Current cell isolation methods involve the use of labels, such as fluorescence activated cell sorting (FACS), and transfection with plasmids^{8,88}, rendering the labelled stem cells unsuitable for direct application to patients. Therefore, vibrational spectroscopy is proposed to be a label-free non-invasive modality for identifying stem cells from the hair follicle. Freed of exogenous tags that may interact with cellular processes, stem cells can be reliably characterised and can also be safely applied to patients.

Table :1 Summary of stem cell treatments that have been applied to animal models to improve wound healing and their results. IV: intravenous; MSC: mesenchymal stem cell; hMSC: human MSC; NOD: non-obese diabetic; db: diabetic; wt: wild type; ADSC: adipocyte derived stem cells; ADM: acellular dermal matrix; GT: granulation tissue

Treatment	Species/ model	Control	Results	Ref
Spraying autologous/ allogeneic MSC with a mixture of fibrin and thrombin	<i>db/db</i> mice and <i>wt</i> mice with full thickness wound	<i>db/+</i> littermates and <i>db/db</i> mice with fibrin spray alone	Prevention of ulceration and accelerated wound closure	⁸⁰
Intradermal injection of BM-MSC round the wound or in Matrigel applied to wound bed	Semi-transparent BALB/c and <i>db/db</i> mice with full- thickness excisional skin wounds	neonatal dermal fibroblasts or vehicle treatment	Increased complete wound closures in <i>db/db</i> mice; Enhanced reepithelialisation, cellularity; increased vasculature and appendages; thicker and larger GT	⁸²
BM-MSC systematically or locally applied	Streptozotocin-induced diabetic adult rats	Untreated adult rats	Immediate and insignificant increase in wound collagen and wound healing growth factors	⁸⁴
Collagen gel solution with ADSC applied	Female nude mice, with 2 full-thickness dorsal wounds each	Collagen gel solution with no ADSC	Significant reduction of wound size and accelerated the reepithelialisation from the wound edge	⁸⁵
Human ADSC seeded in human ADM xeno-tranplanted to murine skin wounds	Athymic nude mice with dorsal full-thickness excisional wound	No graft applied or unseeded ADM applied to wounds	Acceleration of wound closure; local persistence of applied ADSC, differentiation into epidermal, endothelial cells and dermal fibroblasts	⁸⁶

Table 2 Summary of clinical trials on wound patients, using stem cells, to improve wound healing and their results. MSC: mesenchymal stem cell; hMSC: human MSC; ADSC: adipocyte derived stem cells; ADM: acellular dermal matrix

Treatment	Patients	Control	Results	Ref
Spraying autologous MSC with a mixture of fibrin and thrombin	Patients with acute and chronic wounds	Fibrin spray alone without MSC applied to second or third wound in patients with >1 wounds	strong correlation between the no. of cells and reduction of ulcer area; instant pain relief to acute wound patients; acceleration of wound closure and resurfacing; ulcer size reduction or complete wound closure in chronic wound patients by 16-20 weeks; no adverse effects	⁸⁰
Topical application of culture expanded autologous BM-MSC	Human chronic ulcer (> 1 year) patients not responded to other previous treatments	Other conventional treatments as listed in publication	Wound closure, increase in cellularity and dermal rebuilding	⁸⁷
Hair follicle micrografts into Integra dermal regeneration template applied to burn wound 12 days after burn	Human male patient suffering from a 12% full thickness burn	No control, although compared with previous treatments without follicle micrografts.	Accelerated reepithelialisation induced by hair follicle stem cells; restoration of stem cell populations, achieved hair growth and skin maturation.	⁸⁹

1.3 Scope of Research

The advantages of applying hair follicle stem cells to wound healing treatments, as well as other stem cell based treatments, can be realised through isolation of the stem cell population from their differentiated counterparts and via thorough characterisation. Understanding the interaction of stem cells with their environment would allow better design of treatments. In the previous section a list of examples was provided to show the promises of stem cell based wound healing treatments. Despite the promises, careful assessment of stem cells behaviour should be carried out, to ensure the safety of the designed treatments. By enabling the isolation, expansion and characterisation of the hair follicle epithelial progenitor cells (epiPCs) and MSCs, the stem cell population expansion condition can be optimised. Careful evaluation of their behaviour before, during and after stem cell transplantation can be assessed and monitored. Label-free non-destructive identification and the said stem cell types will potentially accelerate the isolation process, increase the number of stem cells usable for treatments, and allow continual monitoring of their morphological changes during their expansion in vitro. The scope of this re-search includes establishing FTIR spectroscopy as a viable technique to differentiate tissue and cell types within the hair follicle; identifying spectral features of the hair follicle stem cells and therefore enabling their identification using FTIR spectroscopy. Last but not least, this thesis presents data from Raman mapping, with implications on future directions of work in this area of research.

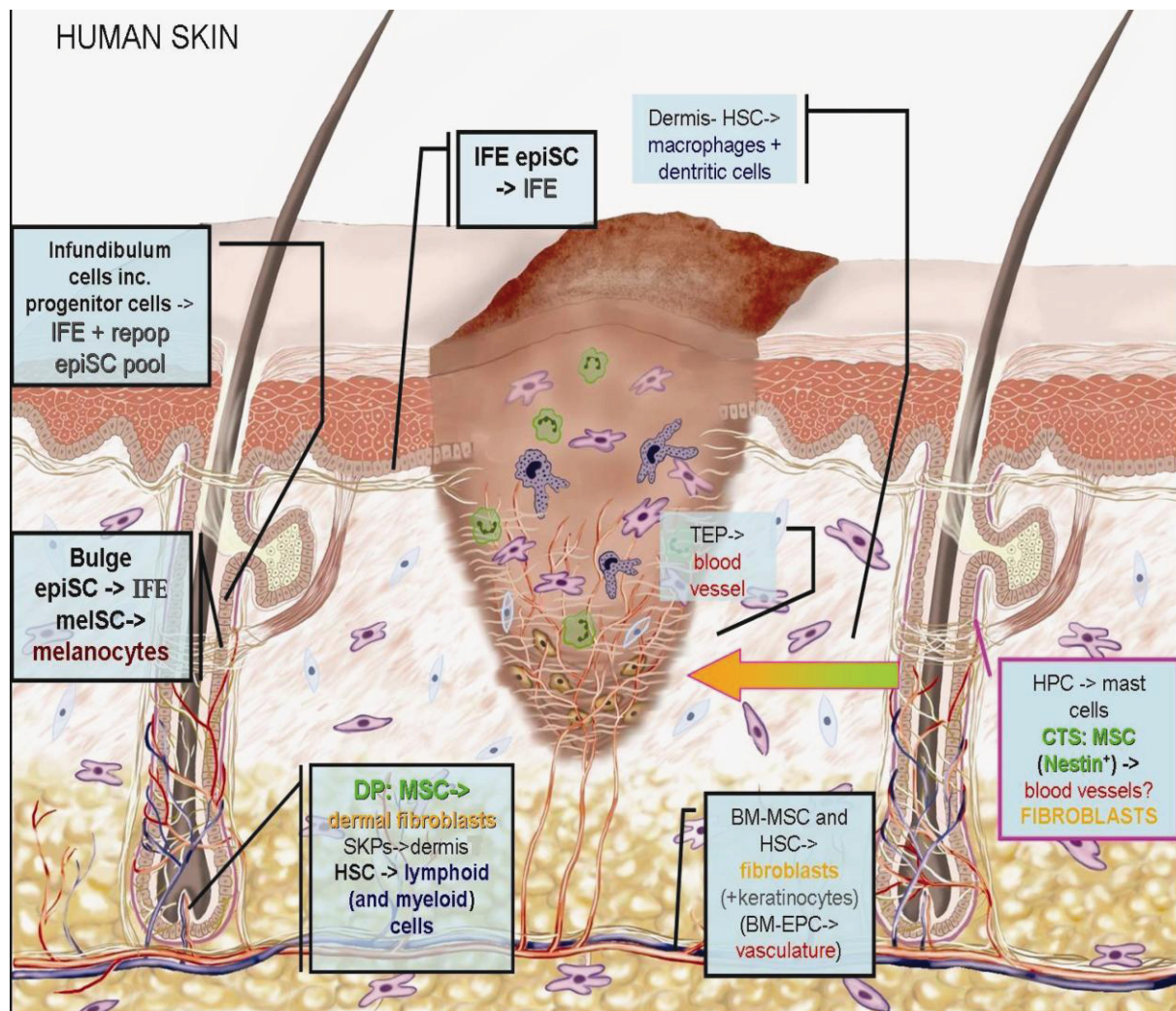
References:

1. A. G. Smith, *Annu Rev Cell Dev Biol* 2001, **17**, 435-462.
2. A. G. Smith, *Methods Cell Sci*, 1991, **13**, 89-94.
3. M. Puc at, *Methods*, 2008, **45**, 168-171.
4. L. Iacovitti, A. E. Donaldson, C. E. Marshall, S. Suon and M. Yang, *Brain Res*, 2007, **1127**, 19-25.
5. A. Spradling, D. Drummond-Barbosa and T. Kai, *Nature*, 2001, **414**, 98-104.
6. H.-G. Kopp, S. T. Avecilla, A. T. Hooper and S. Rafii, *Physiology*, 2005, **20**, 349-356.
7. M. Ito, K. Kizawa, M. Toyoda and M. Morohashi, *J Invest Dermatol*, 2002, **119**, 1310-1316.
8. S. A. Mani, W. Guo, M.-J. Liao, E. N. Eaton, A. Ayyanan, A. Y. Zhou, M. Brooks, F. Reinhard, C. C. Zhang, M. Shipitsin, L. L. Campbell, K. Polyak, C. Brisken and J. a. W. Yang, R.A., *Cell*, 2008, **133**, 704-715.
9. L. Crigler, A. Kazhanie, T. J. Yoon, J. Zakhari, J. Anders, B. Taylor and V. M. Virador, *FASEB J*, 2007, **21**, 2050-2063.
10. Z. Hu and J. Corwin, *PNAS*, 2007, **104**, 16675-16680.
11. M. Loeffler and I. Roeder, *Cells Tissues Organs*, 2002, **171**, 8-26.
12. C. Zouboulis, Adjaye, J, Akamatsu, H, Moe-Behrens, G, Niemann, C., *Exp Gerontol.*, 2008, **43**, 986-997.
13. A. Nijnik, L. Woodbine, C. Marchetti, S. Dawson, T. Lambe, C. Liu, N. Rodrigues, T. Crockford, E. Cabuy, A. Vindigni, T. Enver, J. Bell, P. Slijepcevic, C. Goodnow, P. Jeggo and R. Cornwall, *Nature*, 2007, **447**, 686-690.
14. S. Yamazaki, A. Iwama, S.-i. Takayanagi, Y. Morita, K. Eto, H. Ema and H. Nakauchi, *EMBO J*, 2006, **25**, 3515-3523.
15. Opinion No. 15 of the European Group on Ethics regarding the "Ethical aspects of human

stem cell research and use". Annex E. http://europa.eu.int/comm/european_group_ethics/index_en.htm.

16. Y. Jiang, B. Jahagirdar and R. Reinhardt, *Nature*, 2002, **418**, 41-49.
17. A. Sloan and A. Smith, *Oral Dis*, 2007, **13**, 151-157.
18. C. A. B. Jahoda, C. J. Whitehouse, A. J. Reynolds and N. Hole, in *Exp Dermatol*, 2003, **12**, 849-859.
19. K. Lau, R. Paus, S. Tiede, P. Day and A. Bayat, *Exp Dermatol*, 2009, **18**, 921-933.
20. E. Proksch, J. M. Brandner and J.-M. Jensen, *Exp Dermatol*, 2008, **17**, 1063-1072.
21. A. H. Haake and K. Holbrook, in *Fitzpatrick's Dermatology in General Medicine*. K. Wolff, L.A. Goldsmith, S.I. Katz, B.A. Gilchrest, A. Paller and D.J. Leffell, McGraw Hill, New York, Edition 5, 2007.
22. A. Singer and R. Clark, *N Engl J Med*, 1999, **341**, 738-746.
23. P. Martin, *Science*, 1997, **276**, 75-81.
24. R.A.F. Clark, in *The molecular and cellular biology of wound repair*, ed. R.A.F. Clark, Plenum Press, New York, Edition 2, 1996, pp. 257-288.
25. M. Yu, A. Finner, J. Shapiro, B. Lo, A. Berekatain and K. J. McElwee, *Experts Rev. Dermatol.*, 2006, **1**, 855-871.
26. A. Boulton, L. Vileikyte, G. Ragnarson-Tennvall and J. Apelqvist, *Lancet* 2005, **366**, 1719-1724.
27. B. C. Brown, S. P. McKennac, K. Siddhic, D. A. McGrouther and A. Bayat, *J Plast Reconstr Aesthet Surg*, 2008, **61**, 1049-1058
28. A. Bayat, G. Arscott, W. E. R. Ollier, M. W. J. Ferguson and D. A. McGrouther, *J R Soc Med* 2003, **96**, 554-555.
29. A. Bayat, D. A. McGrouther and M. W. J. Ferguson, *BMJ*, 2003, **326**, 88-92.
30. A. Piatkowski, A. Gröger, M. Pantel, A. Bozkurt, P. C. Fuchs and N. Pallua, *Burns*, 2008, **35**, 256-263.
31. J. Garrison, F. Thomas and P. Cunningham, *Transplant Proc*, 1995, **27**, 1416-1418.
32. P. J. Franks, C. J. Moffatt, D. C. Doherty, R. Smithdale and R. Martin, *Wound Rep Reg*, 2006, **14**, 536-541.
33. D. T. Ubbink, Westerbos, S.J., Nelson, E.A., Vermeulen, H., *Br J Surg.*, 2008, **95**, 685-692.
34. C. Harrington, M. J. Zagari, J. Corea and J. Klitenic, *Diabetes Care*, 2000, **23**, 1333-1338.
35. S. M. Chambers, C. A. Shaw, C. Gatza, C. J. Fisk and L. A. Donehower, et al., *PLoS Biol.*, 2007, **5**, e201.
36. G. Van Zant and Y. Liang, *Exp Hematol*, 2003, **31**, 695-672.
37. R. J. Wassermann, M. Polo, P. Smith, X. Wang, F. Ko, M.C. Robson, *J Surg Res* 1998, **75**, 74-80.
38. P. Teofoli, S. Barduagni, M. Ribuffo, A. Campanella, O. De Pita, P. Puddu, *J Dermatol Sci*, 1999, **22**, 31-37.
39. M. Babu, R. Diehlmann and N. Oliver, *Mol Cell Biol*, 1989, **9**, 1642-1650.
40. A. Dalkowski, D. Schuppan, C.E. Orfanos, C.C. Zouboulis, *Br J Dermatol*, 1999, **141**, 50-56.
41. A. Bayat and D.A. McGrouther, *Br J Hosp Med.*, 2006, **67**, 527-532.
42. P. Durani and A. Bayat, *J Plast Reconstr Aesthet Surg.*, 2008, **61**, 4-17.
43. D. T. Robles and D. Berg, *Clin Dermatol*, 2007, **25**, 26-32.
44. T. A. Mustoe, R. D. Cooter, M. H. Gold, F. D. R. Hobbs, A.-A. Ramelet, P. G. Shakespeare, M. Stella, L. Téot, F. M. Wood and U. E. Ziegler, *Plast Reconstr Surg*, 2002, **110**, 560-571.
45. M. R. Schneider, R. Schmidt-Ullrich and R. Paus, *Curr Biol*, 2009, **19**, R132-R142.
46. S. Werner and R. Gross, *Physiol Rev*, 2003, **83**, 835-870.
47. S. Lyle, M. Christofidou-Solomidou, Y. Liu, D. E. Elder, S. Albelda and Cotsarelis G., *J Cell Sci* 1998, **111**, 3179-3188.
48. G. Cotsarelis, T.T. Sun, and R.M. Lavker, *Cell*, 1990, **61**, 1329-1337.
49. R. Morris and C. Potten, *J Invest Dermatol*, 1999, **112**, 470-475.
50. R. Morris, Y. Liu, L. Marles, Z. Yang, C. Trempus, S. Li, J. Lin, J. Sawicki and G. Cotsarelis, *Nature Biotechnol*, 2004, **22**, 411-417.
51. H. Oshima, A. Rochat, C. Kedzia, K. Kobayashi and Y. Barrandon, *Cell*, 2001, **104**, 233-245.
52. T. Tumber, G. Guash, V. Greco, C. Blanpain, W.E. Lowry, M. Rendl, E. Fuchs, *Science*, 2004, **303**, 359-363.
53. G. Taylor, M. S. Lehrer, P. J. Jenson, T. T. Sun and R. M. Lavker, *Cell*, 2000, **102**, 451-461.
54. R.J. Morris, Y. Liu, L. Marles, Z. Yang, C. Trempus, S. Li, J.S. Lin, J.A. Sawicki and G. Cotsarelis, *Nature Biotechnol*, 2004, **22**, 411-417.
55. C. Potten and R. Morris, *J Cell Sci Suppl.*, 1988, **10**, 45-62.
56. L. Liang and J. Bickenbach, *Stem Cells*, 2002, **20**, 21-31.
57. A. Hosoya, J.-M. Lee, S.-W. Cho, J.-Y. Kim, N. Shinozaki, T. Shibahara, M. Shimono and H.-S. Jung, *Histochem Cell Biol*, 2008, **130**, 1165-1175.
58. M. Ohyama, *J Dermatol Sci*, 2007, **46**, 81-89.

59. K. Lau, R. Paus, S. Tiede, P. Day and A. Bayat, *Exp Dermatol*, 2009, **18**, 921-933.
60. M. Ohyama, A. Terunuma, C. L. Tock, M. F. Radonovich, C. A. Pise-Masison, S. B. Hopping, J. N. Brady, M. C. Udey and J. C. Vogel, *J Clin Invest*, 2006, **116**, 249-260.
61. J. E. Kloepper, S. Tiede, J. Brinckmann, D. P. Reinhardt, R. Faessler and R. Paus, *Exp Dermatol.*, 2008, **17**, 592-609.
62. V. Jaks, N. Barker, M. Kasper, J. van Es, H. Snippert, H. Clevers and R. Toftgard, *Nature Genet*, 2008.
63. M. Ito, Y. Liu, Z. Yang, J. Nguyen, F. Liang, Morris RJ. and G. Cotsarelis, *Nature Med*, 2005, **11**, 1351-1354.
64. A. K. Langton, S. E. Herrick and D. J. Headon, *J Invest Dermatol*, 2007, **128**, 1311-1318.
65. J. A. Nowak, L. Polak, H. A. Pasolli and E. Fuchs, *Cell Stem Cell*, 2008, **3**, 33-43.
66. D. M. Ansell, J. E. Kloepper, H. A. Thomason, R. Paus and M. J. Hardman, *J Invest Dermatol*, 2010, **131**, 518-528.
67. M. Lako, L. Armstrong, P. Cairns, S. Harris, N. Hole and C. Jahoda, *J Cell Sci*, 2002, **115**, 3967-3974.
68. C. A. B. Jahoda and A. J. Reynolds, *Lancet*, 2001, **358**, 1445-1448.
69. A. Gharzi, A. J. Reynolds and C. A. B. Jahoda, *Exp Dermatol*, 2003, **12**, 126-136.
70. E. V. Kiseleva, E. S. Chermnykh, E. A. Vorotelyak, A. I. Volozhin, A. V. Vasiliev and V. V. Terskikh, *Cell Tissue Biol*, 2009, **3**, 42-49.
71. M. J. Hoogduijn, E. Gorjup and P. G. Genever, *Stem Cells Dev*, 2006, **15**, 49-60.
72. J. Y. Liu, H. F. Peng, S. Gopinath, J. Tian and S. T. Andreadis, *Tissue Engineering Part A*, 2010, **16**, 2553-2564.
73. C. Kruse, E. Bodo, A. E. Petschnik, S. Danner, S. Tiede and R. Paus, *Exp Dermatol*, 2006, **15**, 794-800.
74. K. Sugata, T. Kitahara and Y. Takema, *Skin Res Technol*, 2008, **14**, 436-439.
75. D. Tobin, A. Gunin, M. Magerl, B. Handijski and R. Paus, *J Invest Dermatol Symp Proc* 2003, **8**, 80-86.
76. G. D. Richardson, E. C. Arnott, C. J. Whitehouse, C. M. Lawrence, A. J. Reynolds, N. Hole and C.A.B. Jahoda, *J Invest Dermatol Symp Proc*, 2005, **10**, 180-183.
77. C. Blanpain, Lowry, W.E., Geoghegan, A., Polak, L., Fuchs, E., *Cell*, 2004, **118**, 635-648.
78. S. Tiede, J. E. Kloepper, N. Ernst, B. Poeggeler, C. Kruse and R. Paus, *J Invest Dermatol*, 2009, **129**, 2711-2720.
79. H. Ito, A. Nakajima, H. Nomoto and S. Furukawa, *J Neurosci Res*, 2002, **71**, 648-658.
80. V. Falanga, S. Iwamoto, M. Chartier, T. Yufit, J. Butmarc, N. Kouttab, D. Shrayner and P. Carson, *Tissue Eng*, 2006, **13**, 1299-1312.
81. S. François, M. Mouisseddine, N. Mathieu, A. Semont, P. Monti, N. Dudoignon, A. Saché, A. Boutarfa, D. Thierry, P. Gourmelon and A. Chapel, *Ann Hematol*, 2007, **86**, 1-8.
82. Y. Wu, L. Chen, P. G. Scott and E. E. Tredget, *Stem Cells*, 2007, **25**, 2648-2659.
83. H. Kwon, P. H. Liu, D.-H. Lew, E. Nishimura and D. P. Orgill, *Eplasty*, 2008, **8**, 1-11.
84. D. Kwon, X. Gao, Y. Liu, D. DS, A. Danyluk, M. Bansal, M. Chopp, K. McIntosh, A. Arbab, S. Dulchavsky and S. Gautam, *IWJ*, 2008, **5**, 453-463.
85. W.-S. Kim, B.-S. Park, J.-H. Sung, J.-M. Yang, S.-B. Park, S.-J. Kwak and J.-S. Park, *J Dermatol Sci*, 2007, **48**, 15-24.
86. A.M. Altman, N. Matthias, Y. Yan, Y.-H. Song, X. Bai, E.S. Chiu, D.P. Slakey and E.U. Alt, *Biomaterials*, 2008, **29**, 1431-1442.
87. E. V. Badiavas and V. Falanga, *Arch Dermatol*, 2003, **139**, 510-516.
88. C. Roh, Q. Tao, C. Photopoulos, and S. Lyle, *J Invest Dermatol*, 2005, **125**, 1099-1105.
89. H. A. Navsaria, N. O. Ojeh, N. Moiemmen, M. A. Griffiths and J. D. Frame, *Plast Reconstr Surg*, 2002, **113**, 978-981.



Supplementary Figure 1: This figure summarises the stem/progenitor cell populations that contribute to cutaneous wound healing. Bars connecting to text boxes show where these populations normally reside in the skin and coloured texts describe the end differentiation products. Texts ‘keratinocytes’ and ‘BM-EPC-> vasculature’ are put in brackets to indicate their occurrences in normal wound healing, albeit recorded, are rare. Where there is a question mark, it means that the notion is possible but has not been shown by empirical evidence. Abbreviations: IFE- interfollicular epidermis; epiSC- epithelial stem cell; meISC- melanocyte stem cell; MSC-mesenchymal stem cell; SKPs- skin progenitor cells; HSC- haematopoietic stem cell; EC-endothelial cell; TEP- tissue endothelial progenitors; BM- bone marrow; EPC- endothelial precursor cells; HPC- haematopoietic progenitor cells (Published in *Exp Dermatol* 18(11):921-933).

Chapter 2

Methods and Instrumentation

2.1 Introduction – Applying vibrational spectroscopy to biological samples

Vibrational spectroscopic methods – Fourier transform infrared (FTIR) spectroscopy and Raman spectroscopy - are the main techniques applied in the studies presented in this thesis. This chapter will describe the theories behind FTIR and Raman spectroscopies, and discuss why they are suitable methods for achieving the aim of identifying stem cells in the hair follicle.

The application of vibrational spectroscopy to biological samples is typically termed biospectroscopy. Both FTIR and Raman spectroscopies provide information on the chemical contents in the samples, as the wavelengths (either absorbed or scattered), are specific for the functional groups in the molecules. The interaction of vibrational groups in molecules with electromagnetic radiation is measured. Infrared (IR) spectroscopy measures the absorption of IR radiation, while Raman spectroscopy measures the inelastic scattering of photons.

2.1.1 Why is vibrational spectroscopy suitable for hair follicle stem cell identification?

In the last chapter, the needs for isolating stem cells from the hair follicle were discussed. While specific markers are known for the bulge epithelial progenitor cells (epiPCs), definitive markers for hair follicle mesenchymal stem cells (MSCs) are yet established. To enable the isolation of both hair follicle stem cell types, and to apply them to stem cell based treatments, markers are required for their recognition. Since the chemical contents of biological samples can be reflected in their IR or Raman spectra, it is possible to find unique features in the spectra that can be exploited as markers or signatures for specific cell types.

One of the biggest advantages of vibrational spectroscopic techniques is their label free nature. Since vibrational spectroscopy measures the interaction of the molecules with light directly, labelling is not required. In addition, the techniques are generally non-destructive. Currently, the examination of chemical contents in biological samples largely relies on the use of molecular tags. For examples, the use of antibodies for detecting proteins expression¹, *in situ* hybridisation probes for detecting gene expression² and lipid-fluorescent probes for identifying lipid structures³. Although such labelling methods can provide very specific information, the number of molecules that can be detected at any one time is limited. Currently, fluorescence activated cell sorting (FACS) is a commonly used method for isolating cell types in a heterogeneous sample⁴. FACS involves the use of antibodies; a primary antibody directly conjugated to a fluorophore, or a secondary antibody conjugated to

a fluorophore against the primary antibody, may be employed. The extensive steps involved in tagging biological samples with multiple antibodies render the technique highly consuming and laborious. Moreover, the fluorescence emission bands in the spectrum are also very broad and often overlap with the emission bands of other fluorophores. The overlapping of broad fluorescent bands limits the number of fluorophores that can be employed in one assay. Vibrational spectroscopy on the other hand, provides a full spectrum of information on the chemical contents during one measurement. It is therefore a very useful technique for detecting numerous types of chemical changes at a time. The full range of spectral information provided also allows the elucidation of chemical variations between samples without knowledge of target molecules *a priori*.

FACS of live cells is mostly limited to using cell surface molecules as markers⁴, since the tagging of cytoplasmic markers would require lysing or punctuation of the cell membrane, which would affect the viability of the cells. Although it is possible to tag biological materials without prior fixation, the effects of the application of exogenous tags to biological samples are not well understood, leading to possibilities of artefacts⁵. As labelling is not required for vibrational spectroscopy, minimal preparation is required. Since the techniques are non-destructive, live cells can be directly studied by Raman spectroscopy^{6,7} or Synchrotron (SR)-FTIR⁸, rendering vibrational spectroscopy a very powerful and valuable tool for recognition of stem cells in the hair follicle.

2.2 FTIR Spectroscopy - background and theory

2.2.1 IR spectroscopy

IR spectroscopy refers to the study of interaction between matter and radiation (in the IR range). Electromagnetic radiation can be thought of both as light particles and waves. When the frequency of the radiation corresponds to the frequency of the vibrational energy of the chemical bond, a transfer of energy takes place, i.e. the energy is absorbed by the molecule and the molecule is promoted to an excited state. The chemical bonds within molecules vibrate at frequencies specific to their molecular structure, thus absorb radiation of specific frequencies. Since most molecular vibrations have energy corresponding to that of the IR region of the electromagnetic spectrum, IR spectroscopy can reveal information of most chemical bonds within the molecules⁹. Through directing a range of IR of different frequen-

cies onto the sample, and measuring the absorption of IR radiation at different wavelengths, a snapshot of the chemical contents of the sample can be provided.

In a simple IR spectrometry set-up, a broad-band source of radiation containing a wide range of IR wavelengths generally of $4000\text{-}200\text{ cm}^{-1}$ ($2.5\text{ - }50\text{ }\mu\text{m}$) is directed on to the sample. Radiation is often expressed in wavelength (λ). In spectroscopy however, radiation is expressed in frequency (ν) or wavenumber ($\tilde{\nu}$) scales which are linearly related to energy. The wavenumber ($\tilde{\nu}$) is the standard unit used by spectroscopists¹⁰. The relationships between λ , ν and $\tilde{\nu}$ are given by:

$$\lambda = \frac{c}{\nu} \quad (2.2.1-1)$$

$$\nu = \frac{\Delta E}{h} \quad (2.2.1-2)$$

$$\tilde{\nu} = \frac{\nu}{c} = \frac{1}{\lambda} \quad (2.2.1-3)$$

where ΔE is the energy between the initial state and the end state (e.g. ground state and excited state), and c is the speed of light.

2.2.2 Selection rules

For IR light absorption to occur, an interaction between an oscillating dipole moment and an oscillating electric vector of the IR radiation is required⁹. The dipole moment during a vibration must change.

2.2.3 Vibrational modes

A molecule has different ‘vibrational modes’. The vibration is a molecule is defined as when the molecule moves while the centre of gravity does not change. In other words, atoms move such that the centre of mass remains fixed in space. When N is the number of atoms in the molecule, there are $3N-5$ degrees of vibrational modes in a linear molecule, and $3N-6$ vibrational modes in a nonlinear molecule. For example, a water molecule, which is nonlinear, has $3 \times 3 - 6 = 3$ vibrational modes.

Vibrations are never localised. In larger molecules, a large number of vibrational modes involve the whole molecule. Some of these molecular vibrations are localised vibrations while others must be considered as vibrations of the entire molecule. The six localised

vibrational modes are symmetric stretching, asymmetric stretching, bending (or scissoring), rocking, twisting and wagging (these are all illustrated in Fig. 1).

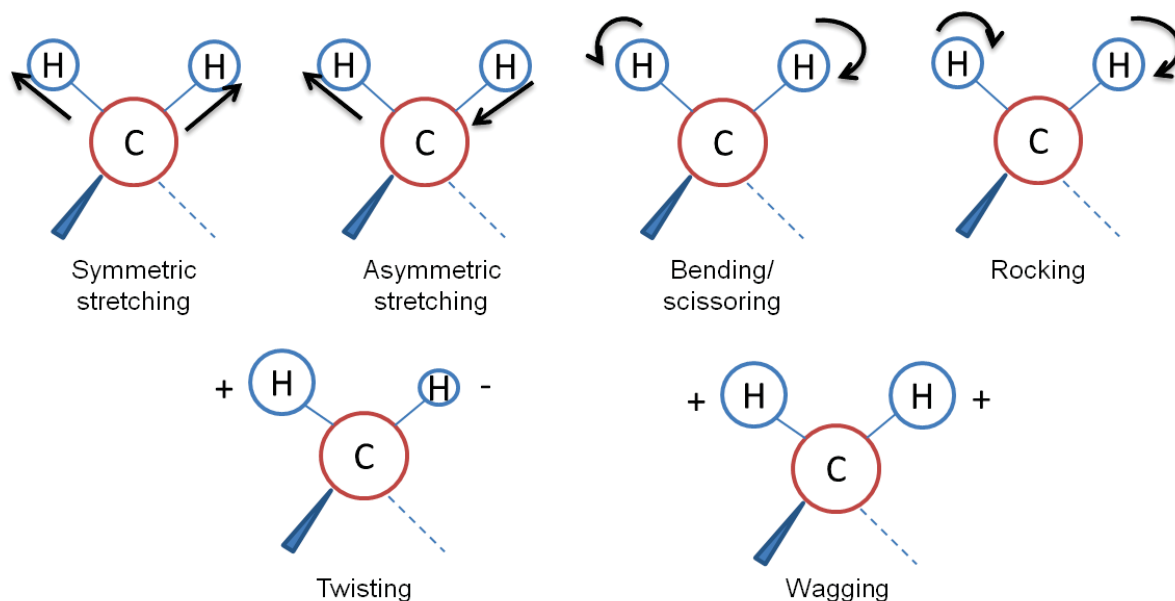


Figure 1. Modes of localised vibrations in a complex molecule are illustrated.

2.2.4 Energy prediction for molecular vibrations

Consider a diatomic molecule as two masses (A and B) connected by a spring, Hooke's law (2.2.4-1) describes the relationship between frequency, the mass of the atoms involved in the vibration and the bond strength:

$$v = \frac{1}{2\pi} \sqrt{\frac{k}{\mu}} \quad (2.2.4-1)$$

where v is the frequency of the vibration, k is the force constant of the bond between A and B. When μ is the reduced mass of atoms A and B of masses M_A and M_B (in g):

$$\mu = \frac{M_A M_B}{M_A + M_B} \quad (2.2.4-2)$$

Substituting Equation 2.2.4-2 into Equation 2.2.4-1 yields:

$$\tilde{\nu} = \frac{1}{2\pi c} \sqrt{\frac{k(M_A + M_B)}{M_A M_B}} \quad (2.2.4-3)$$

where c is the velocity of light (cm/s).

Therefore, the lighter the atoms the higher the frequency, thus C-H vibrations are in the region around 3000 cm^{-1} , while C-C, C-N and C-O vibrations can be found below 1300 cm^{-1} .

2.2.5 IR transmission vs absorption

To obtain the values of IR absorption, the transmittance of IR wavelengths is measured. The transmittance at a given wavenumber is calculated from:

$$T = \frac{I}{I_0} \quad (2.2.5-1)$$

where T is for transmittance, I_0 is the intensity of the incident ray and I is the intensity of the transmitted ray. The absorbance is defined by the Beer-Lambert equation:

$$A = \log_{10} \left(\frac{I_0}{I} \right) = abc \quad (2.2.5-2)$$

where A is the absorbance, a is absorptivity, b is cell thickness, and c is concentration. This implies that the absorbance of IR is linear with the concentration of modes. The Lambert law states that absorption is proportional to the length of the light path, while the Beer law states that absorption is proportional to the concentration of absorbing species in the material.

Both types of spectra are plotted as intensity versus frequency. The transmission spectrum is obtained by plotting the transmittance versus IR wavenumber values (Fig. 2a), and the absorption spectrum is obtained by plotting the absorbance against wavenumber (Fig. 2b), and shows the amount of IR radiation at individual wavenumbers.

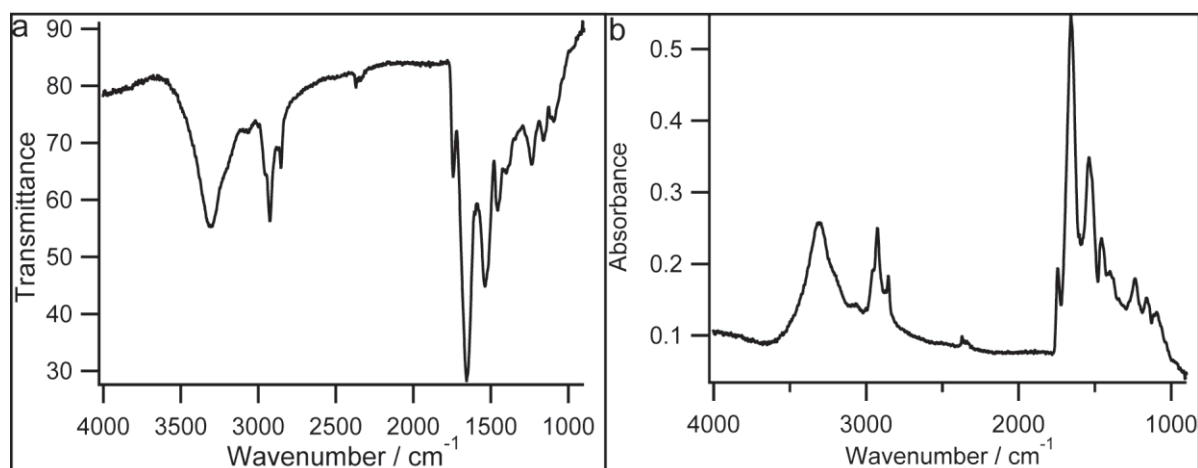


Figure 2a) An example of an IR transmission spectrum collected from a biological sample is shown. **2b)** An IR absorbance spectrum converted from the transmission spectrum shown in 2a.

2.2.6 Fourier transform infrared spectroscopy (FTIR)

FTIR is the preferred type of IR spectroscopy. By incorporating a Michelson interferometer for collecting an interferogram of the sample signal, and transforming the interference into IR spectra by implementing Fourier transformation, the full range of IR frequencies can be simultaneously measured.

The interferometer consists of an IR source, beamsplitter, two mirrors, a laser and a detector. IR radiation from the source is transmitted to the beamsplitter, which splits the beam into two. One of the split beams is reflected at a 90° angle onto a flat fixed mirror, while the other beam is transmitted to a flat mirror which moves back and forth at a constant velocity (Fig.3). The two beams are ultimately reflected from their respective mirrors and are recombined as they re-join at the beamsplitter. Since the distance that one beam travels is fixed, and the other beam reflected back from the moving mirror constantly changes, the recombination of the two beams results in an interference pattern. The resulting interference pattern is called an interferogram. Every data point on the interferogram (a function of the moving mirror position) contains information about every IR frequency from the source. The interferogram is directed from the beamsplitter to the sample, allowing some energy to be absorbed and some to be transmitted. The transmitted energy is subsequently read by the detector and the detector signal is converted into a single beam spectrum by applying Fourier transformation.

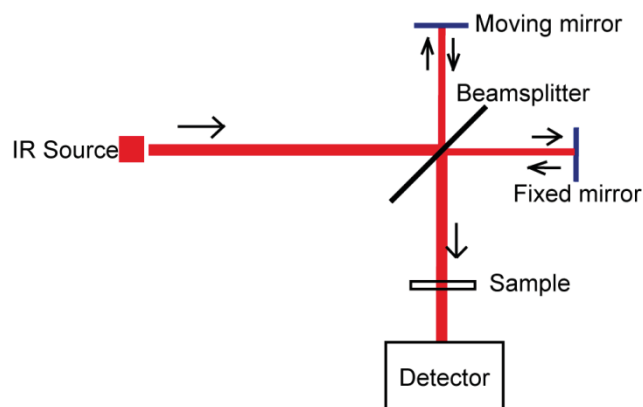


Figure 3. The set-up of an interferometer is illustrated above.

The theoretical resolving power of a Michelson interferometer is given by the number of wavelengths over a certain distance, which is defined by twice the displacement of the moving mirror¹¹:

$$R_0 = \frac{2\Delta l}{\lambda} = 2\Delta l \cdot \tilde{\nu} \quad (2.2.6-1)$$

where R_0 is the resolving power, Δl is the displacement distance of the moving mirror.

The original IR spectroscopy instrument measures both a reference and the sample transmittance so as to take into account the instrumental properties. The sample transmittance is divided by the reference transmittance to obtain an accurate IR spectrum. By splitting one IR beam into two and simultaneously measuring the reference and the sample (Fig.4), any fluctuation in the brightness of the IR source can be discounted. The original IR spectrometer also relies on using a prism or a grating to separate the IR wavelengths from an IR source (Fig.4); the amount of energy at each frequency that has passed through the sample is directed through a slit and measured by the detector one wavelength at a time.

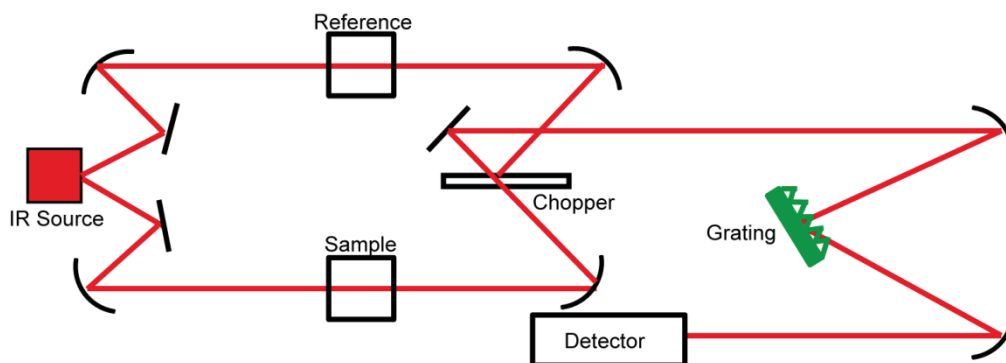


Figure 4. The set-up of a two-beam absorption dispersive IR spectrometer.

Compared to dispersive IR spectrometers, FTIR spectrometers provide higher sensitivity and faster measurement time, as well as higher precision and accuracy of the wavelength positions. Its rapidity also allows a high number of spectra (up to hundreds) to be collected and averaged to provide high signal-to-noise ratio (SNR). It is therefore easy to understand why FTIR is preferred over dispersive IR spectrometers.

2.2.7 FTIR mapping and imaging and spatial resolution

By coupling a FTIR spectrometer to a microscope, FTIR mapping or imaging can be applied to samples to spatially resolve compositional and structural information of biological samples such as tissues^{12, 13}; and to create images based on the intrinsic chemical composition in the IR spectrum. Typically an area is divided into a number of pixels and IR spectra are collected at each pixel. Using the microscopy set up and slits to control the aperture size, the pixel size can be altered to the desired lateral resolution. In FTIR mapping (the point-to-point collection of IR spectra), IR radiation is focused onto the sample through an objective. After the spectrum is collected, the stage moves the next spot into the beam focus for a new spectrum to be collected. The process is repeated until the entire region of interest has been covered; the end result of the mapping is a hyperspectral data cube containing the x, y coordinates of the map and IR spectra at each pixel¹⁴. ‘FTIR imaging’ can technically only be applied when an image of the sample is focused onto an array detector¹⁴. A focal plane array (FPA) detector employed for FTIR imaging usually comes with 64×64 or 128×128 pixels. During FTIR imaging the transmission of IR radiation at each pixel is measured. All the spectra in the map are therefore collected simultaneously.

In FTIR mapping or imaging, the lateral resolution is one of the most critical issues determining the subject of study. A high spatial resolution is required to resolve chemical variations between cell types, whereas for gross morphological examination of tissues a lower spatial resolution may suffice. In any type of optical microscopy the spatial resolution is limited by the diffraction limit of light. Consider a series of concentric rings of decreasing intensity is observed when monochromatic light is passed from a point source through a small circular aperture. The central bright circular region of the pattern is called the Airy disk, of which the radius depends on the wavelength of the radiation and the optics of the microscope. The radius of the Airy disk is defined by the distance between the central maximum and the first minimum of the diffraction pattern. The diffraction limit is given by Abbe's Law of limiting resolution¹⁵:

$$d = \frac{\lambda}{2 NA} \quad (2.2.7-1)$$

where d is the minimum resolving distance, λ is the wavelength of the radiation. NA is the numerical aperture of the objective and is defined as:

$$NA = n \sin\theta \quad (2.2.7-2)$$

where θ is the angle of acceptance of the objective, n is the refractive index of the medium between the objective and the specimen (for air, $n=1$)¹². Therefore spatial resolution is limited by the wavelengths in the mid-IR range ($\lambda = 2.5\text{-}10 \mu\text{m}$).

When the pixel size of the imaging system is smaller than the wavelength of light being used to measure the sample, the system is said to be 'diffraction-limited'. Conversely, when the pixel size is larger than the wavelength of light being used to measure the sample, the system is said to be 'pixel size-limited'¹⁴.

In FTIR mapping or single point collection, the aperture size can be reduced according to the desired lateral resolution. However, reducing the aperture size limits the signal, leading to compromised signal to noise ratio (SNR). The SNR may be improved by increasing the number of spectral accumulations at each pixel, but this lengthens the collection time. FTIR imaging utilises a focal plane array (FPA) detector with fixed physical pixel size predetermined by the manufacturer. Although some FPA imaging systems report a pixel size of down to $1.1 \mu\text{m}$ when a $36\times$ objective is employed, the spatial resolution is, in actual facts, still restricted by the diffraction limit of the radiation.

2.3 Raman spectroscopy – background and theory

2.3.1 Raman microspectroscopy and mapping

Raman spectroscopy measures the inelastic scattering of light. Generally, the inelastic scattering of light is a highly inefficient process. Raman spectrometers therefore employ high power light sources (typically a laser) to increase the signal. By focusing the laser light onto the sample through a microscope lens, the area from which Raman signals are collected can be selected. This technique is called Raman microspectroscopy. The coupling of a Raman spectrometer to confocal microscope renders it possible to achieve spatial resolution of $< 1 \mu\text{m}$, depending on the excitation wavelength. In a similar fashion to FTIR mapping, Raman mapping collects a series of Raman spectra from adjacent loci of a sample over a predefined area. Based on the Raman bands in the spectra, Raman images can be plotted reflecting the chemical and structural composition of the sampled area. Therefore, Raman microspectroscopy imaging provides a means to obtain information of the chemical composition of materials with high spatial resolution. It is a highly advantageous technique for resolving differences from one cell to another, as well as chemical variations within the cells.

2.3.2 Raman theory

The interaction of a photon and a molecule result in elastic scattering (Rayleigh) and inelastic scattering (Raman). As the electromagnetic radiation interacts with matter, it causes distortions to the electrons cloud around the nuclei of molecules. The distortion of the electron cloud results in a periodic separation of charge within the molecules, i.e. an induced dipole moment.

The strength of the induced dipole moment, P , depends on the polarisability of the molecule and the strength of the electric field. Polarisability describes the ability of the electrons in the molecule to polarise, i.e. to what degree the electron cloud is distorted during the interaction between linearly polarised light and the molecule¹⁶.

Polarisability depends on the structure of the molecule and the nature of the bonds. It is given by:

$$P = \alpha \bar{E} \quad (2.3.2-1)$$

where α is the polarisability of the molecule, and \bar{E} is the strength of the electric field of the electromagnetic wave.

For the incident electromagnetic wave, the electric field can be expressed as:

$$\bar{E} = E_0 \cos(2\pi\nu_0 t) \quad (2.3.2-2)$$

where E_0 is the frequency of the incident light ($E_0 = c/\lambda$). Substituting Equation 2.3.2-2 into Equation 2.3.2-1, the time-dependent induced dipole moment is yielded:

$$P = \alpha E_0 \cos(2\pi\nu_0 t) \quad (2.3.2-3)$$

The ability to distort the local electron cloud of a molecule is dependent on the relative position of the individual atoms; therefore polarisability is also a function of the momentary position of the atoms. The vibrational energy of a specific vibrational mode is given by:

$$E_{vib} = \left(n + \frac{1}{2}\right) h\nu_{vib} \quad (2.3.2-4)$$

where n is the vibrational quantum number ($n = 0, 1, 2, \dots$), ν_{vib} is the frequency of the vibrational mode, and h is the Planck constant. The physical displacement dQ of the atoms about their equilibrium position caused by specific vibrational modes may be expressed as:

$$dQ = Q_0 \cos(2\pi\nu_{vib} t) \quad (2.3.2-5)$$

where Q_0 is the maximum displacement about the equilibrium position. For typical diatomic molecules, the maximum displacement is about 10% of the bond length. The polarisability for such small displacements may be approximated by a Taylor series expansion:

$$\alpha = \alpha_0 + \frac{\partial\alpha}{\partial Q} dQ \quad (2.3.2-6)$$

where α_0 is the polarisability of the molecular mode at equilibrium position. Substituting Equation 2.3.2-5 into 2.3.2-6, the polarisability may be expressed as:

$$\alpha = \alpha_0 + \frac{\partial\alpha}{\partial Q} Q_0 \cos(2\pi\nu_{vib} t). \quad (2.3.2-7)$$

Finally, substituting Equation 2.3.2-7 into Equation 2.3.2-3 yields:

$$P = \alpha_0 E_0 \cos(2\pi\nu_0 t) + \frac{\partial\alpha}{\partial Q} Q_0 E_0 \cos(2\pi\nu_0 t) \cos(2\pi\nu_{vib} t). \quad (2.3.2-8)$$

Using a trigonometric identity, the above relation may be simplified to:

$$P = \alpha_0 E_0 \cos(2\pi\nu_0 t) + \left[\frac{\partial \alpha}{\partial Q} \frac{Q_0 E_0}{2} \right] \{ \cos[2\pi(\nu_0 - \nu_{vib})t] + \cos[2\pi(\nu_0 + \nu_{vib})t] \}. \quad (2.3.2-9)$$

According to Equation 2.3.2-9, induced dipole moments are created at three distinct frequencies ν_0 , $(\nu_0 - \nu_{vib})$ and $(\nu_0 + \nu_{vib})$, where scattered radiation occurs. ν_0 corresponds to the incident frequency of the excitation source. Light scattered at the same frequency as the incident light (ν_0) is known as Rayleigh scattering and is the dominant type of light scattering¹⁷ (Fig.5). In one in $1 \times 10^6 - 10^8$ events, the scattered light contains lower energy (longer wavelength) than the incident light ($\nu_0 - \nu_{vib}$); this is called Stokes (Fig.5). Even more rarely, molecules can be at an excited vibrational state due to thermal energy, and may return to the ground state after the interaction with light. During such an event, energy is transferred from the molecule to the scattered photon ($\nu_0 + \nu_{vib}$). Such an event is called anti-Stokes scattering¹⁷ (Fig.5).

According to Equation 2.2.1-2, the energy change between vibrational states (m to n in Figure 5) may be expressed as:

$$\Delta E = h\nu_{vib}. \quad (2.3.2-10)$$

Since most molecules are much more likely to be found in the ground vibrational state, Stokes scattering is more probable than anti-Stokes scattering.

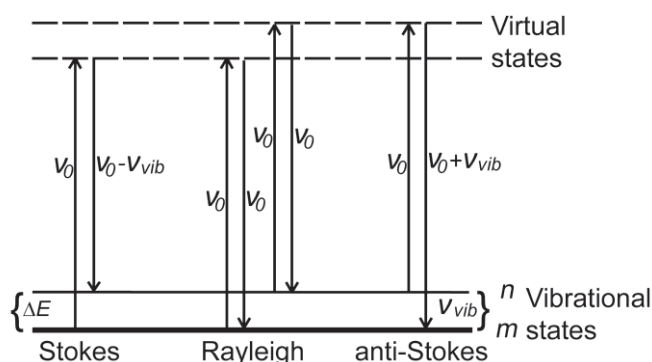


Figure 5. Schematic of the Rayleigh and Raman scattering processes. The lowest vibrational energy state m , represents the ground vibrational state of molecules. Above m is the excited vibrational state n with a higher energy. The molecule may be promoted to a virtual state transiently and return to a higher energy state (as in Stokes), the same energy state as before (as in Rayleigh), or to a lower energy state (as in anti-Stokes).

2.3.3 Raman Intensity

The Raman differential scattering cross-section (cm^2/sr) varies inversely with the fourth power of the excitation wavelength by the proportionality formula¹⁸. The Raman intensity can be calculated by:

$$\sigma' \propto (\tilde{\nu}_0 - \tilde{\nu}_{vib})^4 \quad (2.3.3-1)$$

where $\tilde{\nu}_0$ is the wavenumber of the exciting light ($1/\lambda_0$), and $\tilde{\nu}_{vib}$ is the wavenumber of the vibrational mode (ν_{vib}/c).

2.3.4 Conventions

Raman scattering is expressed as a shift in wavenumber from the wavenumber of the incident photon, and is expressed as cm^{-1} . For most biological samples, the region of Raman shift which is most interesting or contains the most useful information, is between $400\text{-}3600 \text{ cm}^{-1}$.

2.3.5 Coupling Raman spectroscopy to microscopy and Raman spectroscopic imaging

The greatest advantage of coupling Raman spectroscopy to a microscope, is that Raman measurement can be carried out in a confocal manner, allowing the laser beam to be tightly focused onto a sample. A tight laser beam focus greatly improves the efficiency of Raman scatter collection.

In a confocal design, the laser beam fills the back of the microscope objective lens aperture (Fig. 6, 03), optimising the beam profile and presenting a diffraction-limited source. The beam is tightly focused by an objective lens (Fig. 6, 03) with a large numerical aperture (NA) onto a small focal volume in the sample. The same objective lens then collects a mixture of Raman and Rayleigh scattered light from the excited spot. As explained in (2.2.6-2) an objective lens with a high NA has a large angle of acceptance, thus it collects a higher percentage of the scattered light (which scatters in all directions)¹⁷. The collected light is typically filtered by a notch filter or an edge filter (Fig. 6, EF), reflecting the Rayleigh line and transmitting the Stokes-shifted Raman-scattered radiation. Before reaching the detector, the collected light is passed through a pinhole (Fig.6), so that scattered light collected from out of focus is rejected, enhancing the confocality.

The design of an Alpha300 WITec (WITec, Germany) confocal Raman microscope using an upright microscope is illustrated in Figure 6. It consists of a laser source (01). The emitted

laser beam becomes collimated before entering the microscopy system through an optical fibre (02, OF). A band pass filter (BPF) filters out light that is out of the intended range of wavelengths for Raman excitation. The laser light is reflected towards the sample by a mirror (beam splitter, BS) through an objective lens (03) onto the sample stage (04). The focused laser beam causes excitation within the focal volume in the sample. The scattered light is collected by the objective lens and directed towards the CCD detector (08) passing through a Rayleigh filter (05, edge filter, EF), a pinhole, an optical fibre (06, OF) and a lens based spectrometer system (07). The spectrometer typically constitutes a grating for separating the wavelengths so that the intensity at each wavelength is measured.

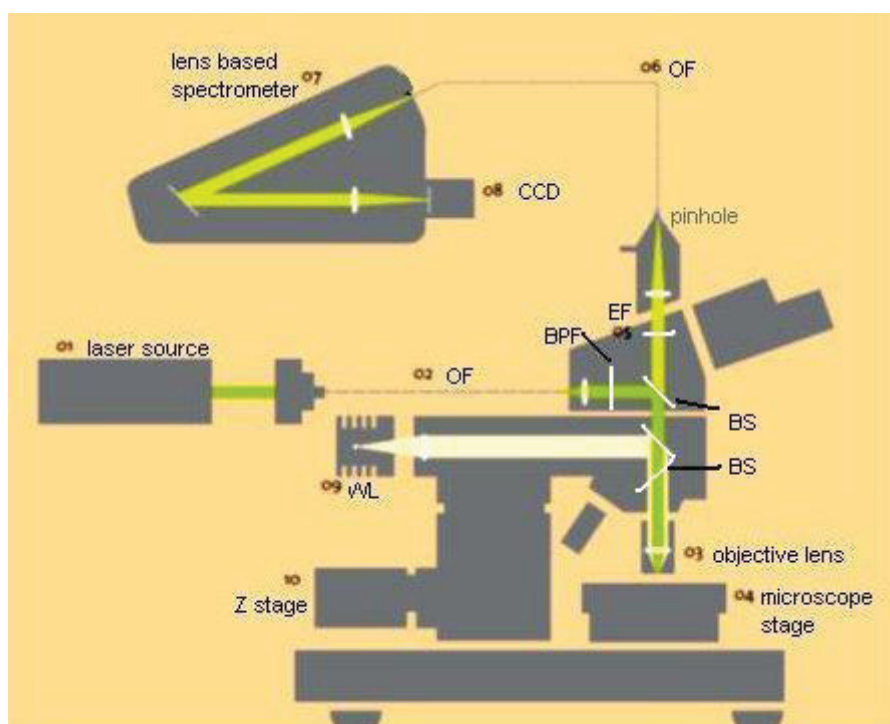


Figure 6. An alpha300R WITec Raman microscope. The beam describes the pathway of the laser beam from its source to the sample and to the CCD detector. 01: laser source; 02: optical fibre (OF); 03: objective lens, for focusing white light (WL) and laser beam onto the sample; 04: microscope stage, where the sample rests; 05: Rayleigh/band pass filter (BPF); 06: optical fibre (OF); 07: lens based spectrometer; 08: CCD detector; 09: white light (WL) illuminator, for white light microscopy of the sample; 10: Z-stage for focusing. (Image adapted from alpha300 R flyer, www.witec.de)

Coupling Raman microspectroscopy to a motorised stage enables Raman spectroscopic imaging. Similar to the idea of FTIR mapping, Raman mapping collects Raman spectra from each pixel in a defined area of the sample. The spectral data can be used for univariate and multivariate analyses, thus creating Raman images revealing information on the chemical composition in the mapped area of the sample.

Since Raman microspectroscopy offers higher spatial resolution than FTIR spectroscopy imaging techniques, subcellular contents can also be investigated (Fig.7). Therefore, Raman microspectroscopy is a suitable and useful technique for characterising cell populations and can potentially be used as a tool for recognising stem cells within their tissue environment.

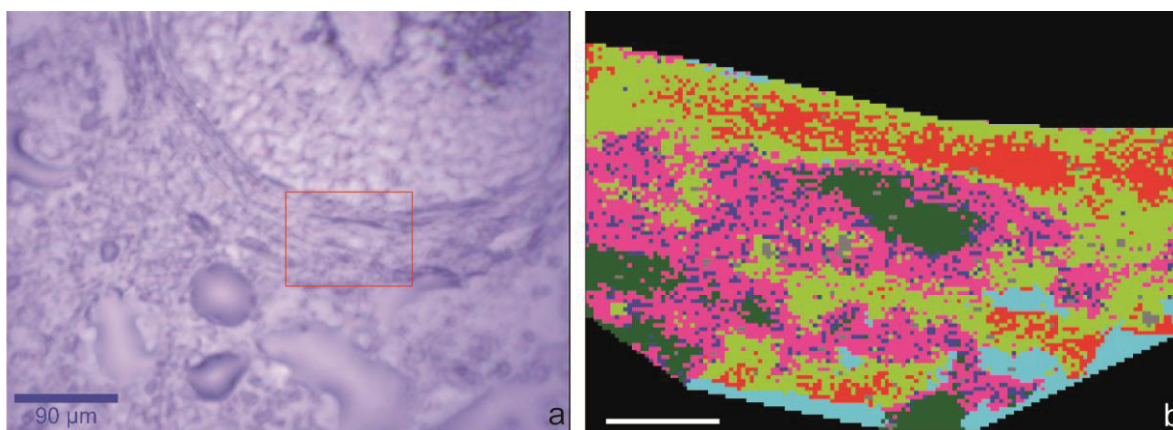


Figure 7a) A white light image of a lower human hair follicle on which Raman mapping was performed. Part of the lower CTS (demarcated in red box) was mapped using a confocal Raman imaging system (WITec, Ulm, Germany), with a 514 nm laser source with a 20× NA 0.4 objective. Scale bar: 90 μm. **7b)** A Raman image obtained from UHCA on the Raman data within the CTS area of the map. According to the average spectra (not shown), the green cluster represents nuclei, the pink cluster represents cytoplasm and the blue cluster represents glycoproteins. Red and light green clusters represent extracellular matrix proteins. The Raman map collected at subcellular spatial resolution allows cellular components to be differentiated from one another, and from extracellular matrix (ECM) components. Scale bar: 20 μm. Ref¹⁹.

2.4 Examples of application of vibrational spectroscopy to skin and hair

The application of FTIR and Raman spectroscopies to studying skin has become increasingly popular over the last decade. FTIR techniques including SR-, FPA- and attenuated total reflection (ATR)- FTIR (coupled to FTIR spectroscopy to enhance the SNR in the spectra and spatial resolution) have been successfully applied to studies on skin²⁰⁻²⁵ as well as hair fibre^{26, 27}. FPA-FTIR employs a FPA detector which simultaneously records spectra from 64 × 64 or 128 × 128 points depending on the size of the detector, enabling rapid spectral recording of material with a reasonable co-add scans number to enhance the signal-to-noise ratio²⁸. Using an FPA-FTIR instrument, the potentials of using FTIR microspectroscopy to investigate dermal drug delivery mechanisms were investigated²⁴. It was shown that mapping of exogenous materials in skin by FTIR is highly feasible. Skin treated with deuterated propylene glycol and dime-thylsulphoxide was sectioned, FTIR-imaged according to various bands including a C-D stretching band in the 2300-2000 cm⁻¹ region²⁶. ATR-FTIR

uses an internal reflectance element, with a high refractive index, to provide total multiple reflection of the incident IR radiation within the element. This provides penetration depth of about 1-3 μm , though it varies slightly depending on the type of ATR crystal, the angle of incidence and wavelength of the light²⁹. When the internal reflectance element is placed on the sample, IR radiation can penetrate into the surface of the sample to a certain derivable depth. Therefore, the technique is suitable for obtaining spectra from the skin surface, such as the *Stratum corneum* and hair fibres. Using ATR-FTIR, the lipid organisation in the *S. corneum* of human skin, porcine skin, reconstructed epidermis²³ and skin substitutes used as psoriatic skin models³⁰ *in vitro* were compared³¹. In addition, through ATR-FTIR applied to human skin at different locations of the body *in vivo* and tape stripping, the distribution of lipid and hydration levels in the *S. corneum* was found to be inhomogeneous²⁴.

As Raman spectroscopy can be coupled to confocal microscopy, the application to confocal Raman spectroscopy to skin can yield chemical information of the skin at predefined depths. This contributes to the possibility of investigation of substances in skin *in vivo* and has thus gained popularity among dermatologists in the cosmetic industry³²⁻³⁸. Through the application of confocal Raman spectroscopy to skin *in vivo*, it is possible to assess a number of factors. These are:

- the penetration ability of oils^{34, 36},
- the effects of moisturising agents^{37, 38},
- concentration of water, lipids, natural moisturising factors for the *S. corneum* (peptides in the *S. corneum* that have water retaining properties)³⁵ and the dermis³²,
- distribution of carotenoids as a marker of antioxidative potential in human skin³³,
- molecular evaluation of wound healing of guinea pig skin³⁹.

Despite the above examples, the application of vibrational spectroscopy to demarcating and characterising hair follicle tissue compartments, as well as the cell types within, was unprecedented.

2.5 Examples of application of vibrational spectroscopy to stem cells

FTIR and Raman spectroscopies have begun to be applied to stem cell studies in the 2000's⁴⁰⁻⁴⁵. One of the first vibration spectroscopic studies on embryonic stem cells (ESCs) was the application of Raman spectroscopy to murine embryonic stem cells (mESCs) by Notingher *et*

*at*⁴³. As mESCs were allowed to differentiate spontaneously *in vitro* over 20 days, decrease in RNA and increase proteins were found as differentiation proceeded⁴³ corresponding to translational activity from pre-existing messenger RNA (mRNA) as differentiation occurs. Using FTIR spectroscopy, spectra collected from mESC demonstrated consistency with the Raman data described above study in that RNA levels were found to decrease while protein levels increased⁴¹. It was also found that the secondary structures of the proteins switched during differentiation indicating that specific proteins were synthesised⁴¹. Furthermore, DNA/RNA hybrid was detected from day 7 after spontaneous differentiation began, signifying *de novo* transcription took place⁴¹. Recently, SR-FTIR was applied to human embryonic stem cell (hESC) to reveal the chemical modifications that take place during early hESC differentiation towards mesendoderm and ectoderm⁴⁶. While this study found that lipid levels decreased significantly during early differentiation⁴⁶, a study which employed SR-FTIR on the neural differentiation of mESCs indicated lipid levels increased during the differentiation⁴⁷. A change from β -sheet secondary structure predominance to α -helix was also registered⁴⁷. Specific chemical modifications that consistently occur during differentiation can be established as spectral signatures. Establishment of signature spectral features can help differentiate stem cells from non-stem cells. Such was the aim of a study applying Raman spectroscopy to discerning hESCs from their cardiomyocyte derivatives⁴⁸. As cardiomyocytes presently have no surface antigen markers^{48,49}, establishing spectral markers for their discernment from undifferentiated hESCs potentially facilitates the use of cardiomyocytes differentiated from hESCs for stem cell based heart therapies^{6,48}. Recently, confocal Raman microspectral imaging was applied to mESCs, resulting in sub-cellular resolution imaging, presenting spectral changes between organelles⁵⁰.

Aside from ESCs, vibrational spectroscopy has also been applied to adult stem cells (ASCs)^{45, 51-53}. FTIR spectroscopy revealed that human mesenchymal stem cell (hMSC) contains higher levels of glycogen, possibly as energy storage, before directed differentiation to osteocytes⁵². FTIR studies on intestinal crypt stem cells revealed structural differences in chromatin between stem cells and transient amplifying (TA) cells and proposed the symmetric PO_2^- band at 1080 cm^{-1} to be an intestinal crypt stem cell spectral marker⁴⁵. Another study using SR-FTIR on human corneal stem cells also associated symmetric and asymmetric phosphate bands with stem cells, as opposed to TA cells.

2.6 Conclusion

Given these examples, the application of FTIR and Raman spectroscopies to hair follicle stem cells, combined with powerful statistical evaluation tools, is likely to yield spectral markers that can differentiate stem cells from their less naïve counterparts.

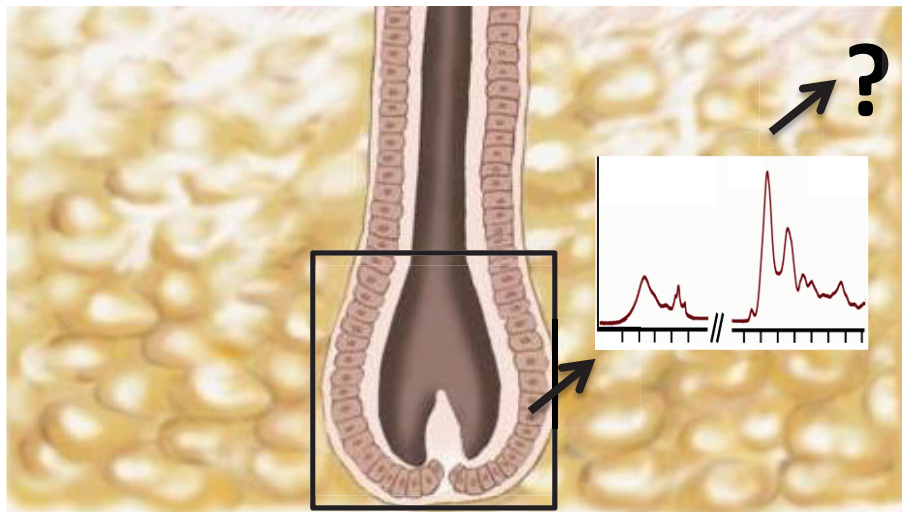
References

1. J. E. Kloepper, S. Tiede, J. Brinckmann, D. P. Reinhardt, R. Faessler and R. Paus, *Exp Dermatol.*, 2008, **17**, 592-609.
2. R. K. Sivamani, M. P. Schwartz, K. S. Anseth and R. R. Isseroff, *FASEB J*, 2011, **25**, 122-131.
3. L. Kuerschner, C. S. Ejsing, K. Ekroos, A. Shevchenko, K. I. Anderson and C. Thiele, *Nat. Methods*, 2005, **2**, 39-45.
4. H. Fukuda, J. Takahashi, K. Watanabe, H. Hayashi, A. Morizane, M. Koyanagi, Y. Sasai and N. Hashimoto, *Stem Cells*, 2006, **24**, 763-771.
5. T. T. Le, S. Yue and J.-X. Cheng, *J. Lipid Res.*, 2010, **51**, 3091-3102.
6. F. C. Pascut, H. T. Goh, N. Welch, L. D. Buttery, C. Denning and I. Notingher, *Biophys J*, 2011, **100**, 251-259.
7. A. Bankapur, E. Zachariah, S. Chidangil, M. Valiathan and D. Mathur, *PLoS ONE*, 2010, **5**, e10427.
8. H.-Y. N. Holman, K. A. Bjornstad, M. P. McNamara, M. C. Martin, W. R. McKinney and E. A. Blakely, *J Biomed Opt*, 2002, **7**, 417-424.
9. H. W. Dudley and I. Fleming, in *Spectroscopic methods in organic chemistry*. H. W. Dudley and I. Fleming, The McGraw-Hill Companies, London, Editon 5, 1995, pp. 28-62.
10. D. Lin-Vien, N. B. Colthup, W. G. Fateley and J. G. Grasselli, in *The Handbook of Infrared and Raman Characteristic Frequencies of Organic Molecules*. D. Lin-Vien, N. B. Colthup, W. G. Fateley and J. G. Grasselli, Academic Press, London, 1991, pp. 1-7.
11. B. Schrader, in *Infrared and Raman Spectroscopy*, ed. B. Schrader, VCH, Weinheim, 1995, pp. 63-186.
12. P. Lasch and D. Naumann, *BBA*, 2006, 1758, 814-829.
13. B. R. Wood, L. Chiriboga, H. Yee, M. A. Quinn, D. McNaughton and M. Diem, *Gynecol Oncol*, 2004, **93**, 59-68.
14. P. R. Griffiths, in *Infrared and Raman Spectroscopic Imaging*, eds. R. Salzer and H. W. Siesler, Wiley-VCH, Weinheim, 2009, pp. 3-64.
15. E. Abbe, *J. R. Microsc. Soc.*, 1883, **23**, 790-812
16. E. Smith and G. Dent, in *Modern Raman Spectroscopy - A Practical Approach*. E. Smith and G. Dent, Wiley, Chichester, England, 2005, pp. 71-91.
17. E. Smith and G. Dent, in *Modern Raman Spectroscopy - A Practical Approach*. E. Smith and G. Dent, Wiley, Chichester, England, 2005, pp. 1-20.
18. M. Diem, in *Introduction to Modern Vibrational Spectroscopy*. M. Diem, Wiley-Interscience, New York, 1993, pp. 109-144.
19. K. Lau, C. Mattheaus, J. Popp, J. E. Kloepper, R. Paus and V. Deckert, in *ICORS Conference Programme*, Boston, Massachusetts, USA, 2010.
20. J.-M. Andanson, K. L. A. Chan and S. G. Kazarian, *App Spectrosc*, 2009, **63**, 512-517.
21. M. Cotte, P. Walter, G. Tsoucaris and P. Dumas, *Vib Spectrosc*, 2005, **38**, 159-167.
22. B. W. Barry, H. G. M. Edwards and A. C. Williams, *J Raman Spectrosc*, 1992, **23**, 641-645.
23. M. Boncheva, F. Damien and V. Normand, *BBA*, 2008, **1778**, 1344-1355.
24. L. Brancalton, M. P. Bamberg, T. Sakamaki and N. Kollias, *J Invest Dermatol*, 2001, **116**, 380-386.
25. R. Mendelsohn, H.-C. Chen, M. E. Rerek and D. J. Moore, *J Biomed Opt*, 2003, **8**, 185-190.
26. D. J. M.-W. Lyman, Jacqueline *App Spectrosc*, 2005, **59**, 26-32.
27. K. L. A. T. Chan, Feng H.; Taylor, Cheryl; Kazarian, Sergei G., *App Spectrosc*, 2008, **62**, 1041-1044.
28. B. R. Wood and D. McNaughton, in *Spectrochemical Analyses Using Multichannel Infrared Detectors*, eds. R. Bhargava and I. Levin, Blackwell, Oxford, 2005.
29. S. G. Kazarian, K. L. A. Chan and F. H. Tay, in *Infrared and Raman Spectroscopic Imaging*. R. Salzer and H. W. Siesler, Wiley, Weinheim, 2009, Vol. 1, pp. 347-376.
30. G. Bernard, M. Auger, J. Soucy and R. Pouliot, *BBA*, 2007, **1770**, 1317-1323.
31. S. L. K. Krill, K. ; Higuchi, W. J. , *BBA*, 1992, **1112**, 281-286
32. N. Nakawaga, M. Matsumoto and S. Sakai, *Skin Res Technol*, 2010, **16**, 137-141.

33. M. E. Darvin, J. W. Fluhr, P. Caspers, A. van der Pool, H. Richter, A. Patzelt, W. Sterry and J. Lademann, *Exp Dermatol*, 2009, **18**, 1060-1063.
34. P. D. A. Pudney, M. Melot, P. J. Caspers, A. van der Pool and G. J. Puppels, *Appl Spectrosc*, 2007, **61**, 804-811.
35. P. J. Caspers, G. W. Lucassen and G. J. Puppels, *Biophys J*, 2003, **85**, 572-580.
36. G. N. Stamatias, J. de Sterke, M. Hauser, O. von Stetten and A. van der Pol, *J Dermatol Sci*, 2008, **50**, 135-142.
37. L. Chrit, P. Bastien, B. Biatry, J.-T. Simonnet, A. Potter, A. M. Minondo, F. Flament, R. Bazin, G. D. Sockalingum, F. Leroy, M. Manfait and C. Hadjur, *Biopolymers*, 2007, **85**, 359-369.
38. J. M. Crowther, A. Sieg, P. Blenkiron, C. Marcott, P. J. Matts, J. R. Kaczvinsky and A. V. Rawlings, *Br J Dermatol*, 2008, **159**, 567-577.
39. A. Alimova, R. Chakraverty, R. Muthukattil, S. Elder, A. Katz, V. Sriramoju, S. Lipper and R. R. Alfano, *J Photochem Photobiol B*, 2009, **96**, 178-183.
40. J. W. Chan, D. K. Lieu, T. Huser and R. A. Li, *Anal. Chem.*, 2009, **81**, 1324-1331.
41. D. Ami, T. Neri, A. Natalello, P. Mereghetti, S. M. Doglia, M. Zanoni, M. Zuccotti, S. Garagna and C. A. Redi, *BBA*, 2008, **1783**, 98-106.
42. C. Krafft, R. Salzer, S. Seitz, C. Ern and M. Schieker, *Analyst*, 2007, **132**, 647-653.
43. I. Notingher, I. Bisson, A. E. Bishop, W. L. Randle, J. M. P. Polak and L. L. Hench, *Anal Chem*, 2004, **76**, 3185-3193.
44. M. J. Walsh, A. Hammiche, T. G. Fellous, J. M. Nicholson, M. Cotte, J. Susini, N. J. Fullwood, P. L. Martin-Hirsch, M. R. Alison and F. L. Martin, *Stem Cell Res*, 2009, **3**, 15-27.
45. M. J. Walsh, T. G. Fellous, A. Hammiche, N. J. Fullwood, O. Grude, F. Bahrami, J. M. Nicholson, H. M. Pollock, M. Brittan, P. L. Martin-Hirsch, M. R. Alison and F. L. Martin, *Stem Cells*, 2008, **26**, 108-118.
46. P. Heraud, E. S. Ng, S. Caine, Q. C. Yu, C. Hirst, R. Mayberry, A. Bruce, B. R. Wood, D. McNaughton, E. G. Stanley and A. G. Elefanty, *Stem Cell Res.*, 2010, **4**, 140-147.
47. W. Tanthanuch, K. Thumanu, C. Lorthongpanich, R. Parnpai and P. Heraud, *J Mol Struct*, 2010, **967**, 189-195.
48. J. W. Chan, D. K. Lieu, T. Huser and R. A. Li, *Anal Chem*, 2009, **81**, 1324-1331.
49. F. C. Pascut, H. T. Goh, N. Welch, L. D. Buttery, C. Denning and I. Notingher, *Biophys J*, 2011, **100**, 1-9.
50. E. Zuser, T. Chernenko, J. Newmark, M. Miljkovic and M. Diem, *Analyst*, 2010, **135**, 3030-3033.
51. A. J. Bentley, T. Nakamura, A. Hammiche, H. M. Pollock, F. L. Martin, S. Kinoshita and N. J. Fullwood, *Mol Vis*, 2007, **13**, 237-242.
52. C. Krafft, R. Salzer, S. Seitz, C. Ern and M. Schieker, *Analyst*, 2007, **132**, 647-653.
53. T. Nakamura, J. G. Kelly, J. Trevisan, L. J. Cooper, A. J. Bentley, P. L. Carmichael, A. D. Scott, M. Cotte, J. Susini, P. L. Martin-Hirsch, S. Kinoshita, N. J. Fullwood and F. L. Martin, *Mol Vis*, 2010, **16**, 359-368.

Chapter 3

Proof of Principle: Application of FTIR mapping and N-FINDR algorithm to demarcating tissue compartments within the human hair follicle bulb



3.1 Abstract

In this thesis, Fourier transform infrared (FTIR) spectroscopy is proposed as a hair follicle stem cell identification method. As a first step, FTIR spectroscopic imaging is applied to the hair follicle in human scalp skin, to demonstrate that it is feasible to define hair follicular structure based on spectral variations. The use of FTIR spectroscopy as a label-free, minimally sample destructive method to has been explored and demonstrated in this chapter. Human scalp skin cryosections were imaged using FTIR microscopy and the data was subsequently analysed with N-FINDR spectral unmixing algorithm. This resulted in an excellent distinction of known hair follicle tissue layers, which could be discerned based on their molecular structure. Conclusion: The development of a minimally sample destructive, label free spectroscopy based technique that can differentiate layers of cells in the dermal papilla (DP) and connective tissue sheath (CTS) in the mesenchyme of the hair follicle paves way towards identifying spectral markers important in wound healing and stem cell therapies. The work presented here within has been submitted as an original article and has been accepted (Ref¹).

3.2 Introduction

FTIR spectroscopy has been proposed as a label-free and minimally invasive method for hair follicle stem cell identification. To realise this goal, FTIR spectroscopic imaging is first applied to hair follicles in skin sections, to demonstrate that tissue or cell types can be distinguished based on their spectral variations.

Defining skin architecture and characterising its appendages usually require the tissue to be destroyed and labelled. For efficient use of such precious tissue samples, a label-free intravital method to image and characterise the skin and its appendages is required. The hair follicle is an optimal model system for exploring such label-free tissue/cell imaging and characterisation methods, as the hair follicle has a defined and well characterised anatomical structure, and its cell types are well studied. Distinct cell types are clearly segregated in their respective compartments.

While staining the hair follicle sections with haematoxylin and eosin allows clear visualisation of the different follicular compartments, it does not present their molecular features. Immunohistochemistry utilising specific antibodies permits the elucidation of information of specific proteins but prior knowledge is required and is a largely time-consuming and laborious process. Vibrational spectroscopy, on the contrary, allows the examination of molecular contents in a cell/tissue sample without labelling or prior knowledge of the cells².

Analyses of infrared (IR) spectra from biological samples can yield information on their contents in terms of proteins, nucleic acids, lipids and carbohydrates. Information on the conformation of lipids, proteins and nucleic acids can furthermore be extracted, by analysing their 'signature bands'. For example, the secondary structure of the proteins can be deduced by the position of maximum IR absorptions in the amide I and amide II bands^{3,4}. By further use of multivariate data analysis, major differences in the 'finger print' region (around 1800-800 cm^{-1}) between samples can be revealed. Such combinations of techniques are extremely powerful for identifying 'abnormal' cells in a tissue sample, such as malignant cells⁵⁻⁷ and for analysing the molecular differences between stem/progenitor cells and their more mature counterparts^{3,8-10}.

The aim of this work is to explore the potential use of FTIR spectroscopy to study single cells in the hair follicle, first by examining the employability of FTIR microspectroscopy and multivariate data analyses for discerning the tissue layers of the hair follicle, purely by means of their spectral differences. In this study we implemented N-FINDR spectral unmixing algorithm to achieve this¹¹. Briefly, N-FINDR determines the most extreme or pure spectra within the data set, which are termed 'endmembers' (further elaborated in Methods)¹¹. Secondly, it was examined whether the locality of the so-called endmembers provided by this spectral unmixing algorithm matched the positions of the tissue layers in the visible image. Thirdly, the level of correlation between the spectral features and the biological features of each compartment was inspected.

The hair bulb is of particular interest since it contains the CTS and the DP where multipotent stem cells are located¹²⁻¹⁶. The distinct cell populations in different compartments—epithelial cells, CTS cells, DP cells and adipose tissue— further rendered the hair bulb suitable for addressing the above-mentioned questions we aimed to tackle.

Although previously a lateral cross-section of a hair follicle has been imaged using FTIR¹⁷, it was neither characterised nor were the tissue compartments defined by the collected spectra. To our knowledge, this is the first reported work on using FTIR and multivariate analysis to discern tissue layers in a longitudinal hair bulb section. This report illustrates the biomolecular information extracted from the spectra of the individual clusters from the FTIR map, and discusses their biological significance in relationship to function. Four samples originating from the two different patients and different hair follicles were examined to confirm the reproducibility of the employed method.

3.3 Materials and Methods

3.3.1 Sample origin

Human scalp skin was donated by routine facelift plastic surgery patients. All experiments were carried out according to the Helsinki guidelines, in compliance with national regulations for the experimental use of human material. The excised skin strips were transported in Williams E medium (Biochrom, Cambridge, UK) on ice and were subsequently cut into blocks before snap-freezing in liquid nitrogen and stored at -80°C.

3.3.2 Skin section preparation

Snap-frozen skin strips were cryosectioned at 5 µm thickness and skin sections containing anagen VI hair follicles were mounted onto MirrIR low 'e' microscope slides (Kevley, Ohio, USA), which are coated with a silver reflective coating. A final coating of tin oxide minimizes silver oxidation. The sections were fixed with 4% paraformaldehyde (PFA) in phosphate buffered saline (PBS) at room temperature for 20 minutes and washed 3 times with fresh reagent to remove the embedding compound and thus minimise spectral contamination.

3.3.3 Sample selection

FTIR measurements were performed on sections of hair follicle of which the shape and completeness were satisfactory. Three data sets (each data set acquired from a different

section; Table 1) are presented in this paper, with data set 1 presented in the main text in details, and the rest shown in the supplementary section. Data set 1 was acquired from a hair follicle from Patient A, while data sets 2-3 were from Patient B. Data sets 2 and 3 were acquired from different sections of the same hair follicle (approximately 10 μm apart).

3.3.4 FTIR measurement

The FTIR measurements were performed on a PerkinElmer FTIR 2000 instrument in trans/reflection mode. Using Penge30 software, a visible microscopy image was obtained to enable the specification of map area. A map region was established around the hair bulb (Fig.1) of a 5 μm thick skin section, since we were particularly interested in the mesenchyme of the hair follicle. The interferograms were collected at a spectral resolution of 8 cm^{-1} . We applied an aperture size of 20x20 μm^2 and a step size of 15 μm for data set 1, 18 μm for data sets 2 and 3. During the map scan, 64 interferograms were co-added per spectrum, spanning the frequency range of 4000-700 cm^{-1} , and a background measurement was performed after every 5 spectra to minimize noise and water vapour signals.

3.3.5 Data Analysis

The spectra were processed and analysed using Matlab software (Mathworks, USA). The spectra in data set 1 displayed Mie scattering artefacts¹⁸, which severely affected the baseline in the region of 4000-2500 cm^{-1} ; consequently only the 1800-1000 cm^{-1} region was used in the ensuing analysis. The spectra in all the data sets were smoothed (13 points) and linear baseline correct-ed. The spectra in data set 2 had further undergone offset normalisation over 1800-1300 cm^{-1} . Three regions in the map were omitted to remove artefacts from the evaluation (see blackened areas in Fig.1B) where perturbation due to liquid nitrogen refill was evident. N-FINDR, a spectral unmixing method similar to vortex component analysis (VCA)¹⁹ and iterated constrained endmembers algorithm²⁰, was applied to the pre-processed data to extract five endmembers¹¹.

The algorithm assumes that “pure” spectra are present in the dataset and that they span the largest volume in the n-dimensional volume spanned by the spectral points of all the spectra present in the data set. Those assumed pure spectra are termed endmembers. In the imple-

mentation of N-FINDR a dimension reduction using principal component analysis (PCA)²¹ was applied to the data set before calculating the largest volume. In the dimension reduced data set the positions of the “pure” spectra were found and the so-called endmembers extracted from the non-dimensionally reduced dataset. It must be noted that a pure spectrum does not refer to a pure compound. Rather, it can refer to a mixture of compounds, which can be detected in the sample. Ideally in our studies, the pure spectra refer to different tissue compartments.

All other spectra in the data set are then described as linear combinations of the found end-member spectra. This is achieved by a least squares fit with a non-negativity constraint of the endmembers to each spectrum in the data set. Each spectrum is then assigned an abundance value for each endmember that can be plotted in abundance maps. High abundances for one endmember in a spectrum indicate highly similar spectral features to the endmember and its spectrum. Overlapping of the components in the image map indicates a constitution of different spectral components in the spectra.

An evaluation was conducted to ensure the optimal number of endmembers was chosen. This was performed through PCA, which served to clarify the number of endmembers required to explain >99.95 % of the spectral variance of the entire data set. For instance, the PCA on data set 1 indicated that ≥ 4 principal components (PCs) are required to explain >99.95% of the data. Therefore, when N-FINDR was implemented, at least 4 endmembers would be required for data set 1. To further determine the correct number of endmembers, the output data matrices were examined, so that there should only be one spectrum in each matrix that is 100% of an endmember. This is because an endmember is a pure spectrum that spans the largest volume in the data set, so there should only be one identical spectrum in the output data. Furthermore, the baseline corrected IR spectra (input spectra) were compared with the linear combination of the endmember spectra (output spectra) at the same point, so that the input and the output should vary minimally.

3.4 Results

3.4.1 Data set 1

3.4.1.1 Overall morphology and protein distribution according to IR spectra

The FTIR map scanned hair bulb is as shown in the visible image in Fig. 1A with a red box indicating the mapped area. The hair bulb map scanned area, to trained eyes, clearly contains the tissue layers DP which is in the centre, matrix cells surrounding the DP which belong to the epithelium, CTS which wraps around the hair follicle, separating the hair follicle from its surrounding adipose tissue, with the outermost cuticle of the CTS intercalating with the subcutis (SC). According to the chemical map plotted based on the integrated intensity of the band at 1648 cm^{-1} (Fig. 1B), which is assigned to amide I, protein is the most abundant in the centre where its locality corresponds to the DP. A decrease in the intensity of amide I can be seen, from the centre outwards.

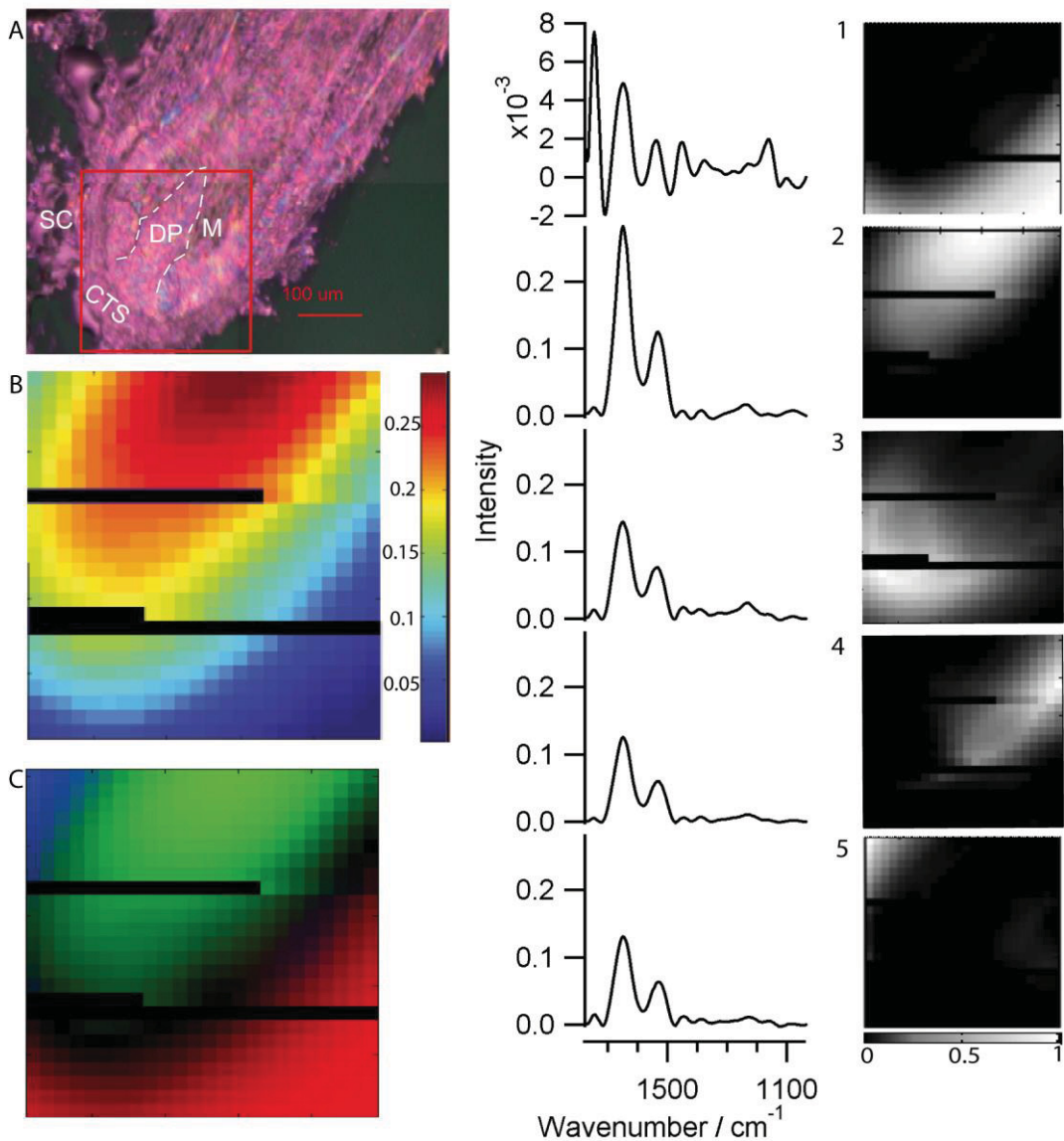


Figure 1 presented images of the hair follicle in data set 1. A) White light microscopy image of an anagen VI human hair follicle in an unstained skin section, mounted on a Kevley low 'e' slide. The purple hue comes from the reflection of the thin silver coating. The red box indicates the area of the hair bulb mapped by FTIR. Scale bar: 100 μm . The tissue layers can be distinguished by eyes: subcutie (SC), dermal papilla (DP; demarcated by the dotted white line), connective tissue sheath (CTS), and hair follicle matrix cells (M) belonging to the epithelium. B) Chemical image based on the integrated intensity of the band at 1648 cm^{-1} (amide I). The pure spectra of endmembers 1 to 5 are shown in the middle column, and the abundance maps of the endmembers shown in the right column. C) Overlapped abundance maps of endmembers 1, 2 and 5. Further elaborated in Fig. 3 caption.

3.4.1.2 Specific FTIR spectra correspond to distinct hair follicle compartments as shown in data set 1

Five endmembers were determined for data set 1. Assignments of the IR absorption bands, from which the chemical information can be interpreted, are listed (Table 1).

Table 1: Detected peak positions and the vibrational groups they correspond to.

Wavenumber value (cm ⁻¹)					Vibrational group (s)	Refs
Endmember						
1	2	3	4	5		
1744	1744	1744	1744	1744	carbonyl ester ν(C=O) (lipid)	22, 23
1648	1648	1648	1648	1648	Amide I ν(C=O) + ν(C-N) + δ(N-R ₂) (protein)	4, 24, 25
1540	1532	1536	1532	1532	Amide II δ(N-R ₂) + ν(C-N) (protein)	4, 25
1452	1452	1448	1448	1448	CH ₂ and CH ₃ deformation vibrations due to lipid contribution	4, 25
1376	1388	1388	1388	1384	Methyl	25
1284, 1236	1284, 1240, 1204	1280, 1232, 1204	1232	1276, 1228, 1204	Amide III C-N stretching, δ(N- R ₂) and C-C stretching (*collagen where triplet is present)	4, 25
	*	*		*		
1156	1164	1160	1160	1160	C-OH in proteins C-O in carbohydrates	26
-	1084	1080	1080	1084	Phosphodiester _{sym} PO ₂ ⁻ stretching	26, 27

Endmember 1 has local abundances situated at the periphery of the hair bulb and has a low overall IR absorbance indicating the tissue is thin and porous where endmember 1 is pre-

sent. The C=O band peaked at 1744 cm^{-1} assigned to the ester carbonyl group of fatty acids (FAs) is very high relative to the absorbance displayed in the other endmembers, showing lipid as a major component in the periphery. Because there is also presence of proteins, indicated by the amide I and II bands, and amide III at 1236 and 1284 cm^{-1} , endmember 1 is likely to represent the spectra collected from the SC around the hair follicle, with some of the outer cuticle of CTS included.

Endmember 2 has local abundances in the upper centre of the map (Fig.1), correlating to the location of DP. Its major bands peaked at 1644 and 1528 cm^{-1} (amide I and II) show high absorbance values compared to the amide I and II signals of the other endmembers (Fig.1). The strong presence of amide I being the centre of the hair follicle is consistent with the chemical image based on the integrated intensity of amide I (Fig.1B). The amide I band is a combination of three modes including $\nu(\text{C=O}) + \nu(\text{C-N}) + \delta(\text{NH}_2)$, while the amide II band which peaks at 1532 cm^{-1} is primarily composed of two modes $\nu(\text{C-N}) + \delta(\text{NH}_2)$, with a shoulder at 1516 cm^{-1} , as has been verified using the second derivative data of the spectrum.

In the second derivative data, the amide I displays minima at 1644 and 1580 cm^{-1} (Fig.2). The amide I band ($1716\text{-}1576\text{ cm}^{-1}$) constitutes three component bands; the amide II band ($1528\text{-}1468\text{ cm}^{-1}$) constitutes a peak at 1532 cm^{-1} with a shoulder at 1516 cm^{-1} . These features indicate strong presence of β -sheet secondary structure protein, correlating with known intense immunostaining for anti-fibronectin found in the DP in an anagen follicle^{29, 30}. Fibronectin is predominantly of β -sheet secondary structure at room temperature^{26, 32}.

The endmember exhibits a broad relative intense feature with a maximum at 1240 cm^{-1} , suggesting collagen and phosphate groups from nucleic acid remnants⁸ are both present and the breadth of the peak is due to their overlapping in the spectrum⁷. Hence, endmember 2 is likely to represent spectra from the DP cells.

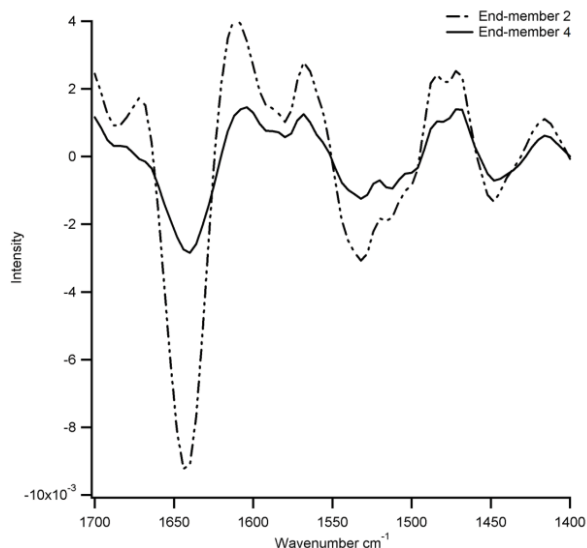


Figure 2. The second derivative of endmembers 2 (DP) and 4 (M) spectra within the amide I and II region ($1700\text{-}1400\text{ cm}^{-1}$) are displayed. In endmember 4, a peak at 1512 cm^{-1} within the amide II band is observed. In endmember 2, it is more of a shoulder (at 1512 cm^{-1}). A triplet is clearly identified in the amide I band for endmember 2, with minima at 1688 , 1644 and 1580 cm^{-1} , suggesting presence of α -helix as well as β -sheet secondary structure proteins.

Position-wise, endmember 3 (Fig.1) being situated between endmembers 1 (SC) and 2 (DP), is distinctive of CTS. This is supported by the strong presence of amide I and II (1648 and 1536 cm^{-1}) and the so-called collagen triplet between $1200\text{-}1300\text{ cm}^{-1}$ indicative of its connective tissue nature, less intense C=O band at 1744 cm^{-1} indicates lower level of lipids and further suggests endmember 3 represents the part of the CTS proximal to the DP. Endmember 3 likely represents CTS proximal to the DP.

Endmember 4 is characterised by its high amide I (1648 cm^{-1}) absorbance to carbonyl ester (1736 cm^{-1}) absorbance ratio, which indicates that proteins are the main component in this endmember. In the second derivative, its peak within the amide II band at 1512 cm^{-1} (Fig.2) can be attributed to intracellular keratins, of which presence is known in the hair follicle epithelium^{31,32}. Therefore, endmember 4 is likely to represent the hair follicle matrix cells (M) of the epithelium.

Endmember 5 has high abundances in the periphery of the mapped area and shows a relatively high amount of lipid, as indicated by the strong band at 1744 cm^{-1} , assigned to ester

carbonyl mode of lipids^{23,24}. It also naturally has a large amount of protein, as evinced by the intensity of the bands at 1648 and 1532 cm^{-1} ^{5,25,26}. The peaks at 1276, 1228 and 1204 cm^{-1} are typically present in collagen^{27,29}. The weak profile of the collagen triplet between 1300-1200 cm^{-1} in endmember 5 suggests that collagen is not a major protein component. Endmember 5 comprises of lipids, proteins, carbohydrate (1156 cm^{-1}) and collagen, and lies in the left periphery of the mapped area, strongly suggesting that endmember 5 represents CTS connected to the SC. The major difference between endmembers 1 and 5 lies in the proportion of proteins in the endmember and the overall IR absorbance.

3.4.1.3 N-FINDR abundance maps in relation to hair follicular anatomy

By assigning a colour to each endmember and showing their abundance distribution, a spatial presentation of endmembers was achieved (Fig.2). The presentation of the abundance of endmembers 1 (SC), 2 (DP) and 5 (CTS) in Fig.3A shows no overlapping between endmembers 1 (SC) with some outer CTS cuticle, and endmember 2 (pure DP). A small degree of overlapping between endmembers 2 (DP) and 5 (CTS) exists, and does also between endmembers 1 (SC) and 3 (CTS) (Fig.3B). The distribution of endmembers 3 (CTS) and 4 (epithelium) can also be seen in Fig.3B. The brownish pixels correspond to overlapped endmembers. By displaying the abundance maps of endmembers 2 (DP), 3 (CTS) and 4 (M), it can be clearly seen that endmember 4 (epithelium) is located in between (Fig.3B). The spatial information of the endmembers relates to one another in such a way that they resemble the positions the tissue layers are found in the mapped hair bulb (Fig 1A).

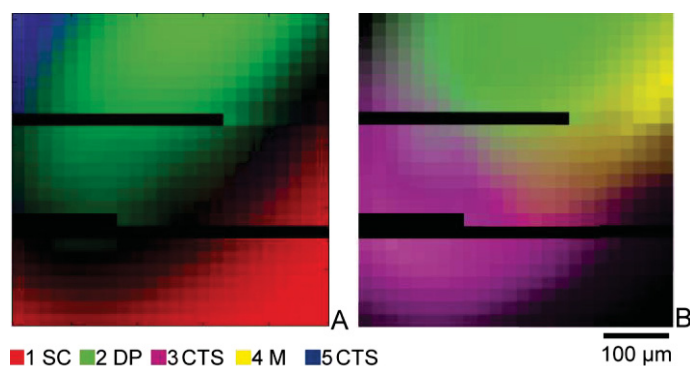


Figure 3. A) The abundance maps of endmembers 1 (red; SC), 2 (green; DP) and 5 (blue; CTS) are displayed on one map (same as Fig.1C). The overlapping areas between blue and green indicate pixels with characteristics of both endmembers 2 (DP) and 5 (CTS) in their spectra. Overlapping is found neither between endmembers 1 (SC) and 2 (DP), nor 1 (SC) and 5 (CTS). 3B: The abundance maps of endmember 2 (green; DP), 3 (lilac; CTS) and 4 (yellow; M) are plotted on the same map. Slight overlapping can be found between endmembers 2 and 3, as well as 2 and 4. SC= subcutis; DP= dermal papilla; CTS= connective tissue sheath; M= hair follicle matrix cells.

3.4.2 Data set 2

To verify that the excellent N-FINDR spectral unmixing results and correlation to visible images can be reproduced in other hair follicles and from more than one patient, FTIR mapping and N-FINDR were applied to two other data sets from a second patient. The mapped area for data set 2 extends further up the hair follicle distally than in data set 1 and contains hair follicle matrix cells (Fig. 4A). Two centres with high amide I abundance can be discerned in the chemical image plotted based on the integrated intensity of the amide I band (Fig. 4B). One high amide I intensity centre correlates to the site of hair follicle matrix cells; and a less intense centre correlates to the location of the DP.

Similar to data set 1, the resulting endmembers are found correlating to different hair follicular compartments (Fig. 4). Four endmembers were deemed adequate for this data set, as determined by method described in '3.5 Data analysis'. The chemical and structural information which supports the anatomical assignment of each endmember can be found in Tables 2 and 3.

Different colours to the endmembers: endmember 1 (DP) – green; endmember 3 (CTS, high lipids) – red; endmember 4 (CTS) – blue. Overlapping the abundance maps clearly shows

that the positions of endmembers highly correlate to their assigned follicular compartments (Fig.4C).

Table 2: Occupied positions and chemical information of the endmembers in data set 2.

End-member	Anatomical correlation	Occupied area in the FTIR map	Chemical information
1	DP	Centre	High amide I and amide II intensity (1644 and 1536 cm^{-1}) and absence of (C=O) intensity from lipid esters. The phosphates band also appears to overlap with the collagen triplet (1200-1300 cm^{-1} , centred at 1240 cm^{-1})
2	Hair follicle matrix cells	Upper region of the map, with an intense centre corresponding to where amide I intensity is the highest (Fig. 4B).	Higher amide I and II intensity (1644, 1536 cm^{-1}) than endmember 1. High protein to lipid ratio
3	CTS connected to the surrounding lipids	Correlates to the CTS in the visible image and the chemical image (Fig.4A,B)	Higher carbonyl ester (1744 cm^{-1}) / amide I (1648 cm^{-1}) ratio, indicating a high level of lipids. Evident collagen triplet at 1288, 1244 and 1208 cm^{-1} .
4	CTS with little contact with the SC	Correlates to the CTS in the visible image and the chemical image (Fig.4A,B)	A low intensity carbonyl ester peak at 1740 cm^{-1} suggests a low concentration of lipid contents.

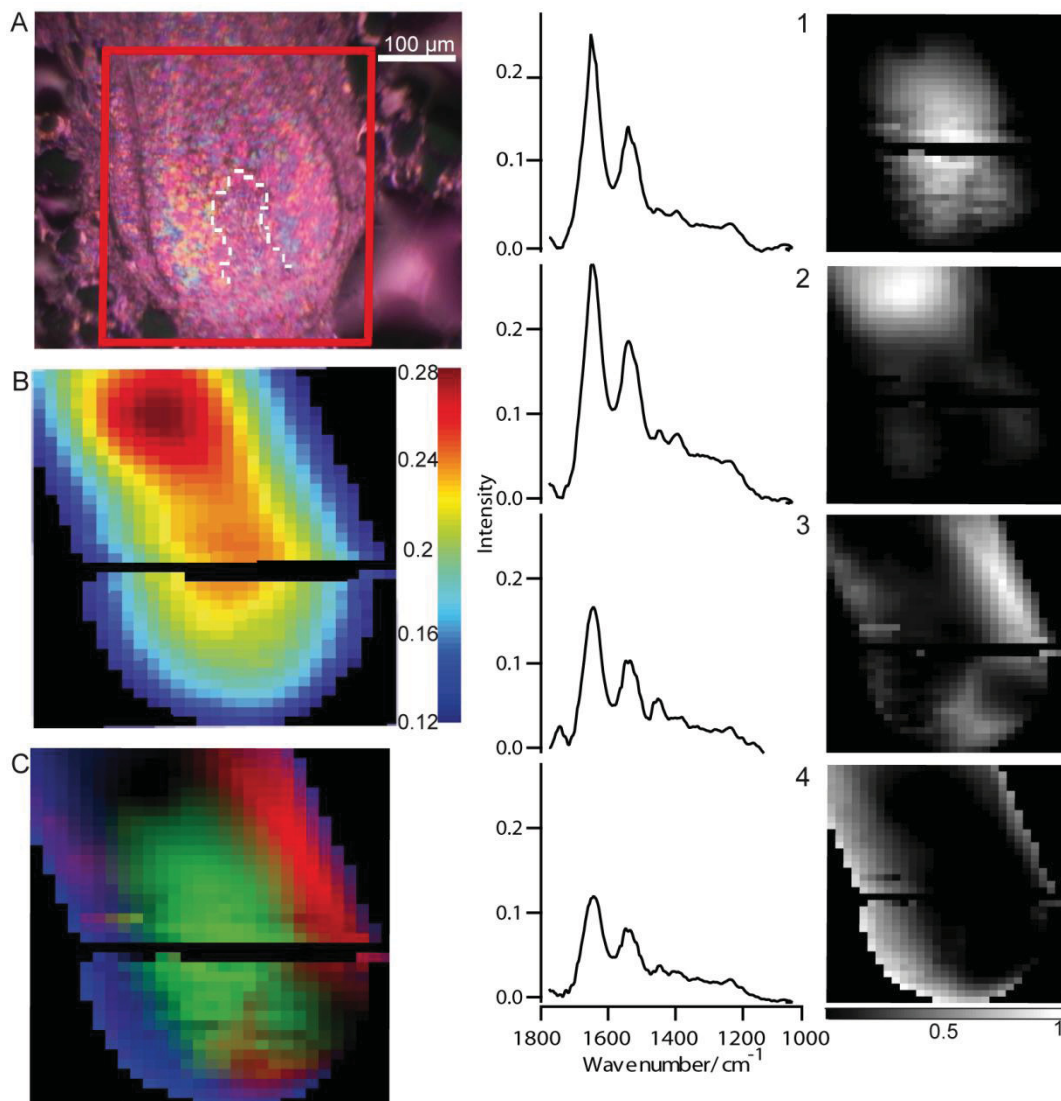


Figure 4A) The mapped area of the hair follicle in data set 2 is shown by the visible image. The white dotted line outlines the approximate area of the DP. This mapped area extends further up the hair follicle distally than data set 1, and contains hair follicle matrix cells. B) Chemical image based on the integrated intensity of amide I is shown. Blackened areas indicate pixels removed due to artefacts and low absorbance. C) Abundance map shows a combination of endmembers 1 (DP; green), 3 and 4 (CTS; red and blue). Mid column: the spectra of the endmembers are presented. The abundance maps are presented in the right column. Endmember 1 - DP; endmember 2 - hair follicle matrix cells; endmember 3 - CTS with high lipid and collagen contents; endmember 4 - CTS (with low overall intensity signifying thin tissue thickness), lower lipid levels than endmember 3. The grey scale bar below the abundance maps indicates the percentage of composition of the endmember in the pixels.

3.4.3 Data set 3

The hair follicle in data set 3 also came from the same hair follicle as in data set 2, but is from a skin section 10 μm away. This mapped area contains the lower half of the hair bulb (Fig.5A) with the DP occupying the largest area in the map. As DP contains a high level of proteins, the chemical image based on the amide I integrated intensity confirms the proteins presence (Fig.5B). Three endmembers were deemed adequate in this data set (Table 3).

Table 3: Occupied positions and chemical information of the endmembers in data set 3.

End-member	Anatomical correlation	Occupied area in the FTIR map	Chemical information
1	Hair follicle matrix cells	Correlates to epithelium surrounding the DP (Fig. 5A)	High protein to lipid ratio: although a small peak is present at 1744 cm^{-1} (C=O), the amide I intensity at 1644 cm^{-1} is very high.
2	CTS connected with SC	Periphery of the map, correlates to the position of the CTS (Fig. 5A).	High level of lipids presence (C=O, 1744 cm^{-1} ; CH_2 , CH_3 deformation, 1448 cm^{-1}). Ample amount of proteins (amide I and II, 1648 and 1536 cm^{-1}) and collagen (1284 and 1240 cm^{-1}).
3	DP	Most of the map area, with the highest percentage of expression in the upper centre.	High protein (1548 , 1536 cm^{-1}) and low lipid contents (absence of C=O at 1744 cm^{-1})

By assigning colours red to endmember 1 (M), blue to endmember 2 (CTS and SC) and green to endmember 3 (DP), and overlapping their abundance maps, the positions of the endmembers (Fig.5C) are clearly seen to correlate to the anatomical parts assigned.

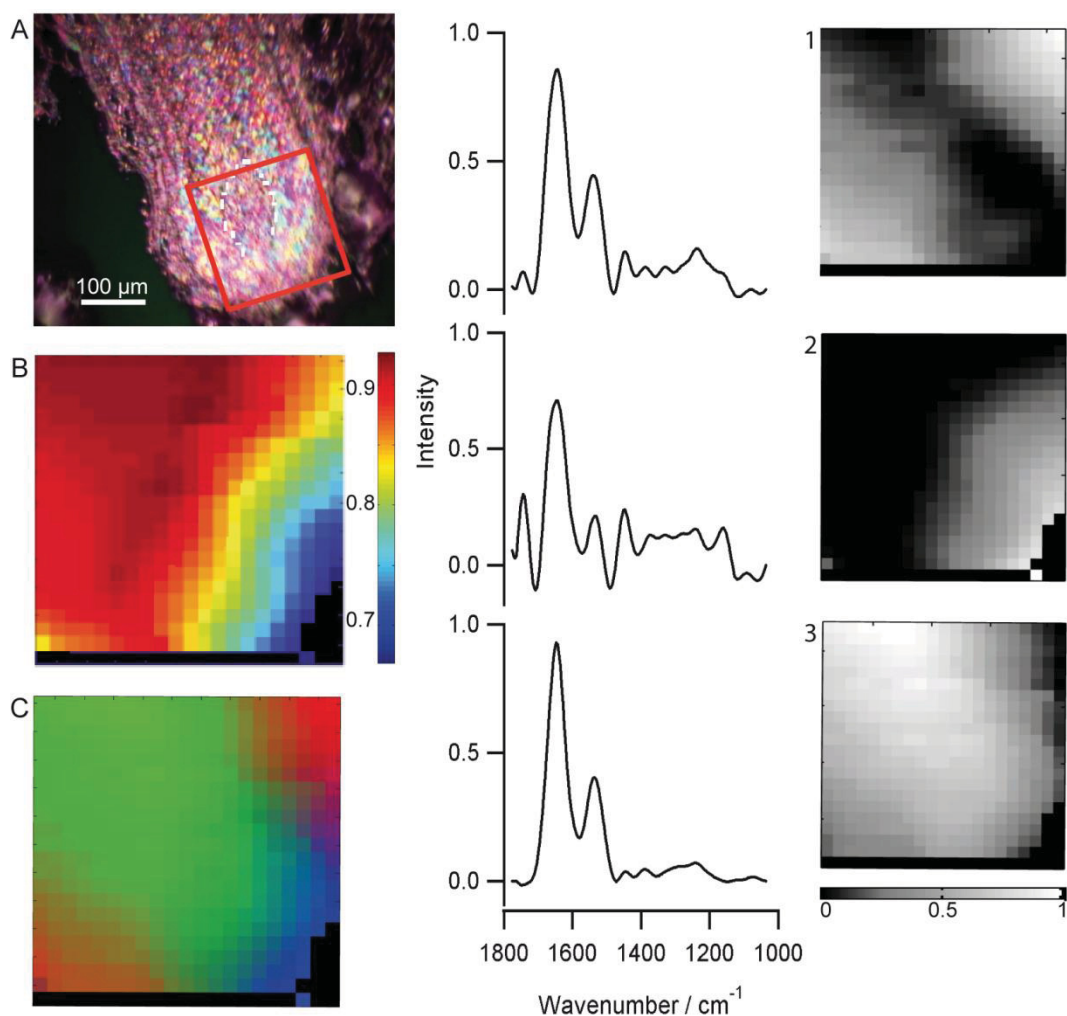


Figure 5 A) The mapped area of the hair follicle is shown by the visible image. The white dotted line outlines the membrane zone between the DP and the epithelium. This mapped area contains the lower half of the hair bulb. B) Chemical image based on the integrated intensity of amide I is shown. The areas in black are where artefacts and spectra with low absorbance had been removed from the analysis. The spectra of each endmember are presented in the middle and the abundance maps are presented in the right column. The grey scale bar below the abundance maps indicates the percentage of composition of the endmember in the pixels. C) The image displays a linear combination of endmembers 1, 2 and 3. Endmember 1 (red) correlates to the epithelium. Endmember 2 (blue) correlates to the CTS. Endmember 3 correlates to DP (high protein contents but low lipid and collagen contents).

3.5 Discussion

To enable the study of cells in the hair follicle in a label-free and minimally sample-destructive manner, a method that permits the observation and identification of cells within the hair follicle was developed and demonstrated by FTIR mapping and N-FINDR. Without labelling, the chemical information of each layer was evidently extracted from the end-

member spectra. The aperture size of 20 μm and interval of 15 μm provided a spatial resolution sufficiently small to differentiate between layers, yet large enough to produce good signal-to-noise ratios in the spectra. The parameters did not enable single cell lateral resolution, but as the aim of this work was to discern tissue compartments, higher resolution was in this case not sought.

3.5.1 Biological relevance of the N-FINDR results

The human anagen VI hair follicle is well extended into the SC and the hair follicle MSCs are known to differentiate into a number of lineages including adipocytes^{14, 33, 34}; PFA was thus chosen as a fixing agent to preserve the lipid features in our sample.

To avoid confusion, this discussion section will refer only to data set 1. The data presented in this chapter show that the centre of the follicle is lipid poor and protein rich (data set 1 endmember 2, Fig 2). Thus, our report is in line with a published study where FTIR spectroscopy imaging was applied on a skin tissue sample, in which a cross section of the hair follicle was captured¹⁷.

By using a combination of FTIR spectroscopy and N-FINDR spectral unmixing analysis, the CTS and the DP could be differentiated as they express different endmembers. The literature has shown that CTS and DP fibroblasts contain different properties and functions (Table 4). For instance, the expression of cell surface markers differs; the protein expression of CD10 *in vivo* by CTS and the absence of which in the DP and the surrounding interfollicular dermis^{35, 36}. Functionality-wise, the DP cells (but not the CTS cells) produce and release anagen inductive signals such as WNT and bone morphogenic protein signalling molecules^{37, 38}, and continue to stimulate hair growth by releasing signalling molecules such as insulin-like growth factor 1 and fibroblast growth factor 7 towards the matrix cells³⁹. The FTIR data are therefore consistent as N-FINDR clearly separated the DP and the CTS into distinct entities; and have shown the highest protein level was found in the DP among the tissue layers, consistent with its role of actively synthesising signalling molecules essentially composed of protein.

Table 4: The properties of DP cells, in comparison to CTS cells, are tabulated below.

Only found in DP cells	Found in both CTS and DP cells
<p><i>In utero</i> (originally present as a condensed body of mesenchymal cells) DP cells induce hair follicle placode development into hair germ during hair follicle formation in foetal. DP cells also perform this function in neonatal skin, as well as in adult (murine) repaired wounds⁴⁰.</p> <p>DP cells signal towards the hair follicle epithelium before a catagen (regression phase) to anagen (growth phase) transition is initiated^{39, 45}.</p>	<p>DP and trichogenic CTS cells <i>in vivo</i> have been shown to up-regulate alkaline phosphatase protein and smooth muscle actin expression⁴¹⁻⁴⁴.</p> <p>Cultured DP and CTS cells were both spontaneously aggregated and had similar morphology^{44, 46}.</p> <p>Both isolated DPs and CTS were shown to induce <i>de novo</i> folliculogenesis when implanted into sub-epidermal skin⁴⁷⁻⁴⁹.</p>

The CTS is composed of fibroblasts and a collagenous matrix characteristic of connective tissues. It functions as a tissue sheath surrounding the hair follicle and separates the follicle from its neighbouring SC. Due to the connection of the CTS outer cuticle to the adipose of the SC, the spectra obtained from the region (endmembers 1 and 5 in data set 1) reflected a high lipids level as expected. The MSCs in the CTS have already been shown to be able to differentiate into multi-lineages including adipocytes *in vitro*¹⁴. The increase in lipid contents towards the outer layers of the CTS as reflected by our spectra, supports a published hypothesis which suggested that the hair follicle mesenchyme was a source of pre-adipocytes that could be found distributed around the hair follicle, both during hair follicle development in foetal/neonatal animals, as well as in adults⁵⁰. It was deemed highly

conceivable that the pre-adipocytes contributing towards the perifollicular subcutaneous adipose tissue originate from the hair follicle mesenchyme and this phenomenon may well continue into adulthood⁵⁰; our data is clearly in agreement with this hypothesis.

According to the immunohistochemistry results in the literature, the DP should contain an ample amount of collagen in its extracellular matrix^{28, 29, 51-53}. The reason the collagen triplet in the endmember 2 of data set 1 is not as prominent as that in the endmember 4 of data set 1 (CTS) may be attributed to the presence of phosphate groups from nucleic acid remnants and lipids⁵, broadening what normally should appear as a triplet. Nevertheless, the peak is 1240 cm^{-1} centred, where the maxima of the collagen triplet lies²⁵, and is a clear indication of both collagen and nucleic acids presence, reflecting the high level of transcription. The high level of transcription is in line with the knowledge of DP being an active signalling centre^{39, 45}.

3.5.2 Suitability of using N-FINDR on hair follicle spectra

The N-FINDR abundance maps exhibit a transition of characteristics between different endmembers in the hair bulb. Due to the aperture size and the step size, it is inevitable that some spectra consist of absorbance from cells in adjacent layers. Although this could be thought of as an instrumental limitation since reducing the aperture size would also decrease the IR light reaching the sample, resulting in a lower signal-to-noise ratio, the results also reflect the transitional nature of tissue layers. For instance, where both DP and CTS overlap (Fig.3B), it is clear that the contributions of either endmember are low, indicating this transitional zone is the inter-DP/CTS boundary. While DP and CTS fibroblasts are distinguishable from each other, they are also inter-exchangeable^{54, 55} and CTS is capable of regenerating a DP^{56, 57}; thus some fibroblasts may display both DP and CTS characters.

Transitioning between endmembers 3 and 5 in data set 1 is as predicted, as the CTS gradually becomes more cuticle-like and interlaces with the surrounding SC. For the mixing of data set 1 endmember 4 (epithelium) with endmembers 2 and 3 (DP and mesenchyme), although distinct boundaries between epithelial and mesenchymal layers can usually be drawn, mesenchymal cells have been reported to interact with the follicular epithelial cells²⁸. Such interaction is mediated via direct cell contact through a punctuated

basement membrane, and by extending cytoplasmic processes of mesenchymal cells into the epithelial layer²⁸. Moreover, CTS cells are known to penetrate the glassy membrane between the ORS of the epithelium and the CTS to initiate cell contact with the epithelial cells at the beginning of anagen²⁸.

While endmember extraction methods effectively show where spectra display mixed spectral characteristics and to what extent, analytical tools such as unsupervised hierarchical clustering analysis and K-means clustering are also powerful^{5, 58}. However, since these clustering methods result in hard borders, and our spectra were recorded using aperture larger than an average cell size, N-FINDR was chosen for a more realistic interpretation.

By applying N-FINDR to data sets acquired from different hair follicles from two patients, as well as two sections from the same hair follicle, the reproducibility of N-FINDR is evidently demonstrated. Due to the different shapes and orientation of the hair follicles within the skin, no two hair follicles look the same. The abundance maps of the endmembers in different data sets are thus not identical. Nevertheless, the major tissue layers were discernible by the FTIR spectral analysis, and the endmember abundance maps were comparable to the anatomy of the hair follicles the FTIR data were collected from.

3.5.3 Perspectives for the use of FTIR microspectroscopy in the hair biology field

Having proven the employability of FTIR microspectroscopy to distinguishing tissue types, the next immediate aim is to identify and characterise single cells, based on their molecular fingerprints, by improving the spatial resolution. This will be realised by the help of focal plane array (FPA)-, attenuated total reflection (ATR)- and Synchrotron (SR)-FTIR technologies, as well as Raman spectroscopy. Future work points towards the identification of hair follicle stem cells with FTIR spectroscopy and depicting their participation in dermal wound healing.

3.6 Conclusions

The main purpose of this study was to demonstrate the feasibility of applying FTIR spectroscopy and spectral unmixing algorithms to tell apart major tissue layers in the hair

follicle. Having proven this applicability, we are confident that increases in resolution will allow more minor details to be distinguished. The potentials of vibrational spectroscopy for examining molecular changes in the hair follicle have hereby been demonstrated and can be applied in the future to an array of studies. This 'top down' method is highly recommended for the application of vibrational spectroscopy to new type of tissues/organs so that an overall understanding of the sample can be obtained prior to elucidating more minute details.

FTIR microspectroscopy and multivariate analysis have been successfully applied to mapping human anagen VI hair follicle end bulbs. To the best of our knowledge, this report demonstrates for the first time the applicability of FTIR spectroscopy to discerning the follicular tissue layers, based on their spectral variation, which can be molecularly assigned. Thus, the molecular information of the individual tissue layers can be simultaneously extracted directly. By comparing the spectral features to the known biological characteristics, the assignment of the clusters to the tissue layers was confirmed. Though possible for visualising the tissue layers, unless the samples are stained, light microscopy alone can neither directly elucidate molecular information, nor provide a quantification of compounds. Fluorescence staining can provide information of the distribution and presence of a particular species, but the number of fluorescence labels applicable to a tissue sample is limited, since fluorescence exhibits broad bands in the electromagnetic spectrum and they overlap. Tagging a sample also leads to a sample becoming non-reusable for examinations with other assays. FTIR microspectroscopy, on the other hand, can be used as a minimally sample-destructive, non-labour intensive and semi-quantitative method to provide a full range of biochemical information quantitatively and qualitatively.

References

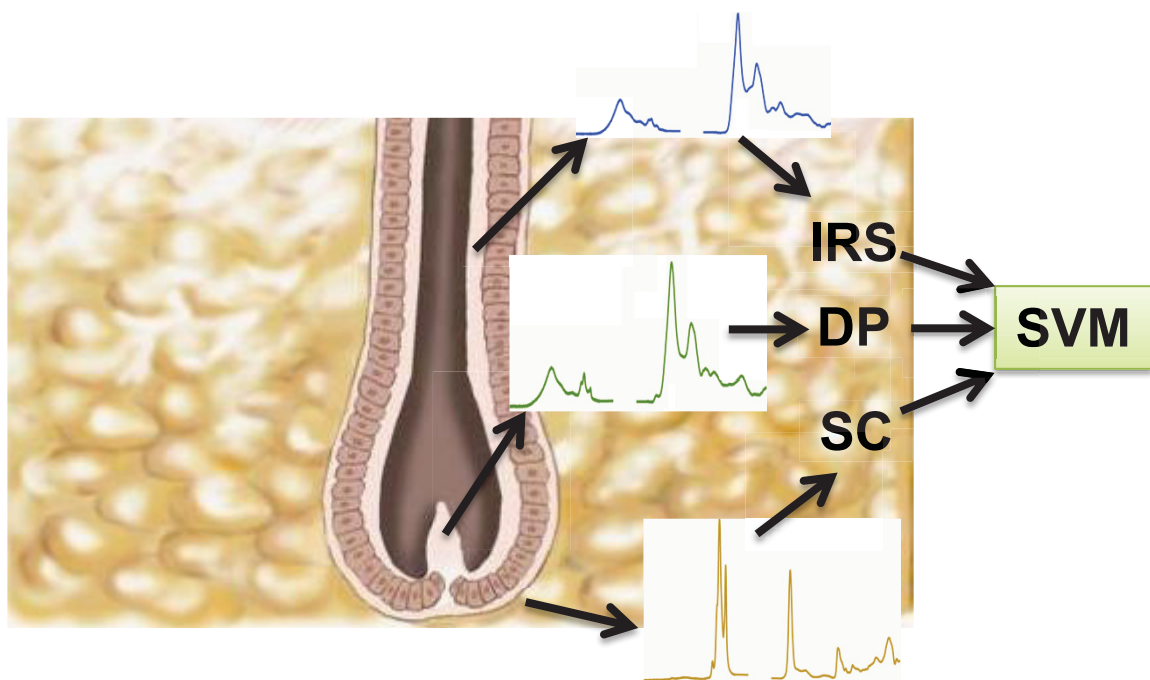
1. K. Lau, M.A.B. Hedegaard, J.E. Kloepper, R. Paus, B.R. Wood and V. Deckert, *J Dermatol Sci*, 2011, **63**, 191-198
2. M. Hedegaard, C. Krafft, H. J. Ditzel, L. E. Johansen, S. Hassing and J. Popp, *Anal Chem*, 2010, **82**, 2797-2802.
3. D. Ami, T. Neri, A. Natalello, P. Mereghetti, S. M. Doglia, M. Zanoni, M. Zuccotti, S. Garagna, and C.A. Redi, *BBA*, 2008, **1783**, 98-106.
4. J. Babrah, K. McCarthy, R. J. Lush, A. D. Rye, C. Bessant and N. Stone, *Analyst*, 2009, **134**, 763-768.
5. B. R. Wood, L. Chiriboga, H. Yee, M. A. Quinn, D. McNaughton and M. Diem, *Gynecol Oncol*, 2004, **93**, 59-68.

6. Z. Hammody, S. Argov, R. K. Sahu, E. Cagnano, R. Moreha and S. Mordechai, *Analyst*, 2008, **133**, 372–378.
7. M. J. Baker, E. Gazi, M. D. Brown, J. H. Shanks, N. W. Clarke and P. Gardner, *J Biophotonics*, 2009, **2**, 104-113.
8. M. J. Walsh, T. G. Fellous, A. Hammiche, W.-R. Lin, N. J. Fullwood, O. Grude, F. Bahrami, J. M. Nicholson, M. Cotte, J. Susini, H. M. Pollock, M. Brittan, P. L. Martin-Hirsch, M. R. Alison and F. L. Martin, *Stem Cells*, 2008, **26**, 108-118.
9. M. J. Walsh, A. Hammiche, T. G. Fellous, J. M. Nicholson, M. Cotte, J. Susini, N. J. Fullwood, P. L. Martin-Hirsch, M. R. Alison and F. L. Martin, *Stem Cell Res*, 2009, **3**, 15-27.
10. C. Krafft, R. Salzer, S. Seitz, C. Ern and M. Schieker, *Analyst*, 2007, **132**, 647-653.
11. M. E. Winter, *Proc. SPIE*, 2004, **5425**, 31-41.
12. C. A. B. Jahoda and A. J. Reynolds, *Lancet*, 2001, **358**, 1445-1448.
13. A. Gharzi, A. J. Reynolds and C. A. B. Jahoda, *Exp Dermatol*, 2003, **12**, 126-136.
14. C. A. B. Jahoda, C. J. Whitehouse, A. J. Reynolds and N. Hole, in *Exp Dermatol*, 2003, **12**, 849-859.
15. G. Richardson, E. Arnott, C. Whitehouse, C. Lawrence, A. Reynolds, N. Hole and C.A.B. Jahoda, *J Invest Dermatol Symp Proc*, 2005, **10**, 180-183.
16. K. Lau, R. Paus, S. Tiede, P. Day and A. Bayat, *Exp Dermatol*, 2009, **18**, 921-933.
17. R. Mendelsohn, H.-C. Chen, M. E. Rerek and D. J. Moore, *J Biomed Opt*, 2003, **8**, 185–190.
18. P. Bassan, H. J. Byrne, F. Bonnier, J. Lee, P. Dumas and P. Gardner, *Analyst*, 2009, **134**, 1586-1593.
19. J. M. P. Nascimento and J. M. B. Dias, in *Pattern Recognition and Image Analysis*, Springer, Berlin/Heidelberg, 2003, vol. 2652, pp. 626-635.
20. M. Berman, A. Phatak, R. Lagerstrom and B. R. Wood, *J Chemometr*, 2009, **23**, 101-116.
21. S. Wold, *Pattern Recogn.*, 1976, **8**, 127–139.
22. O. Pillai and R. Panchagnula, *Skin Pharmacol Physiol* 2004, **17**, 289-297
23. Y.-Z. Li, Y.-S. Quan, L. Zang, M.-n. Jin, F. Kamiyama, H. Katsumi, A. Yamamoto and S. Tsutsumi, *Biol. Pharm. Bull.* , 2008, **31**, 1574-1579.
24. E. Pauthe, J. Pelta, S. Patel, D. Lairez and F. Goubard, *BBA* 2002, **1597**, 12-21.
25. K. Potter, L. Kidder, I. Levin, E. Lewis and R. Spencer, *Arthritis Rheum*, 2001, **44**, 846–855.
26. P. T. T. Wong, R. K. Wong, T. A. Caputo, T. A. Godwin and B. Rigas, *PNAS*, 1991, **88**, 10988-10992.
27. A. Kohler, D. Bertrand, H. Martens, K. Hannesson, C. Kirschner and R. Ofstad, *Anal Bioanal Chem*, 2007, **389**, 1143-1153.
28. C. A. Jahoda, A. Mauger, S. Bard and P. Sengel, *J. Anat.*, 1992, **181**, 47-60.
29. J. Couchman and W. Gibson, *Dev Biol*, 1985, **108**, 290-298.
30. V. Brumfeld and M. M. Werber, *Arch Biochem Biophys*, 1993, **302**, 134-143.
31. H. Heid, I. Moll and W. Franke, *Differentiation*, 1988, **137**, 137-157.
32. P. A. Coulombe, R. Kopan and E. Fuchs, *J. Cell Biol.*, 1989, **109**, 2295-2312.
33. E. V. Kiseleva, E. S. Chermnykh, E. A. Vorotelyak, A. I. Volozhin, A. V. Vasiliev and V. V. Terskikh, *Cell Tissues Biol*, 2009, **3**, 42-49.
34. M. J. Hoogduijn, E. Gorjup and P. G. Genever, *Stem Cells Dev*, 2006, **15**, 49-60.
35. E. Poblet and J. Jiminez, *Br J Dermatol*, 2008, **159**, 646-652.
36. K. Lee, Y. Choi, W. Kim, J. Lee, J. Yang, E. Lee, D. Lee and K. Jang, *Br J Dermatol*, 2006, **155**, 841-865.
37. C. Blanpain and E. Fuchs, *Nat Rev Mol Cell Biol*, 2009, **10**, 207-217.
38. M. Rendl, L. Polak and E. Fuchs, *Genes Dev.*, 2008, **22**, 543-557.
39. R. Paus and G. Cotsarelis, *N Engl J Med*, 1999, **341**, 491-497.
40. M. Ito, Z. Yang, T. Andl, C. Cui, N. Kim, S. E. Millar and G. Cotsarelis, *Nature*, 2007, **447**, 316-321.

41. K. J. McElwee, S. Kissling, E. Wenzel, A. Huth and R. Hoffmann, *J Invest Dermatol*, 2003, **121**, 1267-1275.
42. B. K. Handjiski, S. Eichmuller, U. Hofmann, B. M. Czarnetzki and R. Paus, *Br. J. Dermatol.*, 1994, **131**, 303-310.
43. M. Iida, S. Ihara and T. Matsuzaki, *Dev Growth Differ*, 2007, **49**, 185-195.
44. C. A. B. Jahoda, Reynolds, A.J., Chaponnier, C., Forester, J.C., Gabbiani, G, *J. Cell Sci.*, 1991, **99**, 627-636
45. R. Paus and K. Foitzik, *Differentiation*, 2004, **72**, 489-511.
46. M. Ohyama, Y. Zheng, R. Paus and K. S. Stenn, *Exp. Dermatol.*, 2009, **19**, 89-99.
47. T. Matsuzaki and K. Yoshizato, *Wound Repair Regen.*, 1998 **6**, 524-530.
48. A. J. Reynolds, C. Lawrence, P. B. Cserhalmi-Friedman, A. M. Christiano and C. A. B. Jahoda, *Nature*, 1999, **402**, 33-34.
49. J. Qiao, A. Zawadzka, E. Philips, A. Turetsky, S. Batchelor, J. Peacock, S. Durrant, D. Garlick, P. Kemp and J. Teumer, *Regen Med*, 2009, **4**, 667-676.
50. K. Wojciechowicz, E. Markiewicz and C.A.B. Jahoda, *Exp. Dermatol.*, 2008, **17**, 675-680.
51. J. R. Couchman, *J Invest Dermatol*, 1986, **87**, 762-767.
52. S. Joubeh, O. Mori and T. Hashimoto, *Exp Dermatol*, 2003, **12**, 365-370.
53. A. Messenger, K. Elliott, A. Temple and V. Randall, *J Invest Dermatol*, 1991, **96**, 93-97.
54. D. Tobin, A. Gunin, M. Magerl, B. Handjiski and R. Paus, *J Invest Dermatol Symp Proc* 2003, **8**, 80-86.
55. W. Y. Chi, D. Enshell-Seijffers and B. A. Morgan, *J Invest Dermatol*, 2010, **130**, 2664-2666.
56. R. F. Oliver, *J. Embryol. Exp. Morph.*, 1966, **16**, 231-244.
57. K. A. Horne and C. A. B. Jahoda, *Development*, 1992, **116**, 563-571.
58. C. Krafft, G. Steiner, C. Beleites and R. Salzer, *J Biophotonics*, 2009, **2**, 13-28.

Chapter 4

A classifier built on single hair follicle FTIR spectra for demarcating hair follicular compartments based on spectral variations



4.1 Abstract

The application of Fourier transform infrared (FTIR) spectroscopy demarcated hair follicular compartments, demonstrating that tissue / cell types in the hair follicle can be distinguished based solely on spectral variations. To use vibrational spectroscopy to identify and sort hair follicle stem cells, a classifier that can recognise infrared (IR) spectral features of stem cells, and sort unknown IR spectra into their appropriate classes, is required. As a starting point, we investigated the identification capabilities of a classifier on follicular tissue compartments. This chapter presents a classifier, which has been developed to identify the hair follicle compartments based on the learned features in the FTIR spectra. The focus was placed on the hair bulb. The compartments that can be visualised in a hair bulb were assigned as classes. Using thirty single FTIR spectra collected within each compartment, a support vector machine (SVM; a classifier) was trained. The usability of this classifier was verified by constructing a false colour image by classifying each pixel in a map scan product into a class. The classifier successfully classified the unknown spectra into their appropriate classes. This study implies future use of FTIR spectroscopy on differentiating cell types within a tissue compartment.

4.2 Introduction

In Chapter 3, the applicability of FTIR spectroscopy and N-FINDR spectral unmixing algorithm to demarcating human hair follicular compartments was proven¹. To carry on developing a label-free and minimally-destructive method to recognise and sort spectra from different tissue / cell types, a classifier was developed. A SVM was trained to recognise and classify FTIR spectra from the human hair follicle bulbar region mathematically into their respective compartments.

FTIR has become a popular modality for analysing macromolecular changes in a variety of tissues, including skin². However, aside from the investigation of hair fibre³, the use of FTIR spectroscopy to map the hair follicle and investigate the chemical contents has so far only been carried out by us^{1,4,5}.

For now the classifier has been built only on the compartments in the hair bulb. By feeding single spectra collected from known compartments of the follicle to the SVM, and testing the

SVM (the classifier) with FTIR maps collected from hair bulbs, the feasibility and reproducibility to distinguish tissue layers based on the spectral variations were demonstrated.

The advantage of selecting the hair bulb in particular, is that the dermal papilla (DP) and the connective tissue sheath (CTS) are clearly visible and can act as a validation model in our final outcome – a pseudo colour map. The idea is that spectra can be reliably classified into their respective compartments, and the classification will enable the building of an image. The SVM building process and the verification results are presented in this chapter to demonstrate the feasibility of this method; the results also suggest a SVM can be trained to recognise cell types within a compartment. Future work based on this pilot study lays in the direction of visualising stem cells (e.g. hair follicle stem cells) in wound healing assays.

4.3 Materials and Method

4.3.1 Sample source

Human scalp skin was collected from face lift surgery patients, according to the Helsinki guidelines, as described in Chapter 3. Skin was snap frozen, cryosectioned at 8 μm and mounted on MirrIR low 'e' slides (Kevley, USA).

4.3.2 Preparation and measurement

A Varian 670 FTIR spectrometer (Varian, USA) coupled with a mercury cadmium telluride (MCT) detector was employed for FTIR measurement. An aperture size of about 20 μm was used and 64 co-add scans were collected per spectrum; each spectrum spanned from 3800-800 cm^{-1} . By placing the aperture over a particular part of the hair follicle (which can be distinguishable by eyes) and clearly within the compartment, single spectra were collected from human hair follicles in 8 μm thick human cryo skin sections mounted on MirrIR low 'e' slides (Kevley, USA). The tissue compartments in the hair bulb which can be identified by eyes are DP, CTS, hair follicle matrix cells (M) and outer root sheath (ORS). As well, at the particular growth phase these chosen hair follicles were in (anagen VI), the hair bulbs are surrounded by subcutis (SC). It is harder to differentiate the inner root sheath (IRS) towards the hair bulb and both M and IRS belong to the epithelium. Hence single IRS spectra were obtained further up the hair shaft distally where IRS and ORS can clearly be distinguished. The recording locations of the single spectra were therefore selected according to these six classes – DP, CTS, IRS, ORS, M and SC.

FTIR maps were collected in transflection mode using a commercial FTIR spectrometer (model 670, Varian, USA) and an FTIR microscope with a 64× 64 focal plane array (FPA) detector (model 620, Varian). By placing a tile over the hair bulb, 4096 FTIR spectra were collected simultaneously. The microscope was equipped with a Cassegrain 15× NA 0.4 objective. The microscope chamber was enclosed in a home-built box and purged by dry air to reduce spectral contributions from water vapour. Each image covers an area of 350 × 350 μm² with each pixel corresponding to an area of 5.5 × 5.5 μm², approximating a cell size. The resulting spectra were averaged from 64 co-add scans. Background spectra were taken from a blank area.

4.3.3 Chemometrics

The raw FTIR spectra were pre-processed by background removal using SNIP algorithm⁶, truncating the region between 2750 -1800 cm⁻¹. After that every spectrum \vec{s} was normalized by its L' norm, which means that

$$\tilde{s}_i = \frac{s_i}{\sum_{j=0}^N |s_{ij}|} \quad (1)$$

Principal component analysis (PCA)⁷ was then applied to the pre-processed spectra to rotate the data set to a more appropriate coordinate system without further scaling or centring the data. This data set rotation by PCA can be thought of as a way to find the most representative scores (wavenumbers) in the data set, hence identifying the most distinctive spectral features.

After the PCA procedure only the first 19 scores were used. In other words, only the 19 most significant scores as determined by the PCA would be taken into consideration when the classification took place. In this work, only SVMs⁸ were used, with the implementation of Chang and Lin⁹. All computation was done with Gnu R14 with the SVM routines from the e1071package¹⁰ which encoded libSVM⁹. All other procedures were written in-house.

4.4 Results and Discussion

The means spectra of the single spectra from the six different classes used to train the classifier are shown in Fig. 1. The FTIR band assignments are enlisted in Table 1. In all but the SC spectrum, the major components of the spectra are protein and peptides. Amide A, amide B, amide I and II were clearly detected. Collagen is clearly detected in CTS at 1280, 1238, 1203 cm⁻¹, whereas nucleic acids are detected in the DP and the M spectra as the band is broadened by the overlapping of the phosphate FTIR band (attributed to nucleic acids

remnants). In the SC spectrum, the spectrum is dominated by the bands attributed to saturated fatty acids (satFAs) and unsaturated fatty acids (unsatFAs), phospholipids and triglycerides (Table 1).

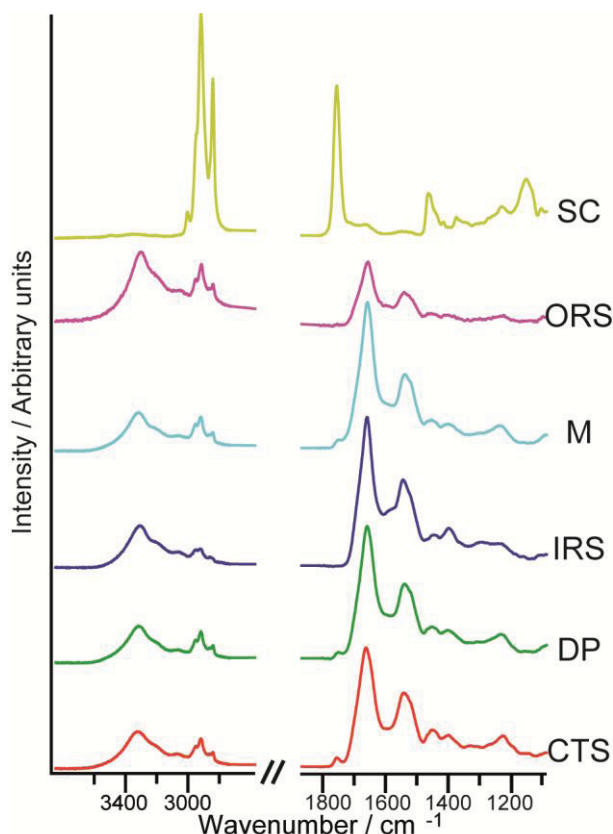


Figure 1: The mean preprocessed spectra of the training data for the six classes. The spectra have been offset without altering the scale.

In this work, a data set consisting of 6 classes, each with 30 spectra, was used for training. Since SVMs are binary classifiers, a method for building multiclass classifiers was needed. Thus, the one-against-one scheme was used, meaning that for every possible pair of classes one classifier was trained to distinguish between only this pair. The present data set consists of $6 \times 5/2 = 15$ binary classifiers. Thus, 15 one-against-one classifiers for the present data set were trained. Every spectrum is subsequently classified by a majority voting system, such that the class with the highest votes becomes assigned.

Table 1. The bands found in the means spectra of the single cell spectra, their modes and origins are enlisted below. Band assignments are according to literature refs¹¹⁻¹⁷

Wavenumber / cm^{-1}	Mode	Originated from
3305	Amide A (N-H stretching)	Protein/peptide
3064	Amide B / Amide II overtone	Protein/peptide
3010	C-H stretching of alkenes	Unsaturated fatty acid
2956/2954	Asymmetric stretching CH_3	Protein, aliphatic amino acid side chains
2926/2924	Asymmetric stretching CH_2	Phospholipid, glycolipid, FA
2873	Symmetric stretching CH_3	Protein, aliphatic amino acid side chains
2854	Symmetric stretching CH_2	Phospholipid, glycolipid, FA
1745	C=O stretching	Lipid, phospholipid
1656	Amide I (C=O stretching)	Protein/peptide
1539	Amide II (N-H bending, C-N stretching)	Protein/peptide
1463/1452, 1402	CH_2 , CH_3 scissoring	Phospholipid, glycolipid, FA, triglyceride, protein
1377	CH_3 symmetric bend	Phospholipid, fatty acid, triglyceride, protein
1238	Antisymmetric PO_2 stretch	Phosphate groups, nucleic acid
1280, 1238, 1203	Amide III (CN stretch, NH in plane bend, CC stretch)	Amide III, Collagen
1162	Ester C=O asymmetric stretching	Ester
1081	Symmetric PO_2 stretch	Phosphate salt, nucleic acid, DNA, RNA

ORS has the lowest overall absorbance due to its relatively porous nature. A broad band with maxima at around 3300 cm^{-1} is detected in all but the SC means spectrum, showing the dryness of the sample (as O-H from water absorbs at around 3400 cm^{-1}) and clarifying the contribution of Amide A to the said band. The CH bands peak at varied positions according to the classes. For instance, 2954, 2924, 1463 cm^{-1} for SC and 2956, 2926, 1452 cm^{-1} for CTS. The shifts may be related to the disordered phase of the fatty acid chains. While most of the interclass spectral variations can be observed in the means spectra, subtle changes between two classes can be derived from the SVM loadings, for examples DP minus CTS (Fig. 2). The loading plots can be scrutinised in a similar manner to difference spectra.

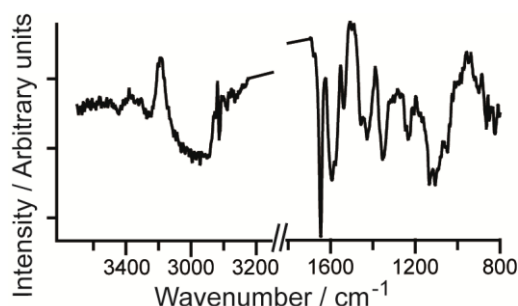


Figure 2 Loadings of the SVM between two classes, calculated by rotating back the data from the 19 dimensional PCA space to the original spectral space. The presented spectrum shows the discriminating vector between the classes DP and CTS.

A FTIR map of a hair bulb was used to verify the classifier. For the FTIR hair follicle data set the same pre-processing as the training set was adopted. After pre-processing the data set from the map was rotated into the coordinate system of the PCA mentioned above. After the rotation, again only the first 19 scores of the new data set were used for all further computations.

The result for the identification experiment is shown in Fig. 3, where every point of the map is identified independently and labelled by the one-against-one SVM. The classes are assigned different colours, thus, a false colour image is shown. The false colour image successfully correlated to the tissue layers that can be seen in the mapped hair bulb.

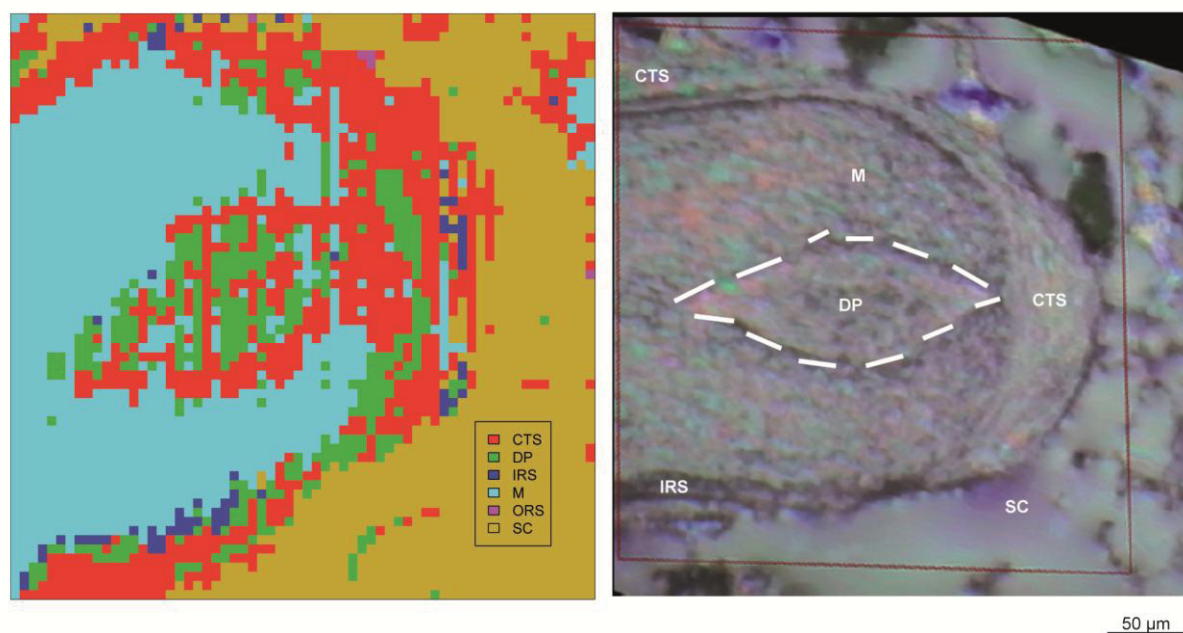


Figure 3 The FCM was obtained by classifying each of the spectra with the SVM using a one-against-one method. Each spectrum was assigned to one of the six possible classes. Each class was given a colour, as shown in the legend in the left image. The positions of the classes roughly correlate to the microscopy image of the mapped hair bulb. The shown hair bulb is a rough estimate for where it was mapped.

In the CTS layer (red), some DP cells (green) can be observed, according to the false colour map. Red CTS cells are also observed in the DP. Such inter-exchangeability between DP and CTS cells is a well-known feature in the hair follicle, and has been discussed in Chapter 3.

For an understanding of the level of confidence in the class assignment, images with the probabilities of assignment are plotted (Fig. 4). A black pixel is where there is 0% probability for this particular point to be assigned to the said class, whereas a white pixel is indicates a 100% probability for the class assignment. The images are displayed for each class in grey scale. As expected, the pattern of high level of expression for a particular class correlates to the where the compartment is expected in the hair follicle (Fig. 4).

In Fig. 4a and 4b, where probabilities of assignment per class are shown, it is clear that the pixels assigned to CTS are the brightest (highest probability) in the CTS layer and some less bright pixels in the central DP area. Whereas the brightest pixels in Fig. 4b (DP) are found in the DP.

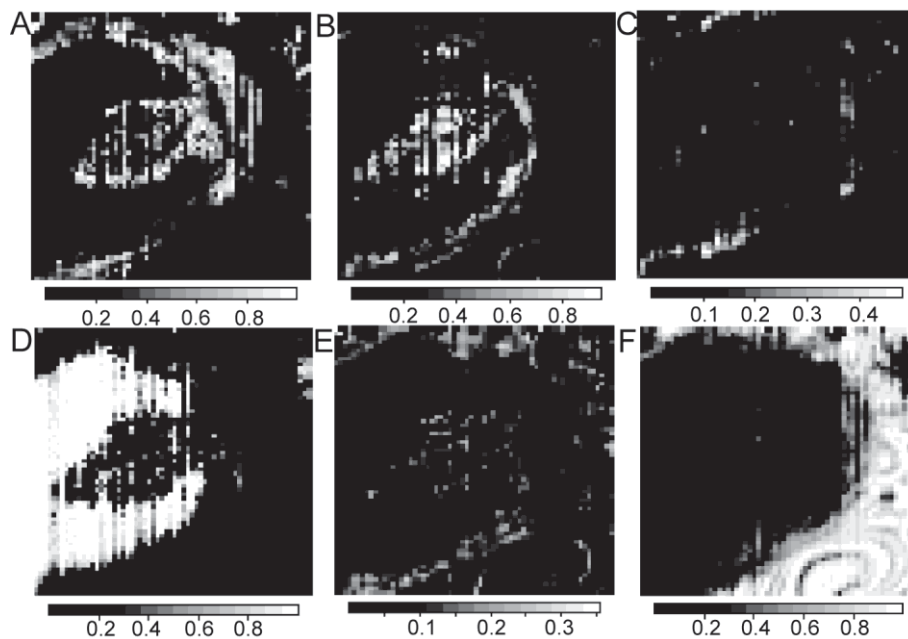


Figure 4 Images displaying the probabilities of assignment per class at every point of the map plotted in grey scale. A: CTS; B: DP; C: IRS; D: M; E: ORS; F: SC. A white point means that the classifier is 100% confident for the particular class assignment at that point. A black point means that the classifier is 0% confident for assigning the point to the particular class.

Artefacts can be seen in the false colour map – spectra that were classed as ORS were found outside the hair bulb (Fig.3). ORS was not seen in the mapped area and no spectra belonging to ORS were found within the hair bulb, clarifying its absence. The erroneous classification outside the hair bulb (adjacent to the CTS layer in red) was likely to be due to areas in the map originating from the porous parts of the skin, containing mainly noise in the spectra. The ORS spectrum displays the lowest overall absorbance (see Fig.1) and therefore explains why a spectrum consisting mainly of noise is misclassified as ORS.

4.5 Conclusion

A SVM has successfully been trained for six tissue compartments that can be found in a human hair follicle bulb. The SVM serves to classify unknown spectra recorded from the hair follicle bulb to their respective class (tissue compartment), and demonstrates the viability of distinguishing hair follicle cell types based on spectral variability. The usability of the classifier has been demonstrated using a FTIR map collected with FPA-FTIR. By assigning a colour to each class, and classifying the unknown spectra from the hair follicle FTIR map, a pseudo colour map with high degree of correlation to the visible image was successfully constructed.

Having demonstrated that different hair follicle cell types can be differentiated by spectral variability, we propose that this will also enable the identification of stem cells from non-stem cells in the hair follicle.

Training a SVM with stem and non-stem cells in the skin potentially enables the visualisation of the positions and movement of stem cells in wound healing studies without labelling. Furthermore, such cell identification methods pave ways for label-free cell sorting and the direct application of such purified and enriched stem cells to wound healing treatments.

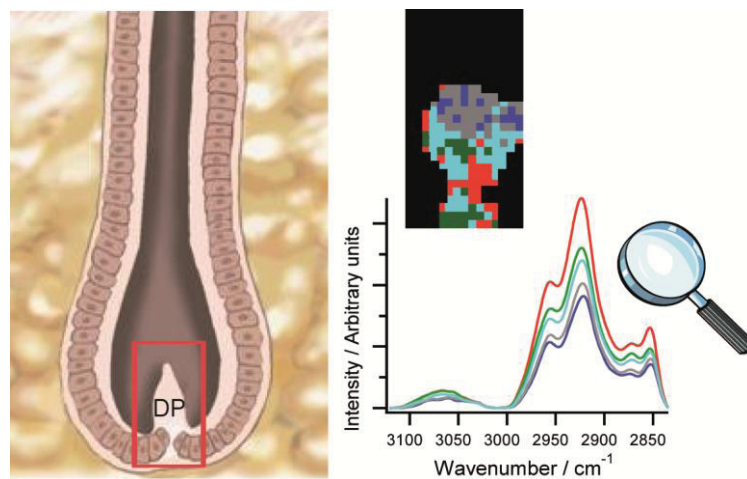
References:

1. K. Lau, M.A.B. Hedegaard, J.E. Kloepper, R. Paus, B.R. Wood and V. Deckert, *J Dermatol Sci*, 2011, **63**, 191-198
2. J. Andanson, K. Chan and S. Kazarian, *Appl Spectrosc*, 2009, **63**, 512-517.
3. K. Chan, F. Tay, C. Taylor and S. Kazarian, *Appl Spectrosc*, 2008, **62**, 1041-1044.
4. K. Lau, B.R. Wood, J.E. Kloepper, K. Bambery, R. Paus and V. Decker, *Exp Dermatol*, 2010, **19**, 221.
5. K. Lau, B.R. Wood, J.E. Kloepper, R. Paus and V. Deckert, *Exp Dermatol*, 2010, **19**, 223.
6. C. Ryan, E. Clayton, W. Griffin, S. Sie and D. Cousens, *Nucl Instrum Meth B*, 1988, **34**, 396-402.
7. K. Pearson, *Philos Mag*, Series 6, 1901, **2**, 559-572.
8. C. Burges, *Data Min. Knowl. Discov.*, 1998, **2**, 121-167.

9. C. Chang and C. Lin, LIBSVM: A library for support vector machines, 2001.
10. E. Dimitriadou, K. Hornik, F. Leisch, D. Meyer, and A. Weingessel, e1071: Misc Functions of the Department of Statistics (e1071), TU Wien, 2010.
11. R. Kong, R. Reddy and R. Bhargava, *Analyst*, 2010, **135**, 1569-1578.
12. K. Potter, L. Kidder, I. Levin, E. Lewis and R. Spencer, *Arthritis Rheum*, 2001, **44**, 846-855.
13. I. Dreissig, S. Machill, R. Salzer and C. Krafft, *Spectrochim Acta A*, 2009, **71**, 2069-2075.
14. S. Krill, K. Knutson and W. Higuchi, *BBA*, 1992, **1112**, 281-286.
15. P. Wu and H.W. Siesler, *J. Near Infrared Spectrosc.*, 1999, **7**, 65-76.
16. S-H Lee, N.G. Mirkin, and S. Krimm, *Biopolymers*, 1999, **49**, 195-207.
17. M. Jackson, L-P Choo, P.H. Watson, W.C. Halliday and H.H. Mantsch, 1995, *BBA*, **1270**, 1-6

Chapter 5

Elucidation of infrared spectral features related to lipid contents in relation to human hair follicle mesenchymal stem cells



5.1 Abstract

The success of demonstrating the feasibility of distinguishing tissue compartments based solely on Fourier transform infrared (FTIR) spectra, encouraged the use of FTIR spectroscopy to differentiate cell types in the hair follicle mesenchyme. To gain a higher spatial resolution approximating the hair follicle dermal papilla (DP) cell size, FTIR point mapping was repeated on a hair follicle DP, using a smaller aperture. Focus was placed on the higher wavenumber region (2800-3500 cm^{-1}), due to contribution of lipids to this region, and empirical evidence showing lipids as important regulators of stem cell state. Since the higher wavenumber region contains IR absorption peaks attributed to C-H stretching of fatty acids (FAs), hence related to lipid features of the sample, possible FTIR lipid features that can be found in the DP were investigated. The putative correlation of the found lipid features in relation to the mesenchymal stem cells (MSCs) in the DP was further explored.

5.2 Introduction

In Chapter 3 and Chapter 4, the application of FTIR spectroscopy to the hair follicle has been demonstrated; the tissue compartments within the hair follicle were successfully discerned based purely on the infrared (IR) spectra¹.

According to the immunofluorescence staining of human hair follicles in skin sections^{2, 3}, the size of the mesenchymal cells in the follicle can be approximated to 5-10 μm . FTIR mapping is applied to a hair follicle bulb in a human skin section, focusing on capturing the DP and part of the lower connective tissue sheath (CTS) where MSCs can be found. FTIR mapping entails the recording of IR absorbance at a series of points over a predefined area. Each point, or pixel, in the FTIR map therefore contains an IR spectrum, from which information on the chemical composition can be extracted. In the present work, we increase the spatial resolution of the FTIR mapping by using a Cassegrain 36 \times objective, an aperture size of 0.45mm, resulting in spatial resolution of approximately 12.5 μm . The area was mapped at a step size of 5 μm . stepping closer to single cell resolution than our previous work shown in chapter 3.

In FTIR spectroscopy, where the pixel size of the imaging system is smaller than the wavelength of the IR radiation, the spatial resolution is said to be diffraction limited⁴, which also means that it is wavelength dependent⁵. In our forthcoming studies, focal plane array

(FPA)-FTIR which offers reduced pixel size will be employed. Thus, the focus for elucidating stem cell related features is placed on the higher wavenumber region of the IR spectrum (4000-2800 cm^{-1}).

Since the 2800-3050 cm^{-1} region of the mid-IR spectrum, also known as the C-H stretching region, contains ample information on lipids or fatty acids (FAs) of the sample, lipid information from the spectra were examined. Lipids play ubiquitous roles in cell biology⁶. Although stem cell lipodomics is an under-investigated area, there is certainly plenty of empirical evidence to support that lipids play important roles in governing stem cell state⁷⁻¹². The lipids that are important for stem cell state regulation include ceramides, FAs, and lipid rafts, which are cholesterol and sphingolipid rich platforms in the cell membrane

Ceramide signalling has been demonstrated to be crucial in stem cell motility^{7, 13}. FA, 10-hydroxy-trans-2-decanoic acid, promotes the differentiation of neuronal stem cells (NSCs)⁹. Lipid rafts, which are cholesterol and sphingolipids rich platform in the cell membrane, are found were found to have an important role in the migratory phenotype of stem cells^{8, 14} as well as self-renewal¹². Important stem cell state maintenance proteins such as Wnt and Hedgehog require post-translational palmitoylation, and also cholesterol modification for Hedgehog, to fully execute their roles^{11, 15, 16}.

Thus there are strong reasons to believe that MSCs in the human hair follicle can be distinguished from their differentiated neighbours based on differences in lipid contents, structures and concentration.

This study presents the variety of lipid features one can find in the hair follicle DP spectra. While the source of C-H groups may be of a mixed origin, an attempt is made to explain the possible relationship of the found lipid features to the stem cell properties of hair follicle MSCs. The delineation of lipid features present in the hair follicle mesenchyme provides possible features to focus on, in establishing unique MSC lipid spectral features.

5.3 Materials and methods

5.3.1 Human skin sections

Human skin sections were prepared as previously described in Chapter 3. Briefly, human skin cryosections of 5 μm were mounted on low 'e' MirrIR slides (Kevley, Ohio, USA) and were

fixed in 4% paraformaldehyde (PFA) in phosphate buffered saline (PBS) at room temperature.

5.3.2 FTIR mapping

The FTIR measurement was carried out using an IFS 28/B spectrometer (Bruker Optik GmbH, Ettlingen, Germany) which was coupled to an IR microscope, with a 36× Cassegrain objective with an aperture size of 0.45 mm. This resulted in a spatial resolution of approximately $0.45\text{ mm}/36 = 12.5\ \mu\text{m}$. An interval of $5\ \mu\text{m}$ was applied during FTIR mapping. The microscope was equipped with a mercury–cadmium–telluride (MCT) detector. 1024 interferograms were co-added for the background and each spectrum in the map was an average of 256 co-added interferograms.

5.3.3 Data processing

Univariate analysis: chemical images were plotted using CytoSpec© (www.cytospec.com). Multivariate analysis: unsupervised hierarchical clustering analysis (UHCA) was performed using CytoSpec software, over $2837\text{-}3099\text{ cm}^{-1}$ on the 1st derivative data. UHCA assigns a distance value for each spectrum, and clusters the spectra with similar distance values together. D-value distance method and Ward's algorithm clustering method were implemented.

5.4 Results and discussion

A FTIR map was recorded over the DP and lower CTS region of a human hair follicle, as illustrated in Fig. 1a. The FTIR map of the hair follicle was plotted into a chemical image based on the integrated intensity of $2990\text{-}2837\text{ cm}^{-1}$, containing C-H stretching bands attributed to FA contents in the sample (Fig.1b). It shows that the hair follicle matrix cells surrounding the DP contain higher levels of FAs than the DP. This trend in FA is consistent with previous findings from our group (see Chapter 3 and Ref¹), and from Mendelsohn and colleagues¹⁷. FTIR spectroscopic studies applied to human skin showed that the centre of the follicle is lipid poor, compared to the outer parts of the hair follicle^{1,17}. The areas corresponding to the hair follicle DP and CTS were selected as a region of interest for further clustering analysis. UHCA was performed on the C-H stretching region ($2990\text{-}2837\text{ cm}^{-1}$). UHCA groups similar spectra together, on the basis of a distance matrix; spectra with small

inter-spectral differences are assigned to one cluster¹⁸. Based on the dendrogram, five main clusters were present within this region of interest (Fig.1c,d).

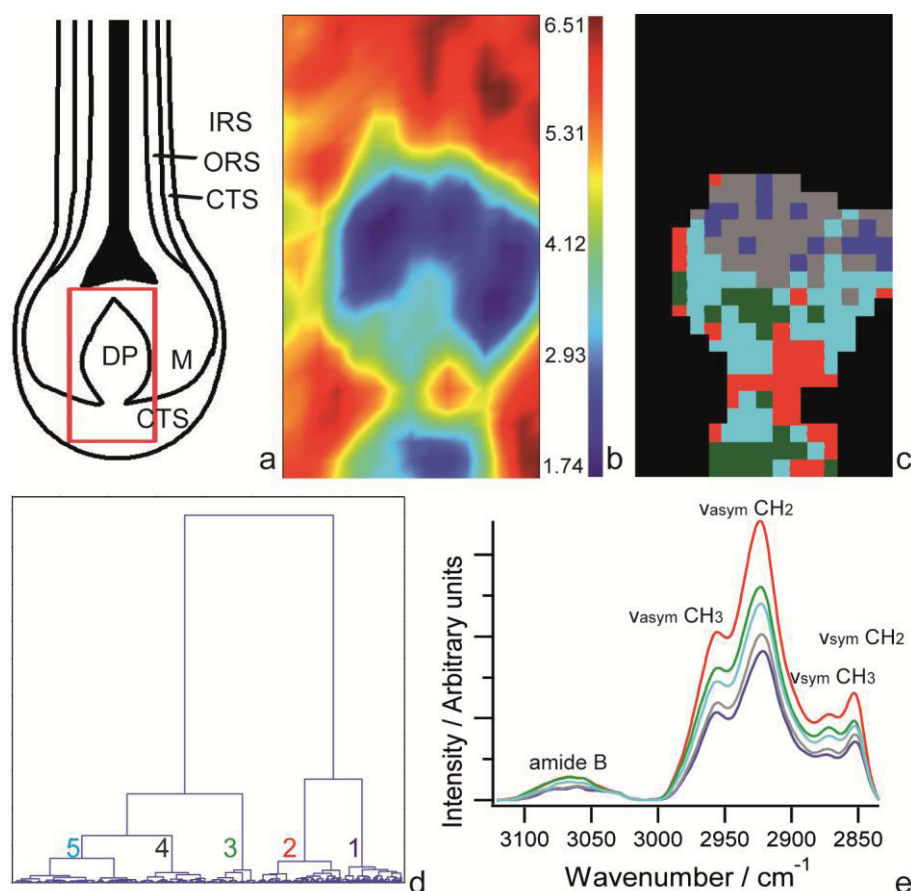


Figure 1a) An illustration of a human hair follicle. Marked in red is the FTIR mapped area. **b)** Chemical image of the FTIR map based on the integral of 2990 -2837cm⁻¹ of the original data. The DP is shown in the centre with very low level of FAs/ lipids. **c)** The DP and CTS areas are selected as region of interest for further analysis. The false colour image from the UHCA on the 1st derivative of the data over 2990-2837cm⁻¹ with five clusters. **d)** The dendrogram of the UHCA shows 5 main analytical clusters. **e)** The average spectra of the DP clusters in 1d are plotted in colours corresponding to the UHCA false colour image in 1c.

The baseline corrected average spectra of the DP clusters (Fig. 1e) and their second derivatives were compared. Analysis of the average spectra yielded three general classifications of lipid features, which varied between the clusters. These are: 1) overall amount of FAs, 2) ratio of FAs to proteins, and 3) shift in the wavenumber values of the FA peaks.

The red spectrum displays the overall highest level of FAs/lipids evinced by the asymmetric CH₂ and symmetric CH₂ stretching bands at 2924 and 2853 cm⁻¹ respectively¹⁹ (Fig.1e). By integrating the areas of the amide B band at 3068 cm⁻¹ (attributed to protein presence) and the

$\nu_{\text{sym}} \text{CH}_2$ band (attributed mainly to FAs/lipids), the ratio of FAs to proteins was found highest in the red cluster (Fig.2). Despite displaying the second highest overall FAs level, the green cluster displays the lowest FAs/lipids to proteins ratio (Fig.2). In the 2nd derivative of the average spectra, it is shown that the grey and the blue clusters contain acyl chains of lower wavenumber values (Fig.3) evinced by the positions of $\nu_{\text{asym}} \text{CH}_2$ band, which is attributed mainly to acyl chain structures of FAs. The $\nu_{\text{asym}} \text{CH}_2$ peaks at 2919 cm^{-1} in the grey and the blue spectra, are both 2 cm^{-1} lower than the light blue and green clusters, and 3 cm^{-1} lower than the red cluster.

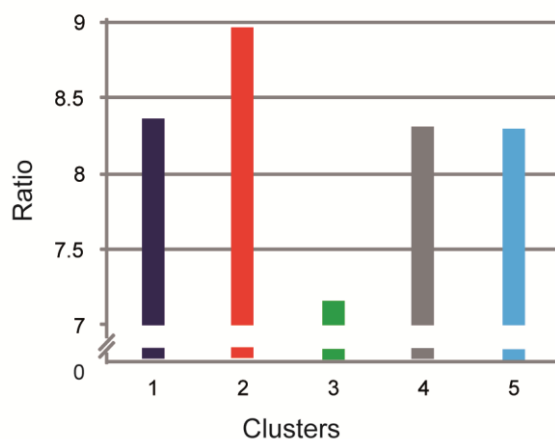


Figure 2. The bar chart shows the ratios of fatty acids to proteins, as calculated from the integrated areas of the amide B and the $\nu_{\text{sym}} \text{CH}_2$ peaks in the average spectra of the DP clusters. The colours correspond to those in Fig 1c.

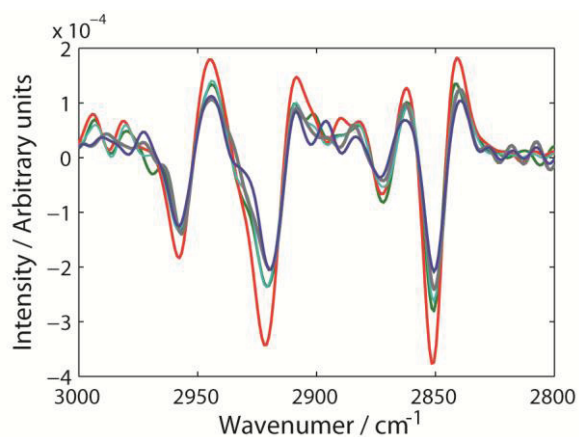


Figure 3 The DP clusters average spectra plotted in 2nd derivative, show there is a shift in wavenumber values for the CH_2 peaks. The $\nu_{\text{asym}} \text{CH}_2$ peaks in the blue and the grey clusters are shifted towards lower values. The colour coding corresponds to Fig 1c.

The higher overall intensity of acyl chains presence reflects an overall higher level of lipids, an indication of lipid storage in the stem cells. The MSCs are present in the DP and the CTS among their neighbouring differentiated cells without a specific niche. Yet they retain the

stem cell properties, such as self-renewal, asymmetric division and multi-potency. Normally slow-cycling in their tissue environment, MSCs can respond to stimulus such as an assault to skin, and proliferate rapidly to provide fibroblasts to repair the surrounding dermis²⁰. It is therefore logical that a lipid reserve exists in the MSCs to allow such rapid responses. This hypothesis is supported by a study on the early differentiation of human embryonic stem cells²¹, in which a rapid decrease in lipids was demonstrated once differentiation commenced. Moreover, lipid inclusions have been clearly imaged at least in the embryonic stem cells (ESCs)²².

The ratio of FAs to proteins was also investigated, since a lower protein level may also be a feature of the MSCs. Most adult stem cells (ASCs) are slow cycling *in vivo* and not highly migratory. Aside from proteins required for maintaining their stem cell state²³, the level of transcriptional activity of MSCs is expected to be lower than their differentiated counterparts. This hypothesis is further supported by a Raman spectroscopic study of murine embryonic stem cells (mESCs)²⁴ in which RNA and proteins were found to increase as spontaneous differentiation proceeded.

As phospholipids are the main components of cellular membranes, shifts in wavenumber values of the symmetric and asymmetric stretching CH₂ bands may reflect the different states of order of phospholipids in plasma membranes. A shift towards lower wavenumbers implies lower energy, and conceivably a higher state of order of FAs^{25,26}. Situations where FAs may be in a lower state of disorder may be: 1) a low number of branching, 2) long length of acyl chains, 3) higher degrees of saturation of acyl chains, or 4) abundance of *trans*- FAs. Such ordered structures may lead to lower acyl chain flexibility hence lower cell membrane fluidity. However, it should be noted that cholesterol is a main contributor on the membrane fluidity of plasma membranes in eukaryotic cells. The relationship between the order of acyl chains, and fluidity of cellular membranes is not easily understood and needs to be further elucidated²⁶. Furthermore, the cytoplasmic membrane accounts for only less than 5% of all cell membrane structures. Should there be a link between the order of the acyl chain and the fluidity of the membrane, this link may not reflect solely on the cytoplasmic membrane fluidity.

Nevertheless, decreased cell membrane fluidity potentially constitutes a defence mechanism protecting the stem cell pool, by reducing trafficking of molecules through the membrane²⁷, thereby discouraging the entry of foreign genetic materials²⁸. Increased plasma membrane fluidity has also been linked to the increase in motility²⁶ and proliferation. Indeed, lower cell

membrane fluidity was reported for proliferating stem cells compared to non-stem cells in the retina¹⁰. Last but not least, a structurally unsound nuclear membrane was postulated to be linked to the release of cancer-promoting or inhibiting signals from senescent breast cancer cells²⁹.

This study has illustrated the lipid FTIR spectral features that can be found in the hair follicle DP. Due to the knowledge that MSCs can be found in the DP, the focus has been placed on this hair follicle tissue compartment. Three lipid features potentially related to stemness were analysed: 1) overall FAs/lipids contents, 2) ratio of FAs to proteins and 3) shift in wavenumber values of CH₂ stretching bands. The possible relationship between these lipid features and stem cell properties have furthermore been discussed.

5.5 Outlook

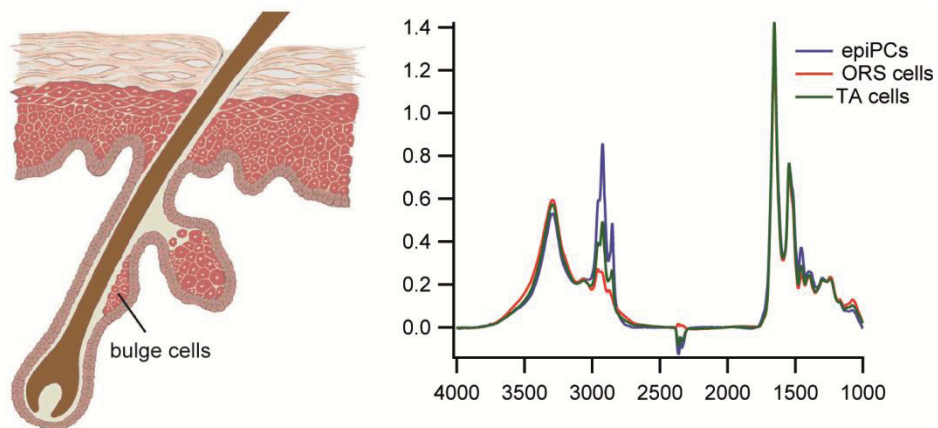
Further studies with higher spatial resolution and correlation to nestin immunostaining are required to locate the MSCs within the human hair follicle using FTIR spectroscopy. Despite the need for further studies, this study provides a systematic step, serving to clarify lipid features that should be focused on in future studies. Since the relationship between membrane order and fluidity needs further clarification, it was concluded that the focus should be placed on the overall FA/lipid contents and the ratio of FAs to proteins. Narrowing down to what lipid features to focus on in the infrared spectra will undoubtedly help develop FTIR spectroscopy as a tool for the identification of MSCs within the hair follicle. In addition, successfully identifying lipid features that can serve as spectral markers of a stem cell type, will provide important information on the involvement of lipids in maintaining stemness in the particular cell lineage. In the forthcoming studies, the FTIR lipid features identified in this study will be used as guides to locate the MSCs in the human hair follicle.

References:

1. K. Lau, M. Hedegaard, J. E. Kloepper, R. Paus, B. R. Wood and V. Deckert, *J Dermatol Sci*, 2010, **63**, 191-198.
2. S. Tiede, J. E. Kloepper, N. Ernst, B. Poeggeler, C. Kruse and R. Paus, *J Invest Dermatol*, 2009, **129**, 2711-2720.
3. C. Kruse, E. Bodo, A. E. Petschnik, S. Danner, S. Tiede and R. Paus, *Exp Dermatol* 2006, **15**, 794-800.
4. P. R. Griffiths, in *Infrared and Raman Spectroscopic Imaging*, eds. R. Salzer and H. W. Siesler, Wiley-VCH, Weinheim, 2009, pp. 3-64.
5. P. Lasch and D. Naumann, *BBA*, 2006, **1758**, 814-829.
6. T. T. Le, S. Yue and J.-X. Cheng, *J. Lipid Res.*, 2010, **51**, 3091-3102.
7. E. Bieberich, *Future Lipidol.* , 2008, **3**, 273-300.
8. R. Gniadecki and B. Bang, *J Invest Dermatol*, 2003, **121**, 522-528.
9. N. Hattori, H. Nomoto, H. Fukumitsu, S. Mishima and S. Furukawa, *Biomed Res*, 2007, **28**, 261-266.
10. J. Li, Z. Cui, S. Zhao and R. L. Sidman *Stem Cells*, 2007, **25**, 2864-2873.
11. K. Willert, J. D. Brown, E. Danenberg, A. W. Duncan, I. L. Weissman, T. Reya, J. R. Yates and R. Nusse, *Nature*, 2003, **423**, 448-452.
12. M. Y. Lee, J. M. Ryu, S. H. Lee, J. H. Park and H. J. Han, *J Lipid Res.*, 2010, **51**, 2082-2089.
13. G. Wang, K. Krishnamurthy, Y.-W. Chiang, S. Dasgupta and E. Bieberich, *J. Neurochem.*, 2008, **106**, 718-733.
14. B. Giebel, D. Corbeil, J. Beckmann, J. Hoehn, D. Freund, K. Giesen, J. Fischer, G. Koegler and P. Wernet, *Blood*, 2004, **104**, 2332-2338.
15. J. A. Porter, K. E. Young and P. A. Beachy, *Science*, 1996, **274**, 255-259.
16. H. Mao, A. M. Diehl and Y.-X. Li, *Lab Invest.*, 2009, **89**, 290-300.
17. R. Mendelsohn, H.-C. Chen, M. E. Rerek and D. J. Moore, *J Biomed Opt*, 2003, **8**, 185-190.
18. P. Lasch, W. Haensch, D. Naumann and M. Diem, *BBA*, 2004, **1688**, 176-186.
19. F. Shakeel, S. Baboota, A. Ahuja, J. Ali and S. Shafiq, *J Nanotechnol*, 2008, **6**, 8.
20. C. A. B. Jahoda and A. J. Reynolds, *The Lancet*, 2001, **358**, 1445-1448.
21. P. Heraud, E. Ng, S. ;, S. Caine, Q. C. Yu, C. Hirst, R. Mayberry, A. Bruce, B. R. Wood, D. McNaughton, E. G. Stanley and A. G. Elefanty, *Stem Cell Res*, 2010, **4**, 140-147.
22. E. Zuser, T. Chernenko, J. Newmark, M. Miljkovic and M. Diem, *Analyst*, 2010, **135**, 3030-3033.
23. T. Reya, A. W. Duncan, L. Ailles, J. Domen, D. C. Scherer, K. Willert, L. Hintz, R. Nusse and I. L. Weissman, *Nature*, 2003, **423**, 409-414.
24. I. Notingher, I. Bisson, A. E. Bishop, W. L. Randle, J. M. P. Polak and L. L. Hench, *Anal Chem*, 2004, **76**, 3185-3193.
25. S. L. Krill, K. Knutson, W.J. Higuchi, *BBA*, 1992, **1112**, 281-286
26. G. Taraboletti, L. Perin, B. Bottazzi, A. Mantovani, R. Giavazzi and M. Salmona, *Int J Cancer*, 1989, **44**, 707-713.
27. G. B. Laskay, R. E. Dale, J. Jelaneck, E. Spooncer and T. M. Dexter, *Growth Factors*, 1988, **1**, 67-73.
28. S. Das, S. Chakraborty and A. Basu, *J Neurochem*, 2010, **115**, 537-549.
29. M. M. Mariani, L. J. Maccoux, C. Matthaeus, M. Diem, J. G. Hengstler and V. Deckert, *Anal Chem*, 2010, **82**, 4259-4263.

Chapter 6

Label-free identification and study of epithelial progenitor cells from the adult human hair follicle



6.1 Abstract:

Epithelial progenitor cells (epiPCs) in the human hair follicle bulge are highly plastic, clonogenic and contribute to hair cycling and towards reepithelialisation during cutaneous wound healing. Due to their highly accessible location in the body and their plasticity, human hair follicle epiPCs are ideal autologous stem cells for stem cell based wound healing treatments. Current stem cell identification method requires labelling, rendering the stem cells unsuitable for direct application to patients. A prerequisite for isolating epiPCs for wound treatments is therefore reliable label-free identification. Thus, FTIR spectroscopy was applied to primary human hair follicle epiPCs and differentiated ORS cells for characterisation. Using established spectral features, FTIR imaging success-fully demarcated epiPCs within hair follicles in human skin sections. The FTIR data moreover provided information on the differentiation status of the epiPCs and their biology. This study forms the prerequisite for vibrational spectroscopy based epiPCs sorting from the hair follicle. In addition, as hair follicle epiPCs and hair follicle MSCs are derived from the same organ, epiPCs spectral features may serve as a pointer for MSCs identification using FTIR spectroscopy.

6.2 Introduction:

The human hair follicle epiPCs found predominantly in the bulge are well studied¹⁻³ and have been demonstrated to differentiate into all epithelial cell types⁴. The previous identification of the epiPC marker cytokeratin 15 (K15)^{4,2,5}, which is preferentially expressed in the human hair follicle bulge (Fig.1), has enabled the isolation of K15+ epiPCs from the human hair follicle bulge by plasmid transfection⁶. Although the cells are thought to be eventually rid of the plasmids after several passages⁶, the level of safety in using plasmid transfected cells for regenerative medicine is questionable. A label-free epiPCs isolation technique would streamline the isolation process and would be advantageous for regenerative medicine purposes.

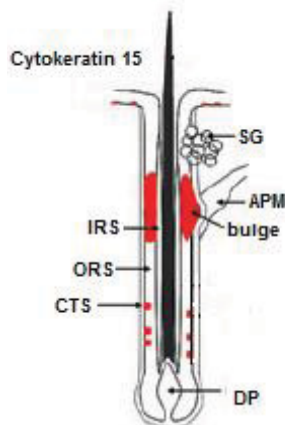


Figure 1 Schematic drawing of immunoreactivity pattern of cytokeratin 15 in the human pilosebaceous unit in red. APM, arrector pili muscle; CTS, connective tissue sheath; DP, dermal papilla; IRS, inner root sheath; ORS, outer root sheath. The figure is adapted from Ref².

The ability to identify stem cells through vibrational spectroscopic analysis and sort them would enable the direct application of the stem cells to patients. Through analysing single Fourier transform infrared (FTIR) spectra of isolated and selected primary hair follicle bulge epiPCs (see method described below⁸), unique IR spectral features of K15+ epiPCs were deduced. These features serve as markers for identifying K15+ epiPCs. In this chapter, the possibility to locate epiPCs within their habitat, by FTIR imaging the hair follicle bulge in human skin sections, is demonstrated. In addition, this chapter shows that not only can vibrational spectroscopy be used for tissue imaging and identifying epiPCs, the chemical information on the actual composition of the tissue revealed by the technique provides further knowledge on the biology of the epiPCs and ORS cells. Furthermore, establishing major variations in the chemical contents between epiPCs and committed ORS cells will provide a rough guide to distinguishing hair follicle mesenchymal stem cells (MSCs) from mature mesenchymal cells.

6.3 Materials and methods

6.3.1 Human Skin Sample origin

The origin of the skin sample is as described in Chapter 3.

6.3.2 K15 positive epiPCs and ORS cells on CaF₂ and quartz substrates

Primary K15+ epiPCs were isolated from human hair follicles from three patients by the non-viral transfection method as described in Ref⁶. K15+ epiPCs were selected by green fluorescent protein (GFP) expression, adhesion ability to collagen IV and geneticin resistance. Primary hair follicle outer root sheath (ORS) cells (as a differentiated control population) were isolated as described in Ref⁶. The primary cells were seeded on CaF₂, quartz and glass slides (one patient per substrate type) coated with collagen IV and fibronectin (Cellsystems, St. Katharinen, Germany) at a density of 10,000 cells/slide.

6.3.3 Skin section preparation

The skin sections preparation method is similar to that described in Chapter 3. Briefly, snap-frozen skin strips were cryosectioned at 8 μm thickness. The skin sections were mounted onto MirrIR low 'e' microscope slides (Kevley, Ohio, USA).

6.3.4 FTIR imaging

FTIR images were collected in transflection mode using a commercial FPA-FTIR spectrometer (model 670, Varian, USA) as described in Chapter 4. The resulting spectra were averaged from 64 co-add scans. Background spectra were taken from a blank area of the slide.

Single point infrared (IR) spectra were collected from K15+ epiPCs and ORS cells in transmission mode. The same spectrometer was used, this time equipped with a mercury-cadmium-telluride detector. The aperture size was approximately 50 μm and the number of co-add scans was 256. 65 measurements were taken from each group from randomly selected locations. Background spectra were regularly taken from blank areas of the slide and averaged from 512 co-added scans.

6.3.5 Statistical evaluation

6.3.5.1 Resonant Mie Scattering Correction (RMieS)^{7, 8}: RMieS was applied to correct the baseline and shifts in wavenumbers in the spectra due to Mie scattering⁴⁵⁻⁴⁸. Five iterations were chosen as further increase in iterations did not result in varied principal component analysis (PCA) results. The RMieS corrected data were evaluated by PCA⁹ using in-house scripts. For

PCA, the data had further been vector normalized and mean-centered. All the above mentioned analyses were performed using Matlab software (Mathworks, USA).

6.3.5.2 PCA: The single point spectra were analyzed using PCA on RMieS corrected (4000-1000 cm^{-1}), vector normalized and mean centered data. The results the scores are plotted against each other in a score plot. Two principal components (PCs) are considered, as two PCs sufficed to explain >99% of the data.

6.3.5.3 Unsupervised hierarchical clustering analysis (UHCA): The primary ORS and K15+ cells, as well as hair follicle IR image were analyzed with UHCA¹⁰⁻¹² using Cytospec© software (www.cytospec.com). UHCA was performed on the RMieS corrected spectra over the 2844-3450 cm^{-1} region.

For the hair follicle IR image, spectra outside the hair follicle ORS were omitted. UHCA was performed on the first derivative of the spectra over the 2840-3124 cm^{-1} region. For both clustering analyses, D-value distance method^{12, 13} and Ward's Algorithm clustering method^{12,14} were implemented. The number of clusters was selected based on the dendrogram of the UHCA.

The average raw spectra of the UHCA from the hair follicle IR map presented were split in upper and lower regions, vector normalized and baseline corrected (rubberband, 64 points) using OPUS software.

6.4 Results and Discussion

6.4.1 Viability of hair follicle K15+ epiPCs and ORS cells on the CaF_2 substrates affirmed

ORS cells and K15+ epiPCs were seeded at the same density on CaF_2 slides, which are optically transparent in the mid-IR range. Their rates of proliferation were 3:2 after the first passage, with the ORS cells more confluent. In later passages, the K15+ epiPCs continued to proliferate and demonstrated on-going clonogenic efficiency, whereas the differentiated ORS cells lost their

proliferative capacity within 3 passages⁶. This is in line with the literature as stem cells are reported to be more slow-cycling^{4, 15} than committed cells, but stem cells can self-renew¹⁵ and therefore continue to proliferate after prolonged passaging¹⁶. Both cell types had proliferated on CaF₂ substrates prior to fixation and were therefore viable cells.

6.4.2 Multivariate analysis applied to single FTIR spectra revealed heterogeneity within the K15+ epiPCs population

UHCA and PCA were applied to analyse the single spectra of ORS cells and K15+ epiPCs. To determine intrinsic similarities between the cells, UHCA was performed on 130 single spectra, 65 collected from ORS cells and 65 collected from K15+ epiPCs. In UHCA each spectrum is given a distance value. The spectra with the closest distances are grouped together as a cluster¹². According to the distance values, three major analytical clusters were derivable from this data set (Fig. 2a). Standard deviation values confirmed the three clusters are distinct from one another (data not shown). Spectra from K15+ epiPCs were segregated into clusters - 1 (red), 2 (blue) and 3 (green) whereas all ORS spectra belong to cluster 1 (red; Fig.2b). The result clearly indicates that cluster 1 (red) contains spectra of differentiated cells. 45% of the K15+ epiPC spectra belong to the cluster 1 (red) indicating that during the time primary isolated K15+ epiPCs were cultured on the CaF₂ substrate, cell differentiation occurred. The UHCA provided insight into a transient amplifying (TA) cell population, as two clusters exist for the remaining 55% of the non-terminal differentiated K15+ epiPCs, 22% of which belong to cluster 2 (blue), 33% of which belong to cluster 3 (green; Fig2b).

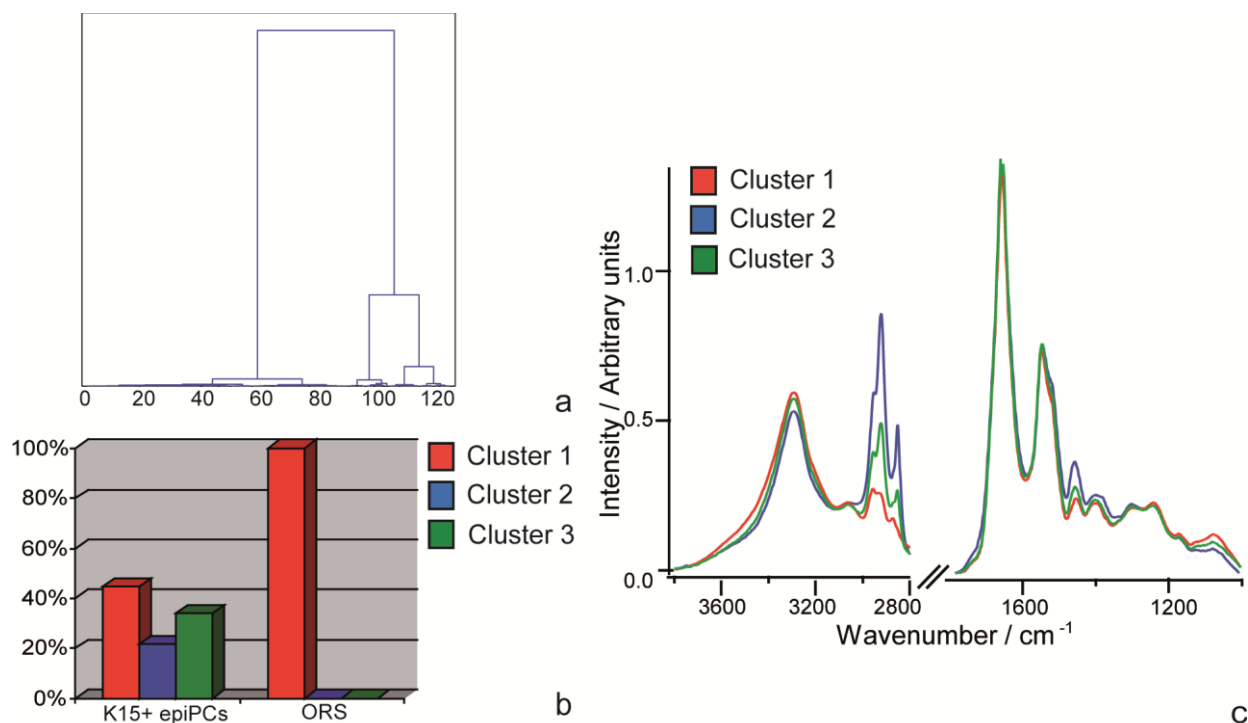


Figure 2a) Dendrogram of distance values from the unsupervised hierarchical clustering analysis, which was performed over 2844–3450 cm⁻¹ on the RMieS corrected spectra. Three main analytical clusters were derived. **b)** The bar chart shows the percentage of K15+ epiPCs and ORS cells that belong to the three clusters. 45% of the K15+ epiPCs belong to cluster 1, 22% belong to cluster 2, 38% belong to cluster 3. All ORS cells belonged to cluster 1. **2c)** The average spectra of the clusters of which the colours coding is explained in the legend. Cluster 1 - outer root sheath cells/ cells committed to differentiation; Cluster 2 - transient amplifying cells; Cluster 3 - human hair follicle epithelial progenitor cells.

PCA is one of the most used chemometric methods in multivariate analysis and aims to describe the complete variation in the data set using a reduced set of vectors called scores or PCs and loadings¹⁷. In doing so, PCA describes the most significant variance between the data. The first PC is found by calculating the vector best explaining the common variation in the data set. The second PC is then found as the vector describing the largest common variance not explained by the first component. Results from PCA performed on the pre-processed data displayed segregation along PC 1 (Fig.3) but not along other PCs. In Fig.1 the blue dots represent single spectra collected from K15+ epiPCs whereas red dots represent data from the ORS cells. Some blue dots (K15+ epiPCs) overlap with the red dots (ORS cells), indicating that some of the K15+ epiPCs have differentiated since being seeded on the substrate. The red dots being concentrated on PC1 indicates the ORS cells are mostly differentiated; the blue dots being highly scattered indicates the K15+ epiPCs display higher heterogeneity than the ORS cells. They were clearly at varied stages from progenitor cells, TA cells to differentiated cells, reflecting the asymmetric division

and self-renewal nature of stem cells. Nevertheless, the K15+ epiPCs that do display characteristics of PC1 loadings display them strongly, as the positive scores on PC1 reach further than the negative scores (0.4 vs. -0.1). 55% of the K15+ epiPCs are positive on PC1, 45% are negative, whereas 100% of the ORS cells are negative.

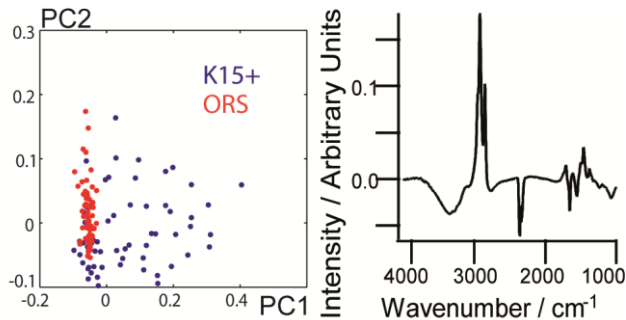


Figure 3: Results from principal component analysis on primary cytokeratin 15 positive (K15+) epithelial progenitor cells and outer root sheath (ORS) cells as presented in the main text. Left: Scatter plots of K15+ (blue) and ORS (red) cells along PC1 (x-axis) and PC2 (y-axis) show that K15+ cells are relatively heterogeneous whereas ORS cells are much more homogeneous. Right: PC1 loadings.

To verify the heterogeneity observed within the K15+ epiPCs population, the seeding procedure was repeated with primary hair follicle K15+ epiPCs and ORS cells from a different patient. Anti-K15 immunofluorescence staining also showed that some K15+ epiPCs display weaker immunofluorescence for K15 and have adopted a flatter morphology (Fig.4), an indication of exiting the progenitor cell state.

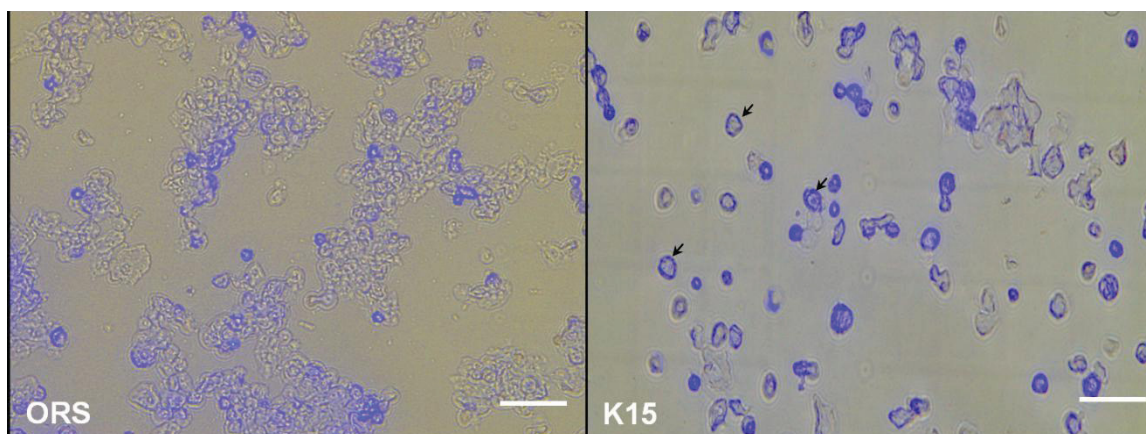


Figure 4 Hair follicle ORS cells and K15+ epiPCs isolated from a different patient were seeded on thin glass over slips. After adherence and proliferation, the cells were fixed in 4% PFA in PBS, and stained with anti-K15 primary antibody, and a secondary antibody conjugated with DyLight 350. DyLight 350 emits blue fluorescence when excited. The ORS cells are mostly K15 negative, but contain a small proportion of K15+ cells. Most K15+ epiPCs display strong immunoreactivity, though some display slightly weaker immunoreactivity and have adopted a flatter morphology (indicated exemplarily by arrows), likely due to their differentiation from progenitor cell to TA cell status. Scale bar: 50 μm .

6.4.3 Increase in total lipids and decrease in total proteins, established as a FTIR signature of K15+ epiPCs

UHCA results revealed a major downward trend for lipids from progenitor cells (blue) to differentiated cells (red). The average spectra (Fig.2c) display dramatic reduction in the intensity of the C-H stretching peaks between 2830-3000 cm^{-1} . This reduction can also clearly be seen in the difference spectra between the clusters (Fig.5).

Further IR spectra had been collected from K15+ epiPCs and ORS cells seeded on quartz substrates and were analysed (Fig.6). UHCA results presented here are consistent with the previous data regarding lipid and protein trends, at least in the 4000-2500 cm^{-1} region (as quartz is not IR transparent below 2000 cm^{-1}). Therefore, the choice of substrates did not influence the chemical contents of the cells, as previously had been suggested to be a possibility¹⁸. Thus, these lipid bands can reliably be used to distinguish K15+ epiPCs from differentiated ORS cells.

Agreeing with the decrease in CH_2 , the 1737, 1458, 1402 and 1380 cm^{-1} peak intensities also declined, from blue to green to red (Fig.2c), and indicated a reduction in lipid groups (Table 1) as differentiation proceeded from K15+ epiPCs.

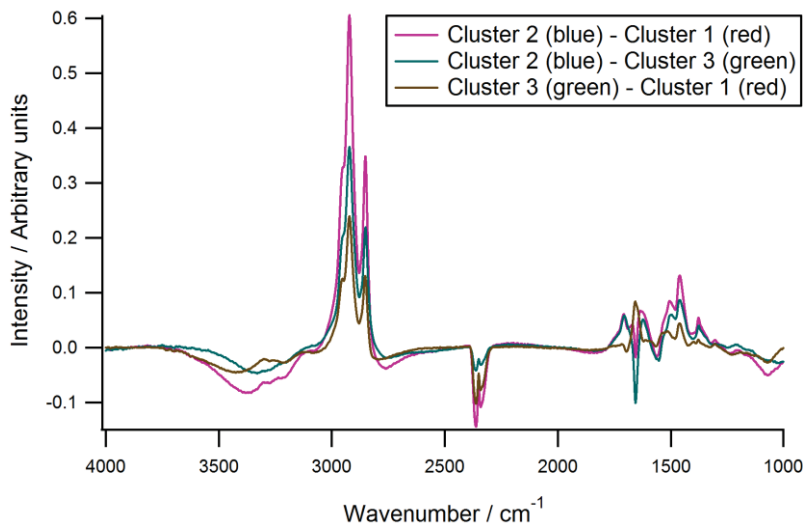


Figure 5. The difference spectra between the average clusters from the UHCA as shown in Fig. 1 are displayed. In purple is the difference spectrum between clusters 2 and 1; in teal is the difference spectrum between clusters 2 and 3; in brown is the spectrum between clusters 3 and 1.

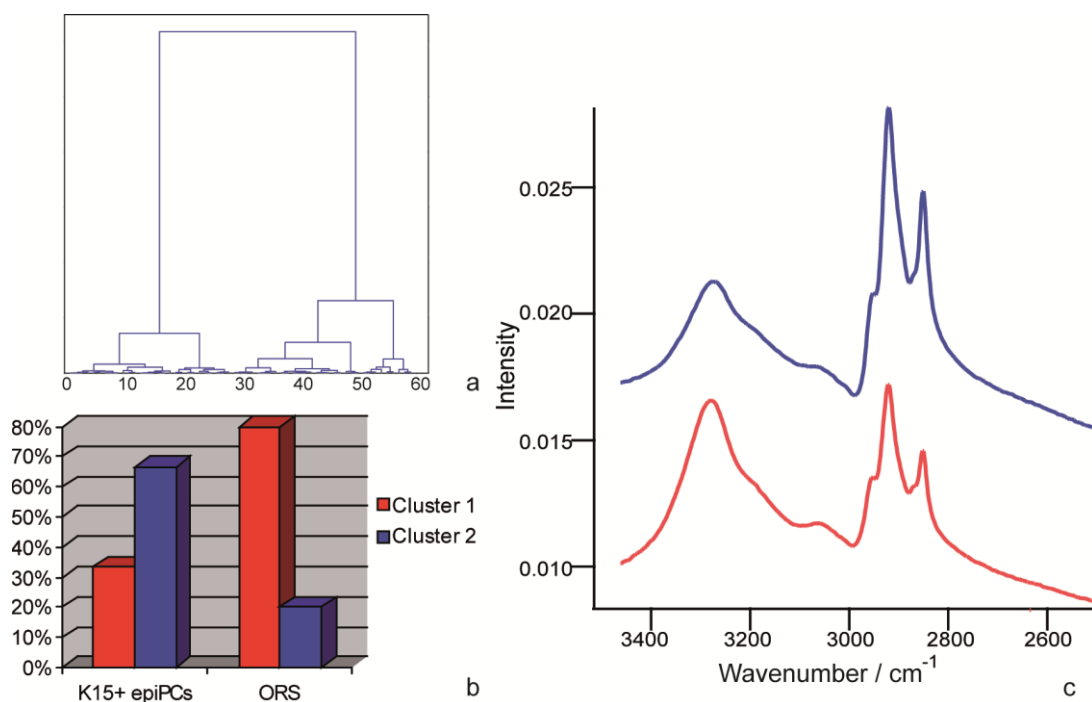


Figure 6a) Dendrogram from the UHCA results from a previous FTIR study on K15+ epiPCs (K15) and ORS cells seeded on quartz cover slips. **a)** Dendrogram of the UHCA. **6b)** Histogram showing the percentage of cells that belonging to cluster 1 (epiPCs) and cluster 2 (ORS cells) . **6c)** According to the average spectra, in the same colours as their corresponding clusters, the K15 cells contain significantly higher FAs (asymmetric and symmetric CH₂ stretching between 2800-3000 cm⁻¹) level than the ORS cells, whereas the ORS cells contain higher protein (amide A, near 3300 cm⁻¹) concentration than the K15 population.

Differences on proteins levels between the groups were also revealed. The UHCA results also show an increase in amide A intensity from blue (epiPCs) to green (TA cells) to red (differentiated cells). This is also seen in the difference spectra between the clusters – a minima is found at 3370 and 3329 cm^{-1} in the difference spectra between clusters 1 and 2 and between clusters 2 and 3 respectively (Fig.5). These results on protein levels are in agreement with published reports on the spontaneous differentiation of murine embryonic stem cells (mESCs) and human embryonic stem cells (hESCs), in which augmented levels of proteins were reported¹⁹⁻²¹.

Table 1 The assignment of bands from the unsupervised hierarchical clustering analysis average spectra for the epiPCs cluster. Upward arrows indicate relatively high level of presence and downward arrows indicate low level of presence compared to other clusters.

Assignment\ Cell type	Primary cells	Bulge	Ref
Amide A	3294 (↓)	3290 (↓)	40
Amide B	3063(flat)	3064 (↓)	40
C-H from C=C-H unsaturated fatty acids	NA	3009 (↑)	41
v_{asym} CH ₂ fatty acids	2924 (↑)	2923 (↑)	41
v_{sym} CH ₂ fatty acids	2853 (↑)	2852 (↑)	41
C=O from lipids	1739 (↑)	1741 (↑)	41
Amide I	1656 (↓)	1650 (↓)	42,43
Amide II	1548 (↓)	1540 (↑)	42,43
CH ₂ and CH ₃ deformation, aliphatic side groups of amino acid and lipids	1460 (↑)	1452 (2nd ↑)	42
	1377 (↑)	1398 (2nd ↑)	42
v_{asym} PO ₂ ⁻	1242 (↓)	1234 (2nd ↑)	44
v_{sym} PO ₂ ⁻	1080 (↓)	1080 (2nd ↑)	45

The combined spectral features for lipids and proteins strongly support the notion that cluster 2 (blue) represents the naïve K15+ epiPC; while cluster 3 (green) represents TA cells, an intermediate stage between progenitor cells and terminal differentiated cells. The naïve K15+ epiPCs becoming a minority in the sample after isolation, is consistent with a recent published study²². Under a culture condition which favoured stem cells, bulge cells from human hair follicle explants were isolated and expanded²². The epiPCs were shown to have divided asymmetrically²², producing highly proliferative daughter TA cells while maintaining a stem cell pool. The population that remained naive stem cells was a minority²².

6.4.4 FTIR spectroscopy revealed different trends in nucleic acids levels between hair follicle epiPCs and ESCs

FTIR spectroscopy not only unambiguously denoted spectral features that can be used to identify epiPCs from differentiated ORS cells, it also revealed on changes in nucleic acids levels. PCA applied to single ORS cells and K15+ epiPCs showed that ORS cells and the PC1 negative K15+ epiPCs had strong intensities at 1238 and 1073 cm^{-1} (Fig. 3), tentatively assigned to stretching vibration of PO_2^- of nucleic acids, as well as the peak at 1710 cm^{-1} assigned to C=O and C=N in plane stretching vibrations of DNA²³. The increase in nucleic acids suggests an increase in transcription in the differentiated cells. Conversely, mRNA levels were found to decrease during embryonic stem cell (ESC) differentiation, which signify translational activities^{19-21, 24}. This contradiction is due to the pre-existing pool of mRNA in ESCs, which is absent in adult stem cells (ASCs). ESCs are isolated from the blastocysts during early embryogenesis. In many animals, the early embryogenesis is programmed by the mRNAs present in the egg at the time of fertilization^{19,25}. Therefore during their early differentiation, the RNA contents decrease as translation from existing mRNA occurs; while at a later stage *de novo* transcription occurs. This was found at least on hESCs – after day 7 of spontaneous differentiation DNA/RNA hybrid was detected, signifying *de novo* transcription²⁴. ASCs on the other hand are maintained in undifferentiated states²⁶, and tend to be slow cycling²⁷ until directed to proliferate and differentiate⁴, during which transcription is required.

6.4.5 Spectral features suggest higher acyl branching in the more differentiated ORS cells

According to the UHCA results, both blue (epiPCs) and green (TA cells) spectra display higher $\nu(\text{CH}_2)$ than $\nu(\text{CH}_3)$ intensities, unlike the red (ORS cells) spectrum which displays higher $\nu(\text{CH}_3)$ to $\nu(\text{CH}_2)$ ratio at 2957 and 2874 cm^{-1} (Table 1; Fig.2c). The higher $\nu(\text{CH}_3)$ to $\nu(\text{CH}_2)$ ratio may be linked to a higher proportion of acyl chain branching {Wood, 2008 #157} in the differentiated cells.

6.4.6 Correlation of high lipid contents to lipid storage in stem cells

Stem cells are highly clonogenic *in vitro*²⁹, but ASCs tend to be quiescent in their niche hence label retaining method is a widely used method for identifying stem cells in tissue^{27, 30}. Stem cells are a source for daughter cells in tissue repair, such as the replenishment of dermal fibroblasts by MSCs in the hair follicle during cutaneous wound healing³¹. Therefore although they are normally slow cycling, once given the cue, stem cells can divide rapidly to provide daughter cells which differentiate into cell types required. Thus, it was hypothesized that certain resources exist to allow this rapid response from stem cells. Human bone marrow derived-MSC and hESCs had been shown to contain higher levels of glycogen, potentially as energy storage, than post-directed differentiation^{20, 32}. We did not observe changes in glycogen levels in the K15+ epiPCs. Nevertheless, hESCs displayed reduction in lipids during early differentiation towards mesoderm and ectoderm²⁰. Lipid inclusions have also clearly been detected in at least undifferentiated mESCs³³. Since lipid is required for synthesizing cellular membrane, it is consistent with our finding that K15+ epiPCs contain higher level of lipids than their more differentiated counterparts.

6.4.7 Changes in protein expression from progenitor cells to TA cells and their activated status

UHCA on single cell spectra revealed cluster 3 (green; TA cells) contained higher protein contents than clusters 1 (red; ORS cells) and 2 (blue; epiPCs). This is evinced by the higher amide I intensity (1548 cm^{-1}) in the corresponding spectrum (green, Fig.2c), and in the minima at 1658 and 1554 cm^{-1} in the difference spectrum of cluster 2 and cluster 3 (Fig.5). It is likely due to the TA cells being activated. *In vitro* TA cells are known to be highly migratory and proliferate rapidly³⁴ hence higher rate of protein synthesis. The amide II of the green and the red spectra

peak at 1548 cm^{-1} while that in the blue spectrum peaks at 1544 cm^{-1} and has a more pronounced shoulder at 1519 cm^{-1} (Fig.2c). This indicates a difference in the secondary structure of protein, and reflects the difference in protein contents. FTIR has thus shown that, once activated the TA cells start to synthesize proteins more similar to those found in differentiated cells. This rapid change in protein types was also true for the differentiation of hESCs^{20, 21, 24}.

To otherwise show the commencement of cells expressing lineage specific markers, destructive processes like qRT-PCR or immunocytochemistry would have to be employed²⁴.

6.4.8 FTIR imaging of the hair follicle bulge revealed the location of epiPCs with spectral features of primary K15+ epiPCs

Having shown that hair follicle epiPCs display higher lipid and lower proteins levels in their IR spectra compared to differentiated ORS cells, FPA-FTIR was applied to the hair follicle bulge in a human scalp skin section. It was examined whether epiPCs can be located within their natural habitat without labelling. The bulge area, recognized and defined as where the arrector pili muscle (APM) is connected to the hair follicle^{2,35-37}, was imaged (Fig.7a). The IR image was divided into 64×64 pixels and each pixel contained an IR spectrum. A chemical image (Fig.7b) plotted based on the integrated intensity of C-H stretching peaks, assigned to fatty acids, was for visualizing the ORS. The intensity of the FA levels is displayed in a 'hot/cold' colour scale – where there is a high FA concentration it appears red, and where there is a low concentration it appears blue. The upper hair follicle region is predominantly blue and is therefore mostly FA poor. The UHCA applied to the ORS (Fig.7c) successfully located an area within the ORS (blue cluster) of which the spectra contain the K15+ epiPCs spectral features – highest CH_2 peaks, moderate intensity at amide A, amide B, amide I and II (Fig.7d; Table 1). The false colour map shows that the epiPCs cluster (blue) lies in the outer layer of the lower bulge, which is in full agreement with previous reports².

A shift in RNA/DNA ratio was found in the blue cluster against the other clusters within the hair follicle bulge. A slightly more prominent shoulder at 1053 cm^{-1} in the 1080 cm^{-1} band (Fig.7c) indicates a higher DNA/RNA ratio³⁸. The other clusters in comparison to the blue cluster contain

higher RNA/DNA ratio. Thus, the higher RNA level in the more differentiated ORS cells in the bulge agrees with the findings from the primary K15+ epiPCs and ORS cells (Fig.2c).

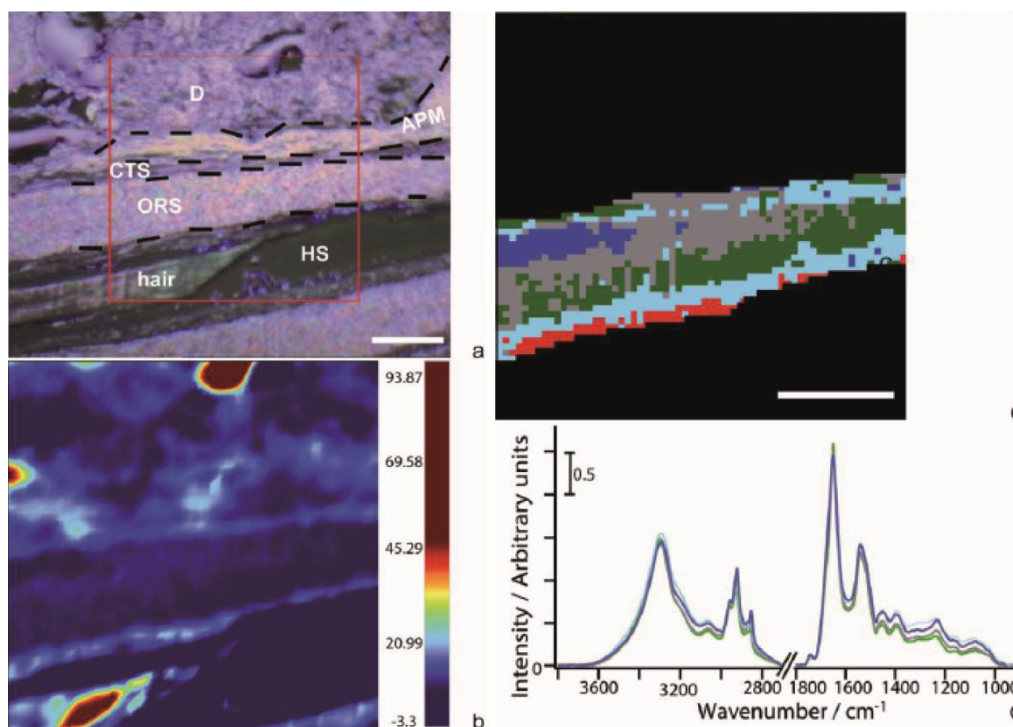


Figure 7a) Light microscopy image of the bulge area of a hair follicle in a human scalp skin section. Scale bar: 100 μm . D=dermis; CTS=connective tissue sheath; ORS=outer root sheath, APM=arrector pili muscle; HS= hair shaft. The red box indicates the mapped area. **b)** Chemical image plotted using the integrated intensity of $2836\text{--}3018\text{ cm}^{-1}$. The ORS area was chosen as the region of interest for further analysis. **c)** False colour map from the unsupervised hierarchical clustering analysis over $3111\text{--}2836\text{ cm}^{-1}$ on the 1st derivative of the data within the region of interest, with five clusters. The red cluster is deemed part of the inner root sheath (IRS) according to its position. **d)** Normalised and baseline corrected average spectra of the ORS clusters as seen in 3c, in corresponding colours. The red spectrum is not shown as it represents IRS.

6.4.9 Establishment of K15+ epiPCs spectral features and demonstration of their label-free identification within the hair follicle bulge paves way for future label-free epiPCs sorting

Using FTIR spectroscopy, we identified unique spectral features of K15+ epiPCs that can serve as intrinsic markers. Consequently, using these spectral markers, epiPCs can be distinguished from their more differentiated counterparts without any labelling. The further application of FTIR spectroscopy to live cells is straightforward and can therefore potentially identify living

epiPCs from more mature cells. Despite ubiquitous water molecules being IR active and usually obscuring IR spectra of biological samples, this impediment can be overcome by applying Synchrotron (SR)-FTIR spectroscopy^{39,40}. A SR light source is up to 100 times more brilliant than conventional IR sources and thus provides high signal-to-noise ratios, overcoming perturbation of cell spectra by water IR bands.

6.5 Conclusion

In summary, this study has identified high lipid and lower protein contents as a marker for the human hair follicle bulge epiPCs, compared to other cells in the ORS. This marker can be detected by FTIR spectroscopy without labelling or destroying the samples. FTIR spectroscopy also revealed manifold biological information ranging from the heterogeneity of the cell populations, to changes in the levels of proteins, lipids, transcriptional activities and methylation, to modifications in protein secondary structure.

Quantitative detection of changes in lipid levels is otherwise achieved only by destructive methods such as mass spectrometry⁴¹. Fluorescence lipid labelling may be employed for visualising concentration and distribution of lipid-rich structures in cells based on the fluorescence intensity^{42,43}. However, the efficiency of fluorescence tagging lipids highly depends on the type of fluorescent lipid molecules, thus affecting the reliability of this technique for quantitation⁴⁴. Adding exogenous lipid tags also risks changing the lipid-rich structures⁴⁴. Moreover, neither of these techniques is applicable to live cells. On the contrary, it is possible to retain spatial information and detect epiPCs within the bulge, based on the lipid levels with FTIR spectroscopy. Thanks to its non-invasive and label-free properties, vibrational spectroscopy such as FTIR is suitable for application to live cells. FTIR spectroscopy is therefore one of the very few techniques that can delineate alterations in lipid levels quantitatively in live cells.

Investigation of proteins and transcripts in biological samples currently relies on destructive techniques such as Western blot, immunohistochemistry and qRT-PCR. We demonstrated FTIR spectroscopy can reveal biological information on the cell types such as heterogeneity, protein

types in relation to the activated status of the TA cells, and level of transcription, without destroying the samples.

The present study succeeded in establishing spectral markers for human hair follicle epiPCs. Given the possibility of applying FTIR spectroscopy to live cells, this work paves way towards vibrational spectroscopy based stem cell sorting. In addition, since hair follicle epiPCs and MSCs come from the same organ. Therefore, establishing spectral features for epiPCs in comparison to their more mature counterparts provides a rough guide to distinguishing hair follicle MSCs from committed mesenchymal cells by FTIR spectroscopy.

References:

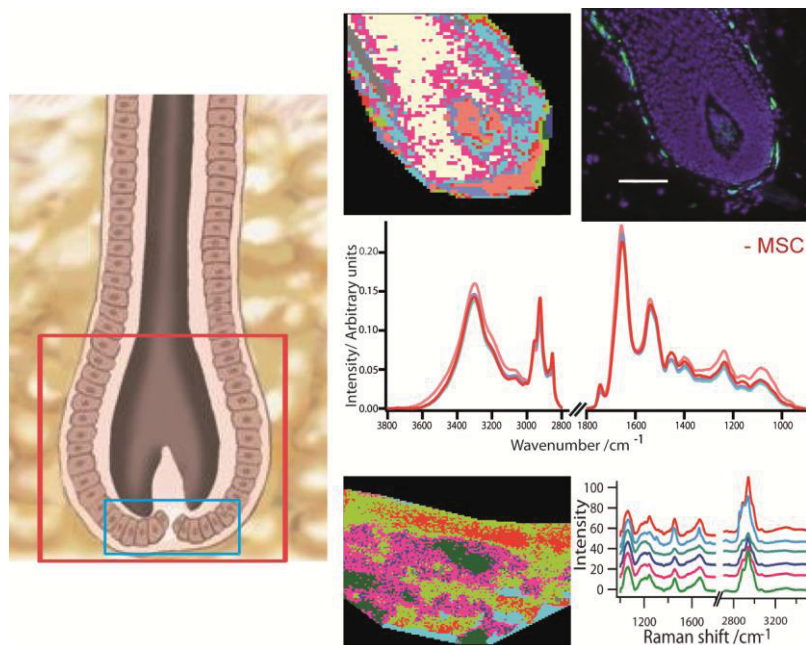
1. M. Ito, K. Kizawa, K. Hamada and G. Cotsarelis, *Differentiation*, 2004, **72**, 548-557.
2. J. E. Kloepper, S. Tiede, J. Brinckmann, D. P. Reinhardt, R. Faessler and R. Paus, *Exp Dermatol.*, 2008, **17**, 592-609.
3. M. Ohyama, *J Dermatol Sci*, 2007, **46**, 81-89.
4. R. Morris, Y. Liu, L. Marles, Z. Yang, C. Trempus, S. Li, J. Lin, J. Sawicki and G. Cotsarelis, *Nat Biotechnol*, 2004, **22**, 411-417.
5. S. Lyle, M. Christofidou-Solomidou, Y. Liu, D. E. Elder, S. Albelda and Cotsarelis G., *J Cell Sci* 1998, **111**, 3179-3188.
6. S. Tiede, N. Koop, J. E. Kloepper, R. Fassler and R. Paus, *Stem Cells*, 2009, **27**, 2793-2803.
7. P. Bassan, H. J. Byrne, F. Bonnier, J. Lee, P. Dumas and P. Gardner, *Analyst*, 2009, **134**, 1586-1593.
8. P. Bassan, A. Kohler, H. Martens, J. Lee, H. J. Byrne, P. Dumas, E. Gazi, M. Brown, N. Clarke and P. Gardner, *Analyst*, 2010, **135**, 268-277.
9. S. Wold, *Pattern Recogn.*, 1976, **8**, 127-139.
10. B. R. Wood, L. Chiriboga, H. Yee, M. A. Quinn, D. McNaughton and M. Diem, *Gynecol Oncol*, 2004, **93**, 59-68.
11. B. Bird, M. Romeo, N. Laver and M. Diem, *J Biophotonics*, 2009, **2**, 37-46.
12. D. Helm, H. Labischinski, G. Schallehn and D. Naumann, *J Gen Microbiol*, 1991, **137**, 69-79.
13. S. Sick, Reinker, S., Timmer, J., Schlake, T. and †, *Science*, 2006, **314**, 1447-1450.
14. J. H. Ward, *J Am Stat Assoc*, 1963, **58**, 236-244.
15. T. Tumber, G. Guasch, V. Greco, C. Blanpain, W. Lowry, M. Rendl and E. Fuchs, *Science*, 2004, **303**, 359-363.
16. C. Blanpain, Lowry, W.E., Geoghegan, A., Polak, L., Fuchs, E., *Cell*, 2004, **118**, 635-648.
17. S. Wold, K. Esbensen and P. Geladi, *Chemometr Intell Lab*, 1987, **2**, 37-52.
18. A. D. Meade, F. M. Lyng, P. Knief and H. J. Byrne, *Anal Bioanal Chem*, 2007, **387**, 1717-1728.
19. I. Notingher, I. Bisson, A. E. Bishop, W. L. Randle, J. M. P. Polak and L. L. Hench, *Anal Chem*, 2004, **76**, 3185-3193.
20. P. Heraud, E. Ng, S. ;, S. Caine, Q. C. Yu, C. Hirst, R. Mayberry, A. Bruce, B. R. Wood, D. McNaughton, E. G. Stanley and A. G. Elefanty, *Stem Cell Res*, 2010, **4**, 140-147.
21. H. G. Schulze, S. O. Konorov, N. J. Caron, J. M. Piret, M. W. Blades and R. F. B. Turner, *Anal Chem*, 2010, **82**, 5020-5027.
22. H. Yu, S. M. Kumar, A. V. Kossenkov, L. Showe and X. Xu, *J Invest Dermatol*, 2010, **130**, 1227-1236.
23. A. Cao, J. Liquier and E. Taillandier, in *Infrared and Raman Spectroscopy - Methods and Applications*, B. Schrader, VCH, Weinheim, 1995, pp. 344-372.
24. D. Ami, T. Neri, A. Natalello, P. Mereghetti, S. M. Doglia, M. Zanoni, M. Zuccotti, S. Garagna and C. A. Redi, *BBA*, 2008, **1783**, 98-106.

25. L. D. Smith and J. D. Richter, in *Biology of Fertilization: Model systems and oogenesis*, Academic Press, New York, 1985, vol. 1, pp. 141-188.
26. A. Spradling, D. Drummond-Barbosa and T. Kai, *Nature*, 2001, **414**, 98-104.
27. R. Kuwahara, A. V. Kofman, C. S. Landis, E. S. Swenson, E. Barendsward and N. D. Theise, *Hepatology*, 2008, **47**, 1994-2002.
28. M. Berman, A. Phatak, R. Lagerstrom and B. R. Wood, *J Chemometr*, 2009, **23**, 101-116.
29. J. Y. Liu, H. F. Peng, S. Gopinath, J. Tian and S. T. Andreadis, *Tissue Eng*, 2010, **16**, 2553-2564.
30. R. Morris and C. Potten, *J Invest Dermatol*, 1999, **112**, 470-475.
31. C. A. B. Jahoda and A. J. Reynolds, *Lancet*, 2001, **358**, 1445-1448.
32. C. Krafft, R. Salzer, S. Seitz, C. Ern and M. Schieker, *Analyst*, 2007, **132**, 647-653.
33. E. Zuser, T. Chernenko, J. Newmark, M. Miljkovic and M. Diem, *Analyst*, 2010, **135**, 3030-3033.
34. C. Roh, Tao, Q., Photopoulous, C. and Lyle, S, *J Invest Dermatol*, 2005, **125**, 1099-1105.
35. M. Ohyama, A. Terunuma, C. L. Tock, M. F. Radonovich, C. A. Pise-Masison, S. B. Hopping, J. N. Brady, M. C. Udey and J. C. Vogel, *J Clin Invest*, 2006, **116**, 249-260.
36. G. Cotsarelis, Sun, T.T. and Lavker, R.M., *Cell*, 1990, **61**, 1329-1337.
37. G. Cotsarelis, *J Invest Dermatol*, 2006, **126**, 1459-1468.
38. P. G. Andrus, *Technol Cancer Res Treat*, 2006, **5**, 157-167.
39. D. A. Moss, M. Keese and R. Pepperkok, *Vib Spectrosc*, 2005, **38**, 185-191.
40. H.-Y. N. Holman, K. A. Bjornstad, M. P. McNamara, M. C. Martin, W. R. McKinney and E. A. Blakely, *J Biomed Optics*, 2002, **7**, 417-424.
41. J. Li, Z. Cui, S. Zhao and R. L. Sidman, *Stem Cells*, 2007, **25**, 2864-2873.
42. L. Kuerschner, C. S. Ejsing, K. Ekroos, A. Shevchenko, K. I. Anderson and C. Thiele, *Nat Methods*, 2005, **2**, 39 - 45

43. D. M. Owen, A. Magenau, A. Majumdar and K. Gaus, *Biophy J*, 2010, **99**, L7-L9.
44. T. T. Le, S. Yue and J.-X. Cheng, *J Lipid Res*, 2010, **51**, 3091-3102.

Chapter 7

Locating Mesenchymal Stem Cells in the Human Hair Follicle Using FTIR and Raman Spectroscopy



7.1 Abstract

Compared to the epithelial progenitor cells (epiPCs), the human hair follicle mesenchymal stem cells (MSCs) are under-characterised and lack definitive markers. In chapter 6, Fourier transform infrared (FTIR) spectroscopy showed that, an increase in total lipids and a decrease in total proteins, were spectral features for hair follicle bulge epiPCs. In this chapter, FTIR imaging over the hair bulb region in human skin sections is shown to identify the positions of MSCs. Infrared (IR) spectra at the indicated MSC locations displayed higher lipid and moderate protein levels, strongly correlating with the findings on epiPCs. Corroboration by immunofluorescence staining with anti-nestin further supported these findings. Having shown the capability of FTIR spectroscopy for hair follicle MSC identification, the next step is to develop Raman spectroscopy-based MSCs identification, an avenue towards label-free sorting of live MSCs. Raman mapping was applied to the connective tissue sheath (CTS) and successfully differentiated mesenchymal cells from their extra cellular matrix (ECM), showing the possibility of establishing a MSC Raman signature, and consequently shows the potential of vibrational spectroscopy-based MSC identification.

7.2 Introduction

Vibrational spectroscopy has provided insight into changes in the lipid profile during stem cell differentiation. A study on the directed differentiation of human embryonic stem cells (hESCs) by Synchrotron (SR)-FTIR demonstrated a significant decrease in lipid levels during early differentiation¹, though directed differentiation towards neuronal cells resulted in an increase in lipids². In the previous chapter, FTIR spectroscopy was shown to be a viable tool for distinguishing human hair follicle epiPCs from their more mature counterparts both *in vitro* and *in situ*. It was found that epiPCs contained higher levels of lipids and moderate levels of protein compared to differentiated cells. These features in the spectra can serve as epiPC markers.

MSCs in the hair follicle co-exist with differentiated cells, but yet they have the self-renewal ability and plasticity, which would be reflected in their chemical composition. Since subtle variations in the spectra can be detected by statistical deconvolution methods³, FTIR spectroscopy combined with multivariate analysis should be able to discriminate MSCs from differentiated cells in the hair follicle. A combination of these techniques was thus applied to the hair follicle for locating the MSCs.

The aim of this work is to locate the MSCs in the hair follicle, and establish spectral variations between MSCs and differentiated mesenchymal cells in the hair follicle. Realising this goal will enable the identification of hair follicle MSCs by FTIR spectroscopy, allowing further characterisation of the MSCs by Raman spectroscopy, which offers higher spatial resolution than FTIR spectroscopy. In this study, FTIR maps were collected using focal plane array (FPA)-FTIR from hair bulbs in human skin sections, and the lipid features in the spectra of dermal papilla (DP) and CTS cells were correlated to those previously seen in the bulge epiPCs spectra. Hair follicle MSCs were located through FTIR imaging and unsupervised hierarchical clustering analysis (UHCA). The results were additionally corroborated by anti-nestin immunostaining.

Raman mapping was further conducted on the lower CTS of a hair follicle in a skin section, to demonstrate the feasibility of recognising distinct cells within the tissue based on Raman spectra. The data presented in this study paves way towards vibrational spectroscopy-based hair follicle stem cell identification and subsequent isolation of stem cell populations.

7.3 Materials and methods

7.3.1 Human skin sample origin

The origin of the skin sample is as described in Chapter 3.

7.3.2 Skin sections preparation

The skin section preparation procedure for FTIR spectroscopy is similar to the description in Chapter 3. Briefly, snap-frozen skin strips were cryosectioned at 8 μm thickness and skin sections containing anagen VI hair follicles were mounted onto MirrIR low 'e' microscope slides (Kevley, Ohio, USA). The sections were fixed with 4% paraformaldehyde (PFA) in phosphate buffered saline (PBS) at room temperature.

7.3.3 Immunohistochemistry – nestin staining (for correlation to FTIR mapping)

For anti-nestin staining, alternate skin sections (adjacent to the sections mounted on Kevley slides) were mounted on Super Frost® glass slides (Thermo-Scientific, Germany). The skin sections were fixed in acetone at $-20\text{ }^{\circ}\text{C}$ for 10 mins. Mouse anti-human nestin (5C93): sc-

71665 (Santa Cruz, California, USA) antibody was applied, using the tyramide amplification system (Perkin-Elmer, Boston, MA, USA) as previously described⁴. The amplification in tyramide (amplification reagent) was 1:50 for FITC.

Images were collected with a Biozero-8100 microscope, using a $\times 20$ objective in combination with the Biozero-Image-Analyzer software, version 2.5 (all Keyence, Osaka, Japan).

7.3.4 Immunohistochemistry – nestin staining (followed by Raman spectra collection)

Skin sections were mounted on quartz slides and fixed in 4% PFA (in PBS) at room temperature for 20 mins. The sample anti-human nestin antibody as above was applied. Then mouse-anti-human secondary antibody conjugated to DyLight 350 (Thermo-Scientific, Germany; excitation /emission maxima = 353/432) was applied. Fluorescence images were taken with a Biozero-8100 microscope.

7.3.5 FTIR spectroscopy

FTIR images were collected in transflection mode using a commercial FTIR spectrometer (model 670, Varian, USA) and an FTIR microscope with a 64×64 FPA detector (model 620, Varian). The microscope was equipped with a Cassegrain $\times 15$ /NA 0.4 objective. The microscope chamber was enclosed in a home-built chamber and purged by dry air to reduce spectral contributions from water vapour. Each image covers an area of $350 \times 350 \mu\text{m}^2$ where each pixel corresponded to an area of $5.5 \mu\text{m} \times 5.5 \mu\text{m}$, approximating a cell size. The resulting spectra were averaged from 64 co-add scans. Background spectra were taken from a blank area of the slide.

7.3.6 Raman spectral collection

7.3.6.1 Raman map on CTS: A Raman spectrometer coupled to a confocal microscope (WITec, Ulm, Germany) was employed for mapping the bulb region of the hair follicle. The Raman scatter was induced by 514 nm laser. Using a $20\times$ NA 0.4 objective, the spatial resolution was approximately 800 nm. Using a 600 g/mm grating (BLZ 500 nm), the spectral resolution was 4 cm^{-1} . 142×106 points were measured over $110 \times 82 \mu\text{m}^2$ over the lower CTS. Each spectrum was acquired over a 5 second integration time and at a laser power of approximately 6 mW.

7.3.6.2 Single point Raman spectra collection on stained skin section:

The same Raman spectrometer as above was used. The Raman spectra were collected using a $\times 20$ NA 0.4 objective, 600 g/mm (BLZ 500 nm) grating, 514 nm laser wavelength, approximately 8 mW laser power, acquisition time 10 seconds.

7.3.7 Statistical evaluation

7.3.7.1 UHCA: The hair follicle IR maps were analysed with UHCA^{5,6} using Cytospec© software (www.cytospec.com). The spectra outside the hair follicle region were omitted from the analysis. UHCA was performed on the first derivative of the spectra over the 2840-3124 cm^{-1} region, using D-values as distance method^{7,8} and Ward's Algorithm as clustering method^{8,9}. The number of clusters was selected based on the dendrogram of the UHCA and what was required to show the anatomical details. The average raw spectra of the UHCA were split in upper and lower regions, vector normalised and base-line corrected (rubberband, 64 points) using OPUS software (Bruker Optics, USA).

7.3.7.2 Raman map processing: The CTS Raman map was pre-processed using CytoSpec and went through cosmic spike removal, vector normalisation on the spectral range 550-4000 cm^{-1} , and polynomial baseline correction. UHCA was performed on the pre-processed data over 900-1750 and 2800-3100 cm^{-1} . Seven clusters were derived from this analysis, based on the dendrogram of the distance values and number of clusters required to represent of the cell/tissue components.

7.4 Results

7.4.1 Visualisation of single cells within their natural habitat using FTIR and UHCA

As published recently¹⁰, nestin+ cell were the most prominent in the CTS of the lower hair follicle. For this reason FTIR imaging was performed on the hair bulb regions of sectioned human scalp skin, which contain the lower CTS and the DP. Hair follicle FTIR map 1 (from here on referred to as map 1) was recorded from the hair bulb as shown in Fig.1a. The estimated mapped area is marked by the red box. The chemical image based on the integrated intensity of amide I clearly distinguished the follicle (high protein) from the surrounding subcutis (SC; low protein) (Fig.1b) and enabled the selection of follicle spectra for UHCA.

Six was the minimum number of clusters for visualising all tissue compartments (Fig.1c). Light blue and pink clusters represent the location of hair follicle matrix and epithelial cells. The grey region represents the DP. The green and blue regions represent the CTS and the red cluster represents non-removed SC spectra.

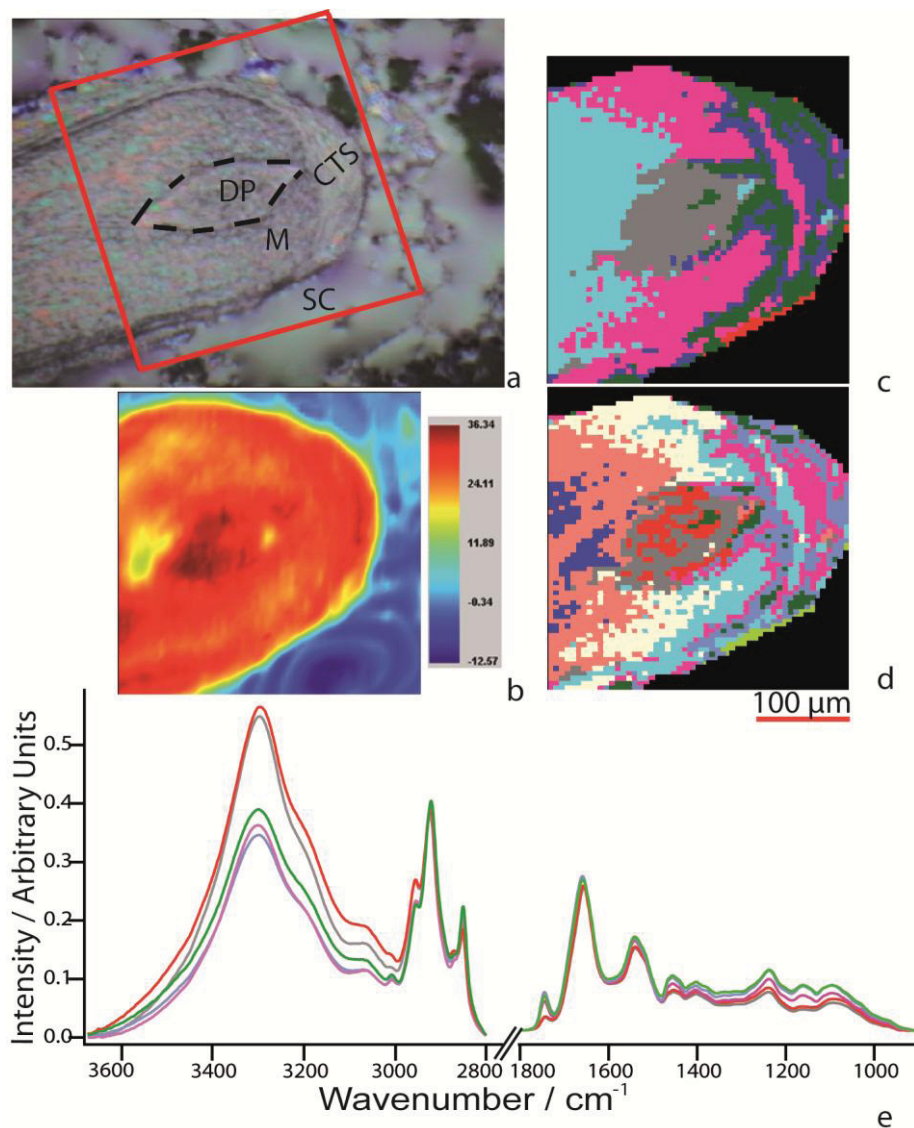


Figure 1: Map 1. 1a) Hair follicle overview using brightfield microscopy; the purple hue was due to the reflection mode. The FTIR region imaged is within the red box. 1b) Chemical map based on the integrated intensity of amide I in map 1. 1c) UHCA false colour image with 6 clusters, differentiate the tissue compartments. 1d) UHCA false colour image with 10 clusters further differentiate cell components within the tissue layers. 1e) Average spectra of the hair follicle DP and CTS clusters, after vector normalisation and rubberband baseline correction (64 baseline points).

As the number of clusters increased, further differentiation within the tissue compartments occurred (Fig.1d). As MSCs are found only in the DP and the CTS, only the clusters found in

DP and CTS were compared. In the 10 clusters image, the DP and CTS clusters are in grey, red, green, pink and mauve. Spectra belonging to the green cluster can be found in both DP and CTS. The green spectrum, whilst displays the most prominent C=C-H peak, along with peaks at 2924, 2852, 1456 and 1402 cm^{-1} assigned to saturated fatty acids (satFAs), lipids and phospholipids (see Table 1 for assignments), exhibits lower amide A, amide B, amide I and II levels than the other mesenchyme clusters (Fig. 1e). The green cluster, in terms of its chemical content, thus most resembles the cytokeratin 15 (K15) positive epiPCs as seen in the previous chapter.

7.4.2 Verification with a second data set and scalp skin hair follicle immunohistochemistry

A second data set (hereafter referred to as map 2) was used to verify whether FTIR and UHCA were suitable for distinguishing single cells from the hair follicle. The adjacent skin section to that of Map 2 was stained with anti-nestin antibody to confirm MSC locations indicated by FTIR and UHCA matched the immunoreactivity pattern or nestin. FTIR Map 2 was recorded over the hair bulb in Fig. 2a and the approximate mapped area is as indicated in the red box. The section consists of a hair bulb with the outer third or quarter of the DP. From the bright-field image, DP cells were identified. A chemical image, based on the integrated intensity of amide I in the raw data, is shown in Fig. 2b. The spectra from SC were extracted for further analysis. The resulting chemical image presents areas of high protein concentration in warmer colours and areas of low protein concentration in cooler colours. A red strip can be seen in the DP area indicating either particularly high protein concentration is found or that part of the tissue is thicker. Should there be heterogeneity in tissue thickness, the issue was dealt with during UHCA, since the D-values distance method incorporates the normalisation function^{7,8}. At six clusters, UHCA sufficiently distinguished the tissue compartments (Fig. 2c) such as the blue cluster represents the outer root sheath (ORS), green the inner root sheath (IRS) and lower hair shaft, pink the CTS.

At ten clusters, further clustering within the tissue layers ensued (Fig. 2d). According to the average spectra of the CTS clusters, the blue cluster contains extremely high carbonyl ester lipid peak at 1745 cm^{-1} (Fig. 3). According to results as presented in Chapter 3 and Chapter 4, such high levels of lipids indicate the blue cluster represents SC. The green and the light green clusters also contain such a high level of lipids, according to the C=O peak intensity

(Fig. 3), rendering the clusters from these two clusters to be the outer cuticle of CTS interlacing with SC. The outer cuticle contains predominately collagen and is acellular compared to other tissue regions, rendering it unlikely to contain MSCs.

Focusing onto the pre-processed average spectra of the DP and CTS clusters only (Fig.4), it was found that the red cluster contains the highest level of fatty acids (FAs) and lipids evinced by the peaks at 2854, 2926, and 1745 cm^{-1} (see Table 1 for the assignment). The prominent peak at 3008 cm^{-1} , indicates clearly that unsaturated fatty acids (unsatFAs) are present in the red cluster. The red cluster contains a moderate level of proteins, of which collagen is one of the major constituents as evinced by the collagen triplet at 1279, 1234 and 1203 cm^{-1} (the highest peak at 1234 cm^{-1})^{11, 12}, which is a characteristic of connective tissue.

According to the apricot average spectrum (Fig. 4), the apricot cluster contains the highest level of proteins as evinced by the amide A, amide B, amide I and II peaks. Slight shift in the amide I and II bands can be observed (Fig.4) and as well the shoulder at 1517 cm^{-1} in amide II is less prominent in the apricot cluster, suggesting varied secondary protein structures.

Collagen is also a main constituent in the apricot cluster as evidenced by the collagen triplet between 1200-1300 cm^{-1} (Table 1). The shoulders are not as prominent as the red spectrum, suggesting an overlap between the collagen peaks and the PO_2^- peak at 1238 cm^{-1} . This hypothesis is further supported by the strong intensity of the peaks at 1088 and 968 cm^{-1} both of which are attributed to phosphates of nucleic acid remnants.

The comparison between the locations of the red cluster (Fig. 2d) and the nestin staining pattern on the adjacent section to map 2 (Fig.2e) lends further support to the red cluster being MSCs. Faint nestin staining is detected in the lower half of the DP and along the CTS. Note that since nestin is not a definitive marker of hair follicle MSC and the staining was performed on the section adjacent to map 2, the locations of the red cluster and the nestin+ cells did not exactly overlap. The general patterns within the follicle were, however, highly similar.

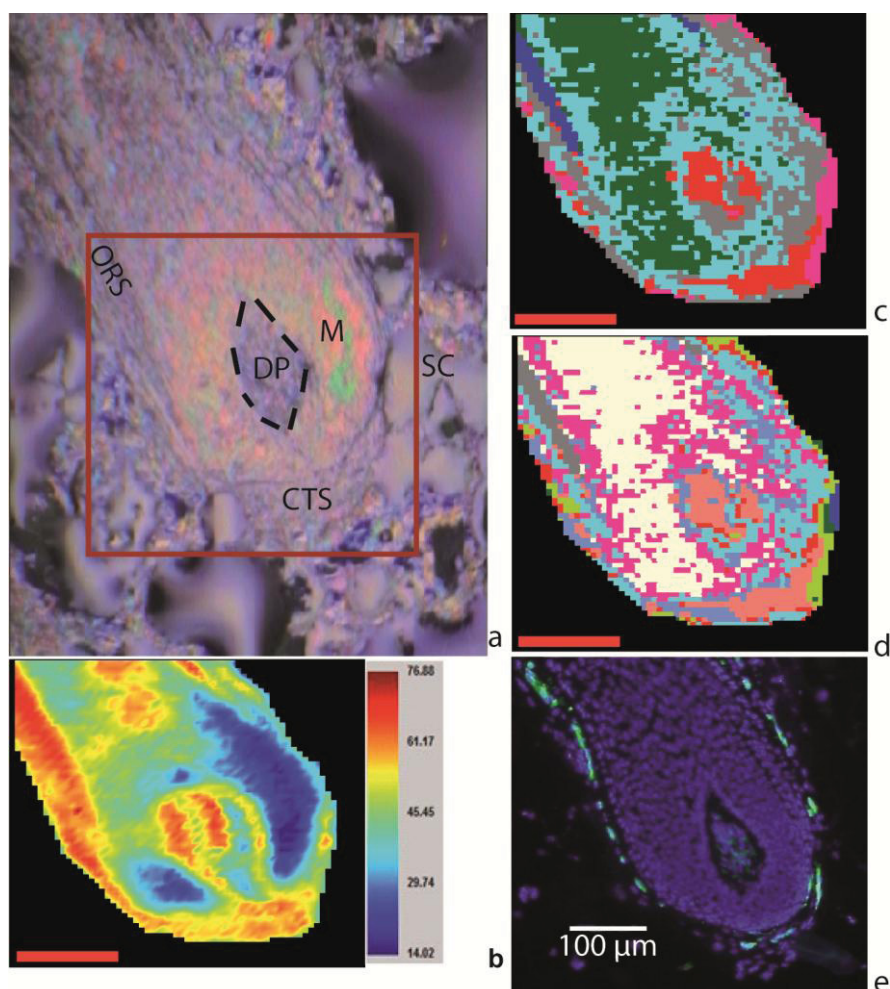


Figure 2: Map 2. 2a) Overview of hair follicle. The purple hue in this light microscopy image is due to the reflection mode. 2b) Chemical image of map 2 based on the integral of 1720-1590 cm⁻¹ (amide I), after removal of SC spectra. 2c) UHCA image with 6 clusters differentiate the tissue compartments within the hair follicle. 2d) UHCA false colour image with 10 clusters single out cell components within the tissue layers. 2b-d) Red colour bar: 100 µm. 2e) Adjacent section to map 2 stained with anti-nestin antibody (FITC) and DAPI counterstain.

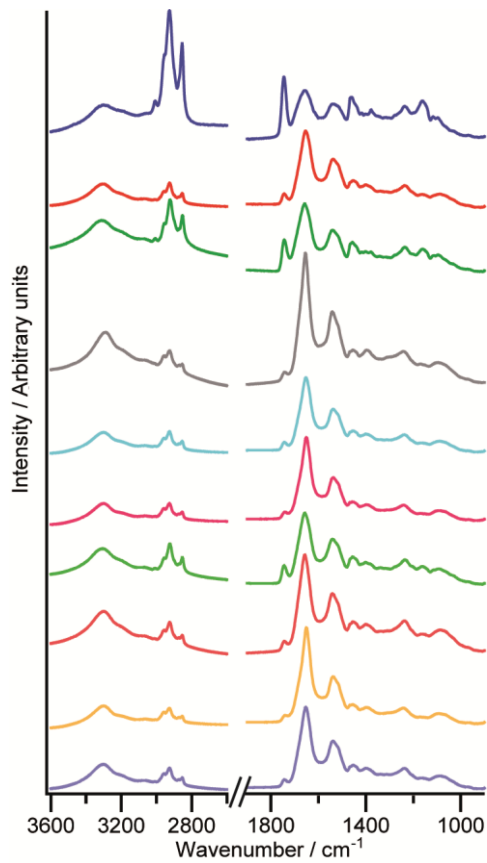


Figure 3) Original average spectra of all the clusters in the UHCA image of Map 2 with 10 clusters as in Fig.2d.

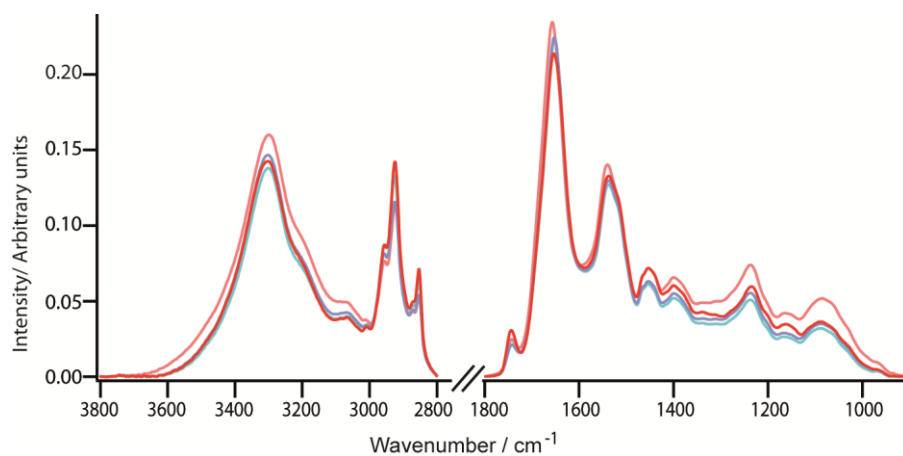


Figure 4) Vector normalised and baseline corrected average spectra of the hair follicle DP and CTS clusters as in Fig.2d.

Table 1 The assignment of bands from the UHCA average spectra. Upward arrows indicate relatively high level of presence and downward arrows indicate low level of presence compared to other clusters.

Assignment\ Cell type	Map 1 'MSC'	Map 2 'MSC'	Ref
Amide A	3300 (↓)	3302 (↓)	13
Amide B	3066 (↓)	3070 (↓)	13
C-H from C=C-H unsaturated FAs	3008 (↑)	3008 (↑)	14
ν_{asym} CH ₂ FAs	2924 (↑)	2926 (↑)	14
ν_{sym} CH ₂ FAs	2852 (↑)	2854 (↑)	14
C=O from lipids	1745 (2nd ↑)	1745 (↑)	14
Amide I	1659 (↓)	1655 (↓)	15, 16
Amide II	1541 (↑)	1539 (↓)	15, 16
CH ₂ and CH ₃ deformation, aliphatic side groups of amino acid and lipids	1456 (↑)	1454 (↑)	16
	1402 (↑)	1400 (↓)	16
Collagen triplet (amide III)		1279, 1234 and 1203 cm ⁻¹ (the highest peak at 1234 cm ⁻¹) (-)	11, 126, 47
ν_{asym} PO ₂ ⁻ nucleic acids	1238 (↑)	1238 (↓)	17
ν_{sym} PO ₂ ⁻ nucleic acids	NA	1088 (↓)	18

7.4.3 Confocal Raman mapping of the MSC-rich human hair follicle CTS successfully differentiated cell spectra

Confocal Raman mapping was also applied to the hair follicle as a further step towards label-free non-destructive living hair follicle MSCs identification. The successful identification of MSC locations in the human hair follicle by FTIR imaging demonstrated the applicability of vibrational spectroscopy as a label-free stem cell identification method. However, further methodological development is required for FTIR spectroscopy to be an identification tool for live MSCs due to water being infrared active. The presence of water perturbs the infrared spectra of cells rendering bench top FTIR spectrometers unsuitable for live cells application at present.

Raman spectroscopy is a vibrational spectroscopic technique that allows subcellular spatial resolution. Signals from water do not overlap with biological signals in the Raman spectrum, making Raman spectroscopy applicable to live cells. To explore this possibility, as a first step, it was investigated whether Raman imaging can distinguish mesenchymal cells from their ECM. Raman mapping was performed on the lower human hair follicle bulb within a scalp skin section (Fig.5a). As predicted, the chemical image based on the integrated intensity of 2843-2897 cm^{-1} (Fig.5b) shows the SC region as the highest in FAs level and the CTS striated. The CTS area of the Raman map was selected as the region of interest for UHCA.

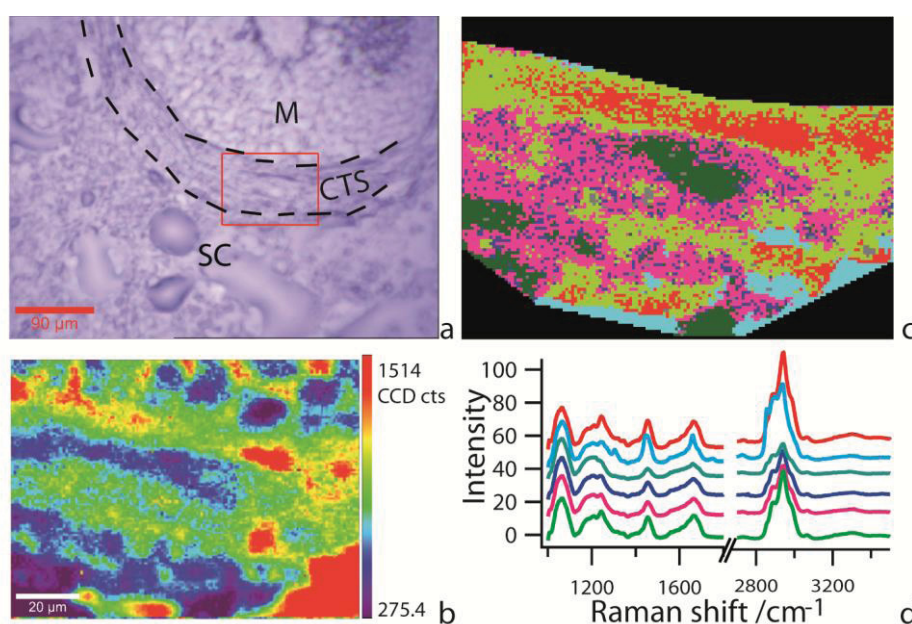


Figure 5a) Light microscopy image of the hair follicle. Scale bar: 100 μm . Marked in red is the area shown in 3b. **5b)** Chemical image of the mapped area based on the integrated intensity of 2843-2987 cm^{-1} . Scale bar: 20 μm . **5c)** shows the false colour map from the UHCA on the region of interest, with six clusters. **5d)** The average spectra are in colours corresponding to the colours of the clusters in the false colour map in 5c.

At six clusters it was possible to distinguish cell components from ECM and SC left in the map (Fig.5c). As seen from the light blue average spectrum (Fig.5d), the prevalent $\nu_{\text{sym}} \text{CH}_3$, as well as other lipid peaks as listed in Table 2, suggest the light blue cluster (Fig.5c) to be SC that was still included in the region of interest. Red and light green clusters were assigned ECM with collagen being specially detected in the red cluster (Table 2). The blue spectrum displays a glycol-protein peak at 1338 cm^{-1} , suggesting the blue cluster to represent glycoproteins. As the pink spectrum contains mainly protein and lipid peaks, and the green

spectrum contains mainly nucleic acids and protein peaks, the pink cluster is likely to be the cytoplasm and the green cluster the nuclei of the cells. Raman mapping and UHCA clearly distinguish spectra from cell components from the cells' surrounding. In this particular Raman imaging study, it was not yet clear whether some of these cells may be stem cells, as further corroboration with immunostaining is required in future investigations.

Table 2 Wavenumber values of Raman peaks in the fingerprint region and their respective tentative assignment. δ = deformation; ρ =bending; ν =stretching; ω =wagging

Cluster	Cluster assignment	Wavenumber (cm ⁻¹)	Raman band assignment
Red	ECM	1007	Phenylalanine ¹⁹
		1180	Tyrosine ²⁰
		1209	Tyrosine/Phenylalanine ²¹
		1243	Amide III/ collagen ²²
		1343	ω (CH ₂)(CH ₃)/Tryptophan ^{21, 23}
		1453	δ (CH ₂), (CH ₃) of methyl group, lipid, phospholipid/collagen ^{24, 25}
Light blue	Subcutaneous fat	1130	Phospholipid/fatty acids ²⁶
		1305	Lipids ²⁷
		1346	ω (CH ₂)(CH ₃)/Tryptophan ^{21, 23}
		1748	C=O lipid ²⁸
Blue	Glycoproteins	1235	Amide III ²⁴
		1338	Glycoprotein ^{29, 30}
Pink	Cytoplasm	1209	Tyrosine/ Phenylalanine ²¹
		1243	Amide III ²²
		1341	CH ₂ lipid ³¹
		1454	ρ_{sym} CH ₃ /phospholipids ²⁴
		1660	ν C=C lipid/amide I α -helix ^{30, 32}
Light green	ECM	1008	Phenylalanine ¹⁹
		1211	Tyrosine/Phenylalanine ²¹
		1240	Amide III β -sheet ²²
		1454	δ (CH ₂), (CH ₃) of methyl group, lipid, phospholipid/collagen ^{24, 25}
Green	Nuclei	1197	ρ N-H protein ³³
		1302	Adenine ⁴
		1343	Adenine, Tryptophan ²¹
		1339	Adenine ^{24, 34}

7.5 Discussion

7.5.1 K15+ epiPCs spectral features as a guideline for locating MSCs with FTIR

Since the $\nu(\text{C-H})$ region ($2800\text{-}3100\text{ cm}^{-1}$) in the IR spectrum is a dominant feature in most hair follicle spectra, deconvoluting the rationale for this became our focus. Moreover, not only does the IR wavelength in this spectral region directly enhance the spatial resolution, it is also an information-rich region. For instance, shifts in $\nu(\text{C-H})$ peak positions are strongly correlated to the state of disorder of the acyl chains in the cells. The ratio of the integral of $\nu_{\text{sym}}(\text{CH}_2)$ to $\nu_{\text{asym}}(\text{CH}_2)$ and $\nu_{\text{asym}}(\text{CH}_3)$ partly reflects the ratio of amino acids to lipids³⁵, while the $\nu_{\text{asym}}(\text{CH}_3)/\nu_{\text{sym}}(\text{CH}_2)$ ratio indicates the concentration of branched FAs relative to long chain FAs³⁵. In addition, the level of unsatFAs can be determined by the C-H stretching band from unsatFAs at 3010 cm^{-1} ³⁵. Furthermore, the level of FAs varies between cell lineages. The spectral features within the C-H stretching region are therefore potential spectral features for lineage identification.

Evidence supporting the role of lipids in stem cell state governance is plentiful. To name but a few: human embryonic stem cell (hESC) self-renewal was stimulated by albumin-associated lipids³⁶, indicating that lipids play a role in the hESC self-renewal. Important stem cell renewal regulators such as Wnt and Hedgehog proteins³⁷⁻³⁹ require post-translational lipid modification in order for them to be activated⁴⁰⁻⁴³. Retinal stem cells (RSCs) contain a higher proportion of satFAs in their plasma membrane phospholipids than the differentiated retinal cells. satFAs were found in proliferating RSCs but not in differentiated non-stem retinal cells⁴⁴. Ceramide was found to activate atypical protein kinase C ξ/λ (aPKC) in neural progenitor cells⁴⁵, which is required for adhesion and detachment during brain development⁴⁶. Inhibiting the *de novo* biosynthesis of sphingolipids in neural progenitor cells and deactivating ceramides resulted in the obliteration of neural progenitor cells motility and polarisation *in vitro*⁴⁷, which could be rescued by re-administering ceramides to the culture, through reactivating the aPKC pathway⁴⁷.

It is important to note that each stem cell type behaves differently, and exhibit different behavioural patterns *in vivo* from *in vitro*, supporting the known differences between primary cells and immortalised cell lines⁴⁸. While spontaneous embryonic stem cell (ESC)

differentiation by the removal of leukaemia inhibiting factor in the media resulted in a decrease in lipid levels, directed differentiation experiments show a decrease in lipid and glycogen storage. As described in Chapter 1, stem cells are highly clonogenic *in vitro*⁴⁹, but adult stem cells (ASCs) tend to be quiescent in their niche (hence label-retaining is a widely used method for identifying stem cells in tissue⁵⁰). Stem cells are a source for daughter cells when tissue repair is required, such as the replenishment of dermal fibroblasts by MSCs in the hair follicle during cutaneous wound healing⁵¹. Therefore, although they are normally slow cycling, once given the cue, stem cells are able to divide rapidly to provide daughter cells, which differentiate into the required cell types. Thus, we hypothesised that storage for lipid or glycogen resources would be present, to allow this rapid response from stem cells. Changes in glycogen level were not observed among the cell types in the hair follicle. However, since lipids are required for membrane synthesis, it is logical that ASCs contain higher lipid levels than their more differentiated counterparts. Also, stem cells being quiescent, show reduced transcription. Thus a lower degree of RNA and proteins were expected. It must also be kept in mind that ASC differentiation *in vivo* is directed by a myriad of signals, supporting its programmed differentiation. While epiPCs and MSCs belong to different embryonic lineages (ectoderm for the former and mesoderm for the latter) and may exhibit different trends, a closer relationship was nevertheless expected of the stem / progenitor cells in the same organ than of a completely different origin.

Walsh *et al*⁵² showed that the symmetric phosphate band at 1080 cm^{-1} in the IR spectrum could be used as a marker for human intestinal crypt stem cells, and it was supposed that this peak was due to an altered DNA conformation. For the putative hair follicle MSCs it was harder to comment on the level of transcription using this band since it overlaps with the collagen bands and collagen is present in the mesenchyme of the hair follicle.

7.5.2 The feasibility of FTIR spectroscopy in identifying hair follicle MSCs

The study on epiPCs, presented in Chapter 6, strongly indicated an increase in total lipids was a feature of the stem/progenitor cells of the hair follicle. Both 'high lipid' character and the locality of the cluster were used as a guide to locate MSCs in the hair follicle using FTIR spectroscopy. In both cases presented, the clusters found in both DP and CTS also exhibit the highest level of lipids in their spectra. The further correlation between the UHCA false colour image and the immunostaining of nestin supported the likelihood of them representing stem

cells. Although the stemness of the cells requires further confirmation by IR measurements on live cells, and their clonogenicity and multipotency further attested, the results strongly infer the feasibility of using vibrational spectroscopy to select stem/progenitor cells from their end-differentiated neighbours.

7.5.3 Potentials for MSC identification within the hair follicle demonstrated by Raman mapping of CTS, which distinguished CTS cells from their ECM

Raman mapping of the CTS, combined with UHCA, successfully differentiated CTS cells from their ECM. These preliminary data show the potentials of using Raman spectroscopy to identifying MSCs within the hair follicle. In order to establish Raman signatures and enable label-free sorting of hair follicle stem cells, one must ensure that Raman mapping is performed on the MSCs, and not on differentiated cells. Anti-nestin immunofluorescence staining will be employed in future works to select for putative MSCs prior to Raman mapping. Since Raman scattering is a weak process, the presence of fluorescence would normally greatly obscure the baseline and mask the Raman peaks. The collection of ‘clean’ Raman spectra from cells immunofluorescence stained with antibody can be realised by the innovative combination of a fluorochrome with low emission wavelengths (e.g. DyLight 350, of which excitation / emission maxima = 353/432), and Raman excitation at higher wavelengths (e.g. visible). An example of a Raman spectrum unaffected by fluorescence is shown (Fig.6).

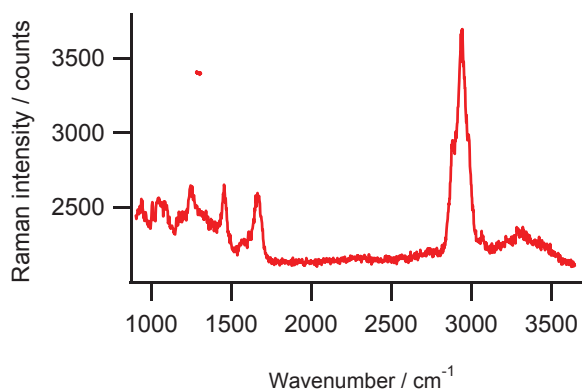


Figure 6 An example of a Raman spectrum collected from CTS immunostained with anti-nestin primary antibody and secondary antibody conjugated to DyLight 350. The Raman spectrum was collected from a point in the CTS of a hair follicle in a skin section mounted on a quartz slide. The laser wavelength used for Raman scattering was 514 nm. The spectrum was collected over 10 seconds using a 20× objective with a NA 0.4 with a WITec Raman microscope. Since the fluorescence excitation and the Raman excitation wavelengths do not overlap in this experiment, fluorescence is absent in the Raman spectrum.

7.5.4 Perspectives in the direction of cell sorting using vibrational spectroscopy

Despite water molecules being IR active and obscuring IR spectra of biological samples, this impediment has been overcome by applying SR-FTIR spectroscopy⁵³, which offers up to 100 times higher brilliance than a conventional IR source and therefore, enables a higher signal to noise ratio. IR spectra can be recorded from live cells in media using Synchrotron (SR)-FTIR, and FTIR was a good starting point for establishing spectral features of the hair follicle stem cells. In spite of that, the technological development pertinent to Raman spectroscopy suggests that live stem cells label-free sorting would be more likely to be realised by Raman spectroscopy. Raman activated cell sorting by marrying optical tweezers to Raman spectroscopy^{54, 55} is under development and looks to be highly promising. The subcellular spatial resolution achievable by Raman spectroscopy provides the opportunity to characterise selected cells in terms of the cell components. The preliminary study of CTS cells by Raman mapping presented in this chapter demonstrates the potentials of Raman spectroscopy in hair follicle MSCs identification within the tissue environment.

7.6 Conclusion

Previously extracted epiPC features were used as markers to identify MSCs from the hair follicle using FTIR spectroscopy. This study has demonstrated the feasibility of using FTIR spectroscopy to identify MSCs within their tissue environment. While further verification using live cells is desired, this study has provided the first step to this goal and shown promises of its achievability. The data presented in this study paves way towards vibrational spectroscopy-based stem cell sorting, with strong implications on enabling the use of autologous stem cells in treatments, eliminating immune reaction issues; abolishing the need to label the cells will also maximise the number of stem cells usable for stem cell based treatments.

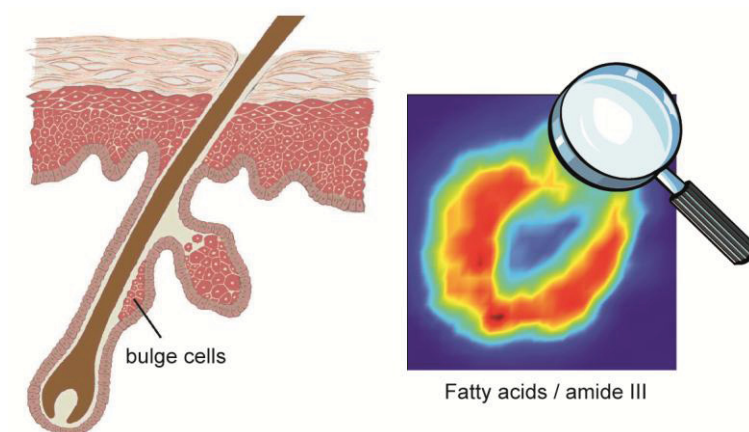
References

1. P. Heraud, E. Ng, S. S. Caine, Q. C. Yu, C. Hirst, R. Mayberry, A. Bruce, B. R. Wood, D. McNaughton, E. G. Stanley and A. G. Elefanty, *Stem Cell Res*, 2010, **4**, 140-147.
2. W. Tanthanuch, K. Thumanu, C. Lorthongpanich, R. Parnpai and P. Heraud, *J Mol Structure*, 2010, **967**, 189-195.
3. E. Goormaghtigh, A. Derenne, A. Benard, R. Gasper and V. Raussens, *Spectrosc*, 2010, **24**, 51-54.
4. J. E. Klopper, S. Tiede, J. Brinckmann, D. P. Reinhardt, R. Faessler and R. Paus, *Exp Dermatol.*, 2008, **17**, 592-609.
5. B. R. Wood, L. Chiriboga, H. Yee, M. A. Quinn, D. McNaughton and M. Diem, *Gynecol Oncol*, 2004, **93**, 59.
6. B. Bird, M. Romeo, N. Laver and M. Diem, *J Biophotonics*, 2009, **2**, 37-46.
7. , Editon edn.
8. D. Helm, H. Labischinski, G. Schallehn and D. Naumann, *J Gen Microbiol*, 1991, **137**, 69-79.
9. J. H. Ward, *J Am Stat Assoc*, 1963, **58**, 236-244.
10. S. Tiede, J. E. Klopper, N. Ernst, B. Poeggeler, C. Kruse and R. Paus, *J Invest Dermatol*, 2009, **129**, 2711-2720.
11. K. Potter, L. Kidder, I. Levin, E. Lewis and R. Spencer, *Arthritis Rheum*, 2001, **44**, 846-855.
12. A. Kohler, D. Bertrand, H. Martens, K. Hannesson, C. Kirschner and R. Ofstad, *AnalBioanal Chem*, 2007, **389**, 1143-1153.
13. R. Kong, R. K. Reddy and R. Bhargava, *Analyst*, 2010, **135**, 1569-1578.
14. I. Dreissig, S. Machill, R. Salzer and C. Krafft, *Spectrochim Acta A*, 2009, **71**, 2069-2075.
15. E. Pauthe, J. Pelta, S. Patel, D. Lairez and F. Goubard, *BBA*, 2002, **1597**, 12-21.
16. J. Babrah, K. McCarthy, R. J. Lush, A. D. Rye, C. Bessant and N. Stone, *Analyst*, 2009, **134**, 763-768.
17. Z. Hammody, S. Argov, R. K. Sahu, E. Cagnano and R. A. M. Moreha, S., *Analyst*, 2008, **133**, 372-378.
18. P. T. T. Wong, R. K. Wong, T. A. Caputo, T. A. Godwin and B. Rigas, *PNAS*, 1991, **88**, 10988-10992.
19. Y. Ozaki, H. Sato, D. Borchman and A. Mizuno, *Proceedings of the Fourteenth International Conference on Raman Spectroscopy, Section 5: Biomedical Applications*, 1994, 201-203.
20. T. Miura and G. J. J. Thomas, in *Subcellular Biochemistry: Proteins, Structure, and Engineering*, eds. B. B. Biswas and S. Roy, Plenum Press, New York, Editon edn., 1995, vol. 24.
21. K. A. Hartman, N. W. Clayron and G. J. J. Thomas, *Biochem Biophy Res Comm*, 1973, **50**, 942.
22. S. Keller, B. Schrader, A. Hoffmann, W. Schrader, K. Metz, A. Rehlaender, J. Pahnke, M. Ruwe and W. Budach, *J Raman Spectrosc*, 1994, **25**, 663-671.
23. C. J. Frank, *PhD Thesis, Ohio State University*, 1994.
24. A. Mahadevan-Jansen and R. Richards-Kortum, *J Biomedical Optics*, 1996, **1**, 31-70.
25. D. P. Lau, Z. Huang, H. Lui, C. S. Man, K. Berean, M. D. Morrison and H. Zeng, *Lasers Surg Med*, 2003, **32**, 210-214.
26. C. Krafft, L. Neudert, T. Simat and R. Salzer, *Spectrochim Acta A*, 2005, **61**, 1529-1535.
27. D. C. B. Redd, C. J. Frank, Z. C. Feng, T. S. Gansler and R. L. McCreey, *Proc. SPIE: Optical Biopsy*, 1993, **2081**, 185-189.
28. M. Shim and B. C. Wilson, *Photochem Photobiol*, 1996, **63**, 662-671.
29. Y. Tomimatsu, J. R. Scherer, Y. Yeh and R. E. Feeney, *J. Biol. Chem.*, 1976, **251**, 2290-2298.
30. M. M. Mariani, L. J. Maccoux, C. Matthaues, M. Diem, J. G. Hengstler and V. Deckert, *Anal Chem*, 2010, **82**, 4259-4263.
31. N.-T. Yu, X.-Y. Li and J. F. R. Kuck, in *Biomedical Applications of Spectroscopy* eds. R. J. H. Clark and R. E. Hester, John Wiley & Sons, 1996.
32. A. Alimova, R. Chakraverty, R. Muthukattil, S. Elder, A. Katz, V. Sriramoju, S. Lipper and R. R. Alfano, *J. Photochem. Photobiol.*, 2009, **96**, 178-183.
33. C.-C. Chuang, J.-S. Shiu and J.-L. Lin, *Phys. Chem. Chem. Phys.*, 2000, **2**, 2629-2633.
34. G. J. Puppels, in *Fluorescent and Luminescent Probes*, ed. W. T. Mason, 1999, pp. 377-406.
35. B. R. Wood, T. Chernenko, C. Matthaues, M. Diem, C. Chong, U. Bernhard, C. Jene, A. A. Brandli, D. McNaughton, M. J. Tobin, A. Trounson and O. Lacham-Kaplan, *Anal Chem*, 2008, **80**, 9065-9072.
36. F. R. Garcia-Gonzalo and J. C. Izpisua Belmonte, *PLoS ONE*, 2008, **3**, e1384.
37. T. Reya, A. W. Duncan, L. Ailles, J. Domen, D. C. Scherer, K. Willert, L. Hintz, R. Nusse and I. L. Weissman, *Nature*, 2003, **423**, 409-414.
38. J. de Boer, H. J. Wang and C. Van Blitterswijk, *Tissue Eng*, 2004, **10**, 393-401.
39. A. L. Derfoul, A. Carlberg, R. S. Tuan and D. J. Hall, *Differentiation* 2004, **72**, 209-223.
40. R. Nusse, *Development* 2003, **130**, 5297-5305.
41. M.-H. Chen, Y.-J. Li, T. Kawakami, S.-M. Xu and P.-T. Chuang, *Genes Dev.*, 2004, **18**, 641-659.
42. J. A. Porter, K. E. Young and P. A. Beachy, *Science*, 1996, **274**, 255-259.

43. R. K. Mann and P. A. Beachy, *BBA*, 2000, **1529**, 188-202.
44. J. Li, Z. Cui, S. Zhao and R. L. Sidman, *Stem Cells*, 2007, **25**, 2864-2873.
45. G. Wang, J. Silva, K. Krishnamurthy, E. Tran, B. G. Condie and E. Bieberich, *J. Biol. Chem.*, 2005, **280**, 26415-26424.
46. W. F. O. Marasas, R. T. Riley, K. A. Hendricks, V. L. Stevens, T. W. Sadler, J. Gelineau-van Waes, S. A. Missmer, J. Cabrera, O. Torres, W. C. A. Gelderblom, J. Allegood, C. Martinez, J. Maddox, J. D. Miller, L. Starr, M. C. Sullards, A. V. Roman, K. A. Voss, E. Wang and A. H. Merrill, Jr., *J. Nutr.*, 2004, **134**, 711-716.
47. G. Wang, K. Krishnamurthy, Y.-W. Chiang, S. Dasgupta and E. Bieberich, *J. Neurochem.*, 2008, **106**, 718-733.
48. R. J. Swain, S. J. Kemp, P. Goldstraw, T. D. Tetley and M. M. Stevens, *Biophys J.*, 2010, **98**, 1703-1711.
49. J. Y. Liu, H. F. Peng, S. Gopinath, J. Tian and S. T. Andreadis, *Tissue Eng.*, 2010, **16**, 2553-2564.
50. R. Morris and C. Potten, *J Invest Dermatol*, 1999, **112**, 470-475.
51. C. A. B. Jahoda and A. J. Reynolds, *Lancet*, 2001, **358**, 1445-1448.
52. M. J. Walsh, T. G. Fellous, A. Hammiche, W.-R. Lin, N. J. Fullwood, O. Grude, F. Bahrami, J. M. Nicholson, M. Cotte, J. Susini, H. M. Pollock, M. Brittan, P. L. Martin-Hirsch, M. R. Alison and F. L. Martin, *Stem Cells*, 2008, **26**, 108-118.
53. D. A. Moss, M. Keese and R. Pepperkok, *Vib Spectrosc*, 2005, **38**, 185-191.
54. A. Y. Lau, L. P. Lee and J. W. Chan, *Lab Chip*, 2008, **8**, 1116-1120.
55. W. E. Huang, A. D. Ward and A. S. Whiteley, *Environ Microbiol Rep*, 2009, **1**, 44-49.

Chapter 8

Perspective work – confocal Raman imaging reveals novel information on lipid polarisation in hair follicle epithelial progenitor cells



8.1 Abstract

Raman mapping of cells at high spatial resolution can reveal valuable information on a subcellular level. Following our success in differentiating epithelial progenitor cells (epiPCs) from outer root sheath (ORS) cells by noting their increased total lipid concentration and decreased protein concentration, Raman mapping was applied to primary human hair follicle cytokeratin 15 (K15)+ epiPCs and ORS cells. Differences in the distribution of lipids in the cells were investigated. The preliminary data presented in this chapter gives evidence to lipid polarisation in K15+ epiPCs but not in ORS cells. It has been shown in Chapter 6 that some epiPCs differentiated into transient amplifying (TA) cells while being grown on the CaF₂ substrate. It is postulated that the lipid polarisation observed is linked to the migratory phenotype of TA cells. Though more evidence needs to be collected in order to verify this hypothesis, the preliminary data shed light on the possible linkage between lipid polarisation and the migratory function of human hair follicle epithelial TA cells.

8.2 Introduction

In previous chapters, the application of Fourier transform infrared (FTIR) spectroscopy to hair follicle epiPCs and ORS cells resulted in the elucidation of differences in the overall levels of FAs. This difference was also found between mesenchymal cell types within the lower hair follicle. To continue the lipodomic investigation of hair follicle stem cells using vibrational spectroscopy, Raman mapping was applied to isolated hair follicle K15+ epiPCs and ORS cells. The difference in lipid distribution between the cell types was investigated.

Raman spectroscopy coupled to a confocal microscopy offers far superior spatial resolution (about 0.5 μm , depending on the excitation wavelength and numerical aperture (NA) of the objective lens). Raman spectroscopy can therefore offer information on a subcellular level, revealing variations in chemical composition as well as distribution within cells.

The lipid polarisation phenomenon is of particular interest, since it has been found to be associated with the migratory function of certain cell types. Coincidentally, epiPCs are known to differentiate into TA daughter cells with higher migratory rates¹, which subsequently differentiate into mature epithelial cells. As shown in Chapter 6, primary human hair follicle K15+ epiPCs differentiate into TA cells and ORS cells while maintaining a progenitor cell pool, after being seeded on Raman compatible substrates. It is of interest whether lipid polarisation may be detected in K15+ epiPCs or TA cells.

Polarisation refers to the asymmetric distribution of cell components in the cell². Lipid rafts, for example, which are cholesterol- and sphingolipid-rich clusters in the cell membrane, were found to play important roles in the governance of the migration of stem cells^{3,4,5}. During haematopoietic stem cell (HSC) / haematopoietic progenitor cell (HPC) migration, HSC/HPCs become polarised and acquire a morphology with a leading edge, and an uropod on the opposite edge⁶. CD133, a lipid raft protein, was found to accumulate in the uropod co-localised with other uropod- and adhesion-related markers. The results indicate that CD133 is likely to be involved in the polarity and migratory activities in HSC/HPCs⁶. By contrast, CD133 was found to be spread over non-migratory HSC/HPCs⁶.

Non-uniform distribution of lipids was also demonstrated to be a major factor in the establishment and maintenance of directional migration of T lymphocytes^{2,7}. Gangliosides are another type of lipid raft associated protein. Gangliosides enriched lipid raft domains were found to localise on the leading edge and the uropod of migratory T lymphocytes; the type of ganglioside was, furthermore, found to differ at the two ends². Disrupting the plasma membrane organisation by cholesterol depletion, and subsequently preventing the formation of lipid rafts polarisation, was found to impede the migration of T lymphocytes as well as chemokine-induced chemotaxis².

Similar to hair follicle epiPCs, epiSCs found in the basal layer of the interfollicular epidermis⁸⁻¹¹ give rise to TA daughter cells that are more proliferative and migratory⁹. Double-labelling of lipid raft-associated ganglioside and epiSC markers revealed that, ganglioside expression was many folds higher in TA cells than in epiSCs, both *in vivo* and *in vitro*¹². Moreover, ganglioside expression was linked to higher proliferative rates¹², a characteristic of the TA cells. The results are indicative of the role of lipid rafts in the proliferation of TA cells - direct descendants of the epiSCs.

This chapter presents the preliminary data from the application of Raman spectroscopy to isolated hair follicle epiPCs and ORS cells (as seen in Chapter 6). The Raman maps collected from isolated hair follicle epiPCs and ORS cells revealed novel information on the lipid polarisation in epiPCs.

8.3 Materials and methods

8.3.1 Hair follicle K15+ epiPCs and ORS cells isolation

The methods were the same as described in Chapter 6 and in ref¹³.

8.3.2 Raman maps collection

A Raman spectrometer coupled to a confocal microscope (WITec, Ulm, Germany) was employed for mapping the isolated hair follicle K15+ epiPCs and ORS cells. The Raman scatter was induced by 514 nm laser. Using a 20× NA 0.4 objective, the spatial resolution was approximately 500 nm; the spectral resolution was 4 cm⁻¹.

8.3.3 Raman map processing: Chemical images of the Raman maps of an ORS cell and a K15+ epiPC chemical images were plotted using CytoSpec© (www.cytospec.com), based on the ratio of ($I_{2770-3110\text{ cm}^{-1}}/I_{1205-1290\text{ cm}^{-1}}$).

8.4 Results

Chemical images were plotted based on the ratio of the integral of the Raman bands for C-H stretching vibration modes of fatty acids (FAs)/ lipids (2770-3110 cm⁻¹) over the integral of the Raman band for amide III (1205-1290 cm⁻¹), showing the distribution of lipids high protein poor regions (Fig. 1a-d). Three of the Raman maps successfully collected from K15+ epiPCs show that the distribution of lipids in the K15+ epiPCs are skewed (Fig. 1a-c), whereas the Raman map successfully collected from ORS cells show that the distribution of lipids in the cells is uniform (Fig. 1d).

Two of the K15+ epiPCs, which were smaller in size, display more skewed lipid polarisation (Fig. 1a,b) than the K15+ epiPC that was larger in size (Fig. 1c). In Figures 1a and 1b the distribution of lipids in the K15+ epiPCs is more concentrated on one end of the cell, forming a 'crescent shape'. In Figure 1c, the distribution of lipids in the K15+ epiPC is non-uniform, but does not display a trend of concentrating to any particular side. The distribution of lipids in the ORS cell assumed a more uniform distribution compared to the K15+ epiPCs (Fig.1d).

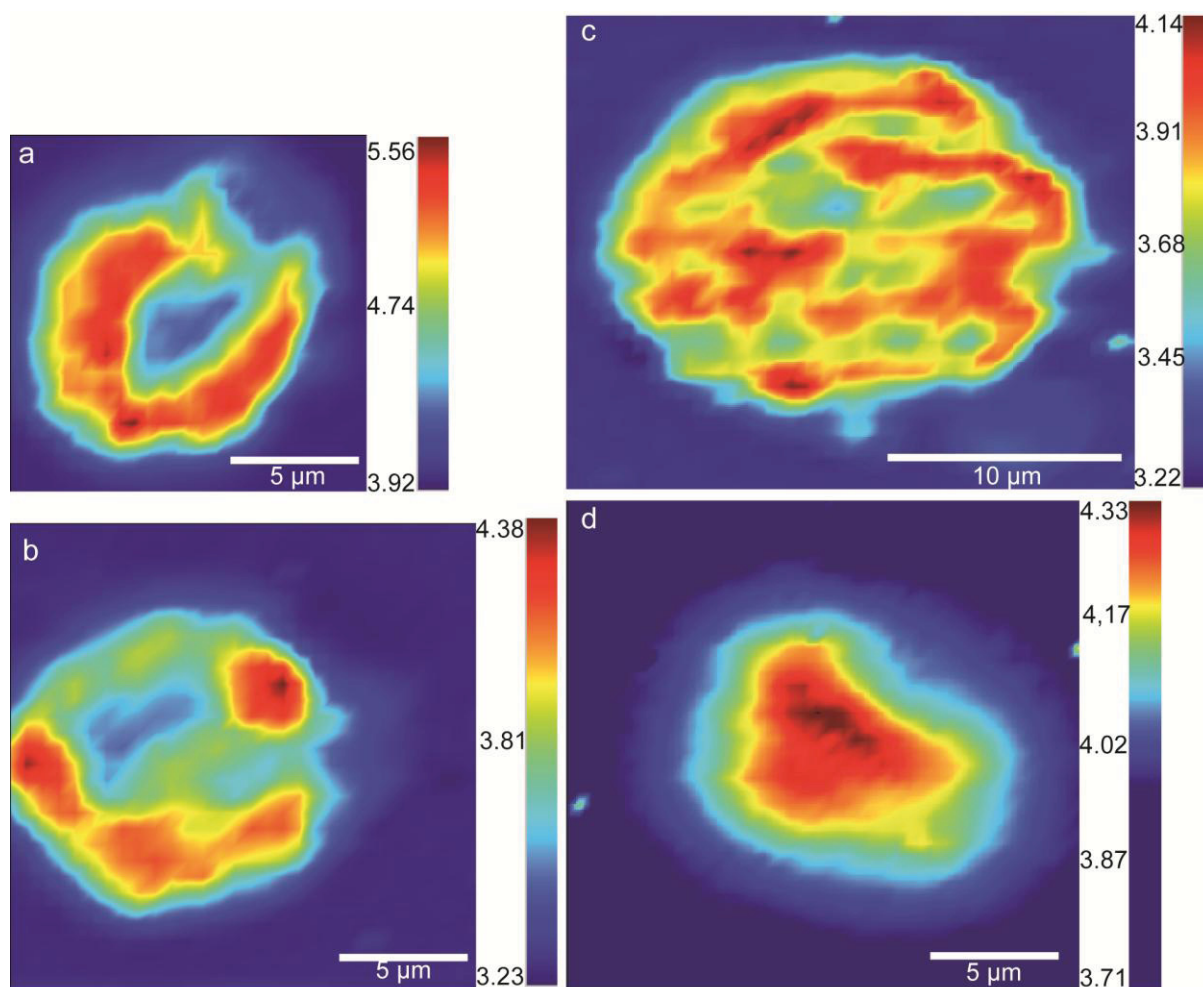


Figure 1a-d show chemical images from Raman maps of cells isolated from a human hair follicle, plotted based on the ratio of the integral of the Raman bands at $2770\text{-}3110\text{ cm}^{-1}$, over the Raman band(s) at $1205\text{-}1290\text{ cm}^{-1}$. 1a-c are maps collected from K15+ epiPCs while 1d is a map collected from an ORS cell.

8.5 Discussion

As the number of Raman images successfully collected from the hair follicle epithelial cells was limited, it is not possible to draw a conclusion whether lipid polarisation is a feature exclusive to cells in the K15+ epiPCs population. However, the images suggest that the lipid distribution in K15+ epiPCs tend to be non-uniform, and in two maps there appears to be polarisation of lipids in the cells, while in the ORS cell lipid is evenly distributed.

This hypothesis requires further investigation; Raman maps from a larger number of K15+ epiPCs and ORS cells need to be collected, in order to confirm whether lipid indeed tends to be polarised only on epiPCs.

As it is known that, after isolation from the hair follicle, human hair follicle epiPCs may differentiate into TA cells that are more motile. At the same time, polarisation of cellular components, such as proteins and lipids, is required for many cell types to be activated and to acquire a motile phenotype. The skewed distribution of lipids in the cell may therefore be a feature linked to the more migratory TA cells, while the uniform distribution of lipids of ORS cells indicates that the cell is of a more mature, settled and differentiated cell type.

Careful consideration should be taken into account that the polarisation of lipid rafts is a phenomenon detected in the cell membrane, which has a curvature. By contrast, the Raman maps presented in this study were acquired over a plane; hence they show the distribution of lipids-rich components across a section of the cells, likely to be cytosolic. While evidence in there is limited literature to directly support that such cytosolic polarisation exists, the Raman maps provide novel insight and food for thought.

It must also be noted that, the formation of holoclones had been recorded for K15+ epiPCs *in vitro*¹⁴, indicating that after being plated on the Raman substrate, some of the K15+ epiPCs were likely to differentiate into TA cells and subsequently more mature cell types.

Further studies aim to clarify the relationship between lipid polarisation and migratory phenotype of hair follicle epiPCs, should incorporate a higher number of K15+ epiPCs and ORS cells, and employ immunostaining techniques. Using antibodies specific for different stages of hair follicle epithelial cells, such as K15, CD200 for epiPCs^{15, 16}, and K6 for differentiated ORS cells, would provide an indication of the stages at which the cells are, prior to Raman imaging. As described in Chapter 7, it is possible to perform Raman spectroscopic studies on fluorescent labelled cells, as long as the excitation and emission wavelengths of the fluorophore employed does not overlap with the source of laser wavelength for inducing Raman scattering.

8.6 Conclusion

Although still at a preliminary stage of investigation, Raman maps of K15+ epiPCs and ORS cells unveiled the potential correlation between polarised lipid distributions and migratory phenotypes of TA cells. Further investigation is required to clarify whether there is a link between the phenotypes. Repeating the Raman mapping exercise on a larger number of cells, which have been immunostained with markers specific for their stages, would no doubt shed light on this fascinating phenomenon and open up a whole new realm of research.

References:

1. C. Roh, Tao, Q., Photopoulous, C. and Lyle, S, *J Invest Dermatol*, 2005, **125**, 1099-1105.
2. C. Gomez-Mouton, J. L. Abad, E. Mira, R. A. Lacalle, E. Gallardo, S. Jimenez-Baranda, I. Illa, A. Bernad, S. Manes and C. Martinez-A, *PNAS*, 2001, **98**, 9642-9647.
3. S. Yamazaki, A. Iwama, S.-i. Takayanagi, Y. Morita, K. Eto, H. Ema and H. Nakauchi, *EMBO J*, 2006, **25**, 3515-3523.
4. S. Yamazaki, A. Iwama, Y. Morita, K. Eto, H. Ema and H. Nakauchi, *Ann NY Acad Sci*, 2007, **1106**, 54-63.
5. M. Y. Lee, J. M. Ryu, S. H. Lee, J. H. Park and H. J. Han, *J Lipid Res.*, 2010, **51**, 2082-2089.
6. B. Giebel, D. Corbeil, J. Beckmann, J. Hoehn, D. Freund, K. Giesen, J. Fischer, G. Koegler and P. Wernet, *Blood*, 2004, **104**, 2332-2338.
7. L. M. Pierini and F. R. Maxfield, *PNAS*, 2001, **98**, 9471-9473.
8. C. Potten and R. Morris, *J Cell Sci Suppl.*, 1988, **10**, 45-62.
9. L. Liang and J. Bickenbach, *Stem cells*, 2002, **20**, 21-31.
10. F. Watt, M., *Phil. Trans. R. Soc. Lond. B*, 1998, **353**, 831-837.
11. C. Blanpain and E. Fuchs, *Nat Rev Mol Cell Biol*, 2009, **10**, 207-217.
12. R. Gniadecki and B. Bang, *J Invest Dermatol*, 2003, **121**, 522-528.
13. K. Lau, R. Paus, S. Tiede, P. Day and A. Bayat, *Exp Dermatol*, 2009, **18**, 921-933.
14. S. Tiede, N. Koop, J. E. Klopper, R. Fassler and R. Paus, *Stem Cells*, 2009, **27**, 2793-2803.
15. J. E. Klopper, S. Tiede, J. Brinckmann, D. P. Reinhardt, R. Faessler and R. Paus, *Exp Dermatol.*, 2008, **17**, 592-609.
16. M. Ohyama, A. Terunuma, C. L. Tock, M. F. Radonovich, C. A. Pise-Masison, S. B. Hopping, J. N. Brady, M. C. Udey and J. C. Vogel, *J. Clin. Invest.*, 2006, **116**, 249-260.

Chapter 9

Summary, conclusion and outlook

9.1 Importance of developing a reliable stem cell identification modality

Stem cell research, tissue engineering and translational medicine, have taken centre stage in biomedical research^{1,2}. Promises of utilising stem cells as part of treatments are being shown^{3,4}, and the development of treatments is being taken from bench to bed⁵. Success stories of stem cell treatments are aplenty, though caution still needs to be taken. With each new type of stem cells being employed for a therapy, thorough investigation is of paramount importance. To gain understanding of a stem cell type, and its interaction with its recipient environment, the ability to purify and enrich the stem cell type is crucial.

Widely accepted cell sorting methods, such as fluorescent activated cell sorting (FACS) and magnetic activated cell sorting (MACS), rely on surface markers specific to the cell lineage. In FACS, fluorescent labels conjugated to antibodies are typically used for cell lineage recognition, while MACS utilises magnetic beads conjugated to antibodies. Although antibody based cell sorting methods have their advantages, there are also numerous disadvantages. Adult stem cells (ASCs) such as mesenchymal stem cells (MSCs), require a cocktail of markers to be sorted confidently. This leads not only to lengthy protocol optimisation and laborious labelling procedures, but also to complication with the overlapping of fluorescence bands in the electromagnetic wave spectrum. Setting tight parameters for fluorescence wavelengths threshold inevitably results in cell loss. Cell loss should ideally be avoided especially for stem cells with limited abundance. Furthermore, the identification of lineage specific markers is a time consuming process, making it difficult to isolate ASCs based on surface markers.

Vibrational spectroscopy can provide a full range of information on the structural and chemical composition of samples. As empirical evidence increases, growing enthusiasm is being injected in the use of vibrational spectroscopy to identify stem cells.

9.2 Need for label free identification of hair follicle stem cells

The hair follicle is a highly dynamic organ in the skin⁶. It hosts a myriad of ASCs^{7,8}, such as epithelial progenitor cells (epiPCs), melanocyte stem cells, MSCs and skin derived progenitors capable of differentiating into neuronal lineages^{9,10}. Particular interests have been placed on human hair follicle epiPCs and MSCs in this thesis, since both of these cell types are known to participate in cutaneous wound healing⁸. They are also highly clonogenic *in vitro* and therefore have huge potentials for tissue engineering and translational medicine.

Another main reason for applying vibrational spectroscopy to human hair follicle MSCs, stems from the fact that specific surface markers for MSCs are lacking. This results in great obstacles in obtaining pure MSCs from the human hair follicle. Compared to the well characterised human hair follicle epiPCs, with successfully identified specific surface markers^{11, 12}, human hair follicle MSCs are in dire need of further characterisation.

9.3 Feasibility of using FTIR spectroscopy to discern hair follicle tissue compartments proven

Hair follicle contains clearly defined tissue compartments, identifiable by trained personnel. Spectral variations between biological species are often subtle. Chemometric analyses are thus typically employed to uncover the subtle spectral variations. Before applying vibrational spectroscopic techniques to single cells in the hair follicle, proof of principle studies were carried out. Fourier transform infrared (FTIR) mapping was applied to lower human hair follicles in scalp skin section to show that tissue compartments can be differentiated and characterised by FTIR spectroscopy, purely based on their spectral variations.

In our proof of principal study, N-FINDR spectral unmixing algorithm was applied to the FTIR spectra in the maps. The tissue types within the hair follicle were successfully discerned. N-FINDR finds the purest spectra (endmembers) in the data set, then expresses all the spectra as a linear combination of the endmembers. The result of N-FINDR was pseudo-colour maps, which present the spatial distribution of the endmembers.

N-FINDR was deemed a suitable method for the study. N-FINDR expresses each spectrum in the map as a linear combination of endmembers. It allows the overlapping of endmembers, and results in 'transitional zones' between tissue compartments. One may argue that these transitional zones are not succinct in the bright field images. However, since the aperture size allowing infrared (IR) radiation through was 15-20 μm , some spectra were inevitably obtained across hair follicle tissue layers. Overlaps of endmembers in the pseudo colour maps must therefore be true representation of the data.

The assignment of endmembers to tissue layers was based not only on the locality of the endmembers, but also on the level of correlation of spectral features of the endmembers to known biological information of the tissue layers. According to published immunostaining data in the literature collagen is abundant in the hair follicle mesenchyme^{13, 14}. Collagen was clearly detected in the FTIR spectra of endmembers corresponding to connective tissue

sheath (CTS) and dermal papilla (DP). Endmembers corresponding to the CTS were found to contain higher levels of total lipids than the DP. These observed spectral features are also well supported by the published knowledge of the hair follicle biology. For instance, pre-adipocytes were shown to be found around the hair follicle during embryonic development, and the hair follicle CTS is believed to continue to supply adipocytes to the surrounding dermis and subcutis (SC), well into adulthood¹⁵.

9.4 A classifier trained specifically to identify hair follicle tissue types

Another approach of developing FTIR spectroscopy as a tool for identifying tissue and cell types in the human hair follicle was implemented. A support vector machine (SVM; a classifier) was trained on single FTIR spectra collected from the clearly defined hair follicle tissue compartments. Each chosen tissue compartment was assigned as a 'class'. The SVM identified the most representative IR features for each class, and used them for classifying unknown spectra into their respective classes. The means spectra of the training set of each class displayed spectral features similar to the corresponding endmembers in the previous work, which utilised N-FINDR (Chapter 3). For example, the means spectrum of the class CTS (Chapter 4), and the endmembers corresponding to CTS (Chapter 3), displayed an abundance of lipids, proteins and collagen. This affirms that our assignment of endmembers to their respective hair follicle tissue layers was correct.

Verification of the SVM was carried out on a FTIR map collected from a hair follicle by focal plane array (FPA)-FTIR. A pseudo colour map was constructed by classifying spectra with the SVM and assigning a colour to each class. As the pseudo colour map greatly resembled the white light image of the hair follicle, with respect to compartment identification, the experiment was deemed successful.

The significance of building a SVM specific to the hair follicle tissue compartments comes in two layers. Firstly, the SVM can produce images detailing classes. Overlaying SVM images over white light images can provide a visual guide of tissue compartments to non-hair follicle experts. Secondly, it shows the potential of building a SVM that can classify single cell spectra. Training a classifier based on single cell spectra of different cell types from the hair follicle (stem and non-stem cells), potentially enables the identification and tracking of hair follicle stem cells in tissues. Given the roles of hair follicle stem cells in wound healing, it is envisaged hair follicle stem cells in wound healing can be investigated using FTIR and SVM *sans* labelling.

9.5 Elucidation of lipid features detectable by FTIR spectroscopy in DP cells

Utilising vibrational spectroscopy to identify MSCs in the hair follicle was a major aim of this project. A simple way to realise the aim would be to establish ‘signature spectra’ of MSCs against differentiated mesenchymal cells. However, due to the lack of specific markers, isolating pure MSCs was not an option. Furthermore, unlike epiPCs, MSCs do not cluster in a specifically defined niche. They are non-uniformly distributed in the DP and along the CTS. The positions of MSCs within a hair follicle could therefore not be assumed by anatomical positions. We employed FTIR mapping of the DP as a strategy, since MSCs are known to be located in the DP^{16, 17}. It was decided that, spectral features within the DP would be analysed, and the extracted features would be compared to the current published knowledge of stem cells.

As the size of the spindle shaped fibroblast cell in the DP is estimated to be approximately 5 μm wide and approximately 10 μm in length, and the spatial resolution in FTIR spectroscopy is wavelength dependent (ranging from 3 to 10 μm)¹⁸, focus was placed on the higher wavenumber region of the mid-IR spectrum. This region contains IR absorption bands attributed to C-H stretching modes of acyl chains, attributed to fatty acids (FAs), lipids and proteins in the sample. By applying unsupervised hierarchical clustering analysis (UHCA) on the FTIR map of the DP, several clusters were derived.

Three main types of spectral variations in the average spectra, which are pertinent to lipid and protein, were considered: 1) level of total lipids, 2) lipid to protein ratio, and 3) shifts in wavenumbers of the C-H stretching peaks. The level of total lipids conceivably indicates presence of lipid reserve, which ASCs require when cues to differentiation and proliferation were received. The lipid to protein ratio reflects the level of transcriptional activities in the cells, which is believed to be lower in quiescent stem cells than the more metabolically active differentiated cells. Shifts in wavenumbers of C-H peaks indicate specific cell membrane fluidity, which is believed to be lower in stem cells¹⁹. Evaluating the detectable lipid features in the FTIR spectra of the DP cells provided guidance for spectral features to focus in the following studies.

9.6 Establishment of FTIR spectral markers for human hair follicle K15+ epiPCs

The journey towards identifying human hair follicle MSCs by FTIR spectroscopy progressed by borrowing a leaf from their neighbours in the outer root sheath (ORS). The extraction of

human hair follicle epiPCs had become feasible, by engineering *cytokeratin 15 (K15)*-promoter driven green fluorescent protein (GFP) expression and toxin resistance into epiPCs²⁰. FTIR spectroscopy was applied to primary K15+ epiPCs and non-bulge ORS cells in order to establish spectral differences. Single spectra were collected from these cells, which had been grown on quartz and CaF₂ substrates. The spectra were analysed using UHCA and principal component analysis (PCA). In both circumstances, K15+ epiPCs were found to contain higher lipid concentration and lower protein concentration than the ORS cells. Using increased total lipids and decreased protein contents as criteria for recognising K15+ epiPCs, FPA-FTIR imaging was applied to a human hair follicle in a skin section, which contained the bulge – the K15+ epiPCs niche. By applying UHCA, a spectral cluster which fit the K15+ epiPC criteria was identified within the bulge. Its location coincided with published K15 immuno-staining results¹¹ – the lower (distal) bulge. It also contained higher concentration of total lipids and lower protein concentration. It was thus highly conceivable that, the increased lipid level and the decreased protein level, could be used as stem cell recognition criteria, at least in the human hair follicle.

9.7 Identifying MSCs in the human hair follicle using FTIR spectroscopy

Although MSCs and epiPCs are expected to behave differently (since they are of different embryonic lineages), they are likely to possess more similar characteristics during differentiation to each other, than to ASCs of other organs. Therefore, the criteria learnt from the epiPCs were applied to human hair follicle MSCs.

Human hair follicle bulbs were FTIR imaged using a FPA detector, an area of 350 $\mu\text{m} \times 350 \mu\text{m}$ with each pixel corresponding to an area of 5.5 $\mu\text{m} \times 5.5 \mu\text{m}$. In each map, UHCA isolated a cluster that could be found in both DP and CTS, which simultaneously displayed the highest concentration of lipids among the mesenchymal clusters. These clusters also had lower protein concentration than the other clusters. Further corroboration with the pattern of nestin immunoreactivity, as seen on the adjacent skin section, supported the notion that FTIR spectroscopy and UHCA successfully identified and located MSCs within the human hair follicle.

9.8 Paving way for human hair follicle MSC identification with Raman spectroscopy

The story of developing FTIR spectroscopy as a hair follicle stem cell identification tool has involved fixed samples thus far. To enable the use of vibrational spectroscopy as a modality

for sorting hair follicle stem cells from non-stem cells for clinical use, studies on live hair follicle cells will be necessary. Since FTIR spectra of cells in media can be affected by water bands, which overlap with biological IR absorption bands, FTIR spectroscopy is not ideal for analysing live cells. Although Synchrotron (SR)-FTIR has been successfully applied to studying live cells^{21, 22}, access to SR-FTIR facilities is often limited. Thus SR-FTIR is unlikely to become a widely adopted tool for sorting hair follicle stem cells. The preliminary success in identifying hair follicle stem cells using FTIR spectroscopy nevertheless shows the potentials of vibrational spectroscopy as a cell sorting tool. As the water band in Raman spectra of biological samples does not obscure the Raman bands containing biochemical information, Raman is ideal for live cells analysis²³.

To realise the use of vibrational spectroscopy as a hair follicle stem cells sorting technique, Raman signatures of the said cell types need to be established. To confidently acquire Raman spectra from the right cells, immunostaining can be employed to show their locality. Fluorescence is known to overwhelm the Raman spectrum, masking the naturally much weaker Raman signals. However, we showed that Raman spectra with minimal fluorescence background can be collected from skin sections, which were stained with antibodies conjugated to a blue fluorochrome (e.g. DyLight 350). By using a Raman excitation source with a visible wavelength (e.g. 514 nm) outside the fluorescence excitation range, Raman scattering was induced without exciting the fluorochrome. There is however a short coming: the conjugation of an antibody to the cell may alter the Raman spectra. Moreover, hair follicle MSCs lack specific markers. Though nestin expression can be used to shed light on their locality, it must be noted that not all nestin expressing cells in the human hair follicle mesenchyme are MSCs.

FPA-FTIR enables thousands of spectra to be taken over several hundred micrometres within minutes. A viable strategy is therefore to utilise FTIR spectroscopy for providing an overview of the tissue, and point out the locations of epiPCs and MSCs in the hair follicle *in situ*.

Raman mapping can be performed at subcellular resolution on stem cell-containing areas of the sample skin section, apply UHCA, and acquire average Raman spectra from the stem cell cluster as a fingerprint. To demonstrate the feasibility of this strategy, a Raman map was collected from the CTS of a hair follicle in a skin section. UHCA successfully separated the cell spectra from the extracellular matrix (ECM) spectra. This experiment has therefore shown the potential of establishing fingerprint spectra of hair follicle stem cells by Raman mapping.

9.9 Raman mapping revealed lipid polarisation in single K15+ epiPCs but not in ORS cells

Other than establishing signatures for cells, Raman spectroscopy has also been increasingly adopted for revealing chemical and structural information on a subcellular level^{23,24}, because of the high spatial resolution it can offer. Primary K15+ epiPCs and ORS cells seeded on CaF₂ substrates were Raman mapped using a 514 nm laser source at about 700 nm step size. Plotting Raman images based on the ratio of based on the ratio of $I_{2770-3110\text{ cm}^{-1}}/I_{1205-1290\text{ cm}^{-1}}$ (C-H stretching bands attributed to FAs over the amide III band from protein), enabled the visualisation of lipid domains distribution in the cytoplasm. Uneven distribution of lipid was observed in K15+ epiPCs but not in ORS cell, giving evidence to polarisation in cells from the K15+ epiPCs population. It was unclear whether the lipid polarisation was recorded in epiPCs or transient amplifying (TA) cells. However, since TA cells are known to be migratory and lipid polarisation has been linked to the migratory phenotype, lipid polarisation was postulated to be a TA cell feature. Although further analysis is required to clarify, Raman mapping has provided the first hint to this plausible linkage. Raman mapping combined with lineage markers for hair follicle epithelial cells such as K15, K6 and CD200 will most certainly provide an answer.

9.10 Conclusion and outlook

FTIR spectroscopy has been successfully applied to distinguishing stem cells from differentiated cells within the human hair follicle in a label-free and minimally destructive manner. This work has provided a novel solution to identifying MSCs within the hair follicle without labelling. The obstacle of not being able to isolate pure MSCs from the hair follicle due to the lack of specific markers was overcome. Our approach to solving the problem consisted of these steps:

- demonstrate FTIR spectroscopy and mapping, together with chemometric tools e.g. N-FINDR, SVM, UHCA and PCA, as a viable tool for differentiating tissue types within the hair follicle;
- interpret the IR features based on current knowledge on stem cells;
- learn the distinctive IR features of hair follicle epiPCs which can be isolated by genetic manipulation;

- correlate FTIR imaging with anti-nestin immuno-staining and establish spectral features to distinguish MSCs from their neighbouring mesenchymal cells.

By systematically approaching this challenge, we have produced convincing empirical evidence to show that FTIR spectroscopy imaging can identify and locate MSCs and epiPCs within the hair follicle. This study has therefore successfully shown the potentials of using vibrational spectroscopy to sort hair follicle stem cells.

FTIR imaging, especially when coupled to a FPA detector, can provide a rapid overview for a large sample area. Using the hair follicle stem cell IR features we recently identified, the locations of the MSCs and epiPCs within the hair follicle can be visualised without staining. However, FTIR spectroscopy is unlikely to be adopted as a cell sorting technique, since water IR signals in the cell medium would perturb biological signals in the IR spectrum. We foresee that a vibrational spectroscopy based cell sorting tool will be based on Raman spectroscopy. Raman signature of human hair follicle MSCs and epiPCs would first need to be established. We showed that Raman mapping of the hair follicle CTS combined with UHCA successfully separated cell spectra from the ECM spectra. It is therefore conceivable that Raman mapping will allow MSC and epiPC Raman fingerprint to be established. To be certain the Raman spectra are acquired from the stem cells, FTIR imaging in combination with UHCA can indicate the locations of the stem cells without adding extra labels. The results may be verified by immunostaining. Finally, live cells dissociated from the human hair follicle should be analysed and sorted according to their Raman signature. Of course, the ultimate proof that vibrational spectroscopy can be applied to sorting live hair follicle stem cells is needed. The ultimate proof can be provided by showing these cells possess stem cell properties *in vitro*, i.e. proliferate indefinitely, undergo asymmetric differentiation, and can differentiate into multiple cell types. This work has paved the way towards a label-free non-invasive vibrational spectroscopy based modality for sorting hair follicle MSCs and epiPCs, which have huge potentials in regenerative medicine and tissue engineering.

Last but not least, this study has also shown Raman spectroscopy can reveal novel information of epiPCs. The irregular distribution of lipid in the cells within the K15+ epiPCs population suggests lipid polarisation, which may be linked to the migratory phenotype of hair follicle epithelial TA cells. This work will need further verification by analysing a larger number of cells, and verify their identity by immunofluorescence staining. Raman mapping

of hair follicle stem cells will undoubtedly unveil further novel chemical and structural information on a subcellular level.

References:

1. C.-M. Chuong, G. Cotsarelis and K. Stenn, *J Invest Dermatol*, 2007, **127**, 2098-2100.
2. S. Levenberg, N. Huang, E. Lavik, A. Rogers, J. Itskovitz-Eldor and R. Langer, *PNAS*, 2003, **100**, 12741-12746.
3. L. Wang, J. Deng, G. Li, J. Wang, B. Xiang, T. Kashour, R. Arora, M. Gruwel, M. Glogowski, B. Tomanek, R. Deslauriers and G. Tian, *J Mol Cell Cardiol*, 2007, **42**, S88-S101.
4. A. Stoff, A. Rivera, N. Banerjee, S. Moore, T. Numnum, A. Espinosa-de-los-Monteros, D. Richter, G. Siegal, L. Chow, D. Feldman, L. Vasconez, J. Mathis, M. Stoff-Khalili and D. Curiel, *Exp Dermatol*, 2008, **18**, 362-369.
5. H. A. Navsaria, N. O. Ojeh, N. Moiemem, M. A. Griffiths and J. D. Frame, *Plastic Reconstr Surg*, 2002, **113**, 978-981.
6. M. R. Schneider, R. Schmidt-Ullrich and R. Paus, *Curr Biol*, 2009, **19**, R132-R142.
7. S. Tiede, J. Kloepper, E. Bodo, S. Tiwari, C. Kruse and R. Paus, *Europe J Cell Biol*, 2007, **86**, 355-376.
8. K. Lau, R. Paus, S. Tiede, P. Day and A. Bayat, *Exp Dermatol*, 2009, **18**, 921-933.
9. J. G. Toma, McKenzie, I.A., Bagli, D., Miller, F.D., *Stem Cells*, 2005, **23**, 727-737.
10. J. G. Toma, M. Akhavan, K. J. L. Fernandes, F. Barnabé-Heider, A. Sadikot, D. R. Kaplan and F. D. Miller, *Nat Cell Biol*, 2001, **3**, 778-784.
11. J. E. Kloepper, S. Tiede, J. Brinckmann, D. P. Reinhardt, R. Faessler and R. Paus, *Exp Dermatol*, 2008, **17**, 592-609.
12. M. Ohyama, A. Terunuma, C. L. Tock, M. F. Radonovich, C. A. Pise-Masison, S. B. Hopping, J. N. Brady, M. C. Udey and J. C. Vogel, *J. Clin. Invest.*, 2006, **116**, 249-260.
13. J. Couchman and T. Walter, *Dev Biol*, 1984, **108**, 290-298.
14. A. Messenger, K. Elliott, A. Temple and V. Randall, *J Invest Dermatol*, 1991, **96**, 93-97.
15. K. Wojciechowicz, E. Markiewicz and C. Jahoda, *Exp Dermatol*, 2008, **17**, 675-680.
16. G. Richardson, E. Arnott, C. Whitehouse, C. Lawrence, A. Reynolds, N. Hole and C. Jahoda, *J Invest Dermatol Symp Proc*, 2005, **10**, 180-183.
17. C. A. B. Jahoda, C. J. Whitehouse, A. J. Reynolds and N. Hole, in *Exp Dermatol*, 2003, **12**, 849-859.
18. P. Lasch and D. Naumann, *BBA*, 2006, **1758**, 814-829.
19. J. Li, Z. Cui, S. Zhao and R. L. Sidman, *Stem Cells*, 2007, **25**, 2864-2873.
20. S. Tiede, N. Koop, J. E. Kloepper, R. Fassler and R. Paus, *Stem Cells*, 2009, **27**, 2793-2803.
21. H.-Y. N. Holman, K. A. Bjornstad, M. P. McNamara, M. C. Martin, W. R. McKinney and E. A. Blakely, *J Biomed Optics*, 2002, **7**, 417-424.
22. H. Y. N. Holman, M. C. Martin and W. R. McKinney, *J Biol Phy*, 2003, **29**, 275-286.
23. F. C. Pascut, H. T. Goh, N. Welch, L. D. Buttery, C. Denning and I. Notingher, *Biophys. J.*, 2011, **100**, 251-259.
24. E. Zuser, T. Chernenko, J. Newmark, M. Miljkovic and M. Diem, *Analyst*, 2010, **135**, 3030-3033

Acknowledgements

I would like to thank my PhD supervisor, Dr. Volker Deckert, for his patience, his continuous support and mentoring. Through Volker's supervision, I have gained a myriad of valuable skills and developed traits that will certainly benefit my scientific career in the years to come.

Dr. Bayden Wood is the second person I would like to thank. Bayden has introduced me to FTIR spectroscopy, given me enormous support throughout my PhD and continually given me sunshine all the way from Australia.

I am grateful to Prof. Ralf Paus for providing a great topic for me to research on, and his supervision and training. His enthusiasm in hair biology is contagious and I am so glad to have been drawn into this field.

From Ralf's group, I would particularly like to thank Dr. Jennifer Kloepper and Dr. Stephan Tiede, without whom I would not have been able to complete my research. Jenny and Stephan provided me with great training on histology and immunocytochemistry at the beginning of my PhD. Throughout the rest of my PhD, they had been great collaborators – always eager to give feedback and supply samples.

I would also like to thank my colleagues and former colleagues in Dortmund and Jena. Dr. Melissa Mariani, in particular, had been an important part of my PhD life. I am grateful to have had Melissa's presence in the office and her valuable and continuous feedback as a colleague.

I would like to acknowledge Dr. Martin Hedegaard for expanding my chemometrics knowledge and helping me tackle a lot of the data analysis issues.

I must also thank other colleagues and collaborators who have given me help and or guidance throughout my PhD, and they are in no particular order: Dr. Christian Matthaeus, Dr. Michael Heise, Dr. Philip Heraud, Prof. Dieter Naumann, Dr. Peter Lasch and Mr. Wilm Schumacher.

Last but not least, I must thank my mother, Anna Lau, and my good friends who have given me all the emotional support I needed throughout my PhD.